

1-15-2023

Numerical Study of Owls' Leading-Edge Serrations

Asif Shahriar Nafi
Coastal Carolina University

Follow this and additional works at: <https://digitalcommons.coastal.edu/etd>



Part of the [Aerodynamics and Fluid Mechanics Commons](#), [Engineering Physics Commons](#), and the [Fluid Dynamics Commons](#)

Recommended Citation

Nafi, Asif Shahriar, "Numerical Study of Owls' Leading-Edge Serrations" (2023). *Electronic Theses and Dissertations*. 183.

<https://digitalcommons.coastal.edu/etd/183>

This Dissertation is brought to you for free and open access by the College of Graduate and Continuing Studies at CCU Digital Commons. It has been accepted for inclusion in Electronic Theses and Dissertations by an authorized administrator of CCU Digital Commons. For more information, please contact commons@coastal.edu.

Numerical Study of Owls' Leading-Edge Serrations

by

Asif Shahriar Nafi

A Dissertation submitted
in Partial Fulfillment of the Requirements for the
Degree of Doctor of Philosophy in
Marine Science: Coastal and Marine Systems Science

Gupta College of Science
Coastal Carolina University
2023

Dr. Roi Gurka

Graduate Faculty Advisor, Coastal Carolina Univ.

Dr. Angelos Hannides

Comm. Member, Coastal Carolina Univ.

Dr. George Hitt

Comm. Member, Coastal Carolina Univ.

Dr. Elias Balaras

Comm. Member, George WA Univ.

Dr. Nikolaos Beratlis

Comm. Member, Arizona State Univ.

Dr. Erin Hackett

MSCI Assoc. Chair of Graduate Programs

Dr. Chad Leverette

Dean, Gupta College of Science

© Copyright by
Asif Shahriar Nafi
2023

Acknowledgements

I would like to express my deepest gratitude to my advisor, Dr. Roi Gurka, for his unwavering support, guidance, and invaluable mentorship throughout the entirety of my Ph.D. journey. His expertise, encouragement, and constructive feedback have been instrumental in shaping the direction of my research.

I extend my appreciation to the members of my dissertation committee, Dr. Angelos Hannides, Dr. George Hitt, Dr. Elias Balaras and Dr. Nikolaos Beratlis, for their insightful comments and contributions that have significantly enriched the quality of my work. My heartfelt thanks to Dr. Nikolaos, for helping me with the simulations and for providing guidance throughout my Ph.D. journey.

I would also like to thank Dr. Erin Hackett for teaching me several courses that were essential for my thesis research. My thanks to all Environmental Fluids Laboratory (EFL) members as their encouragements have always motivated me.

I am grateful to Coastal Carolina University for providing the resources and research facilities essential for the successful completion of this thesis.

My heartfelt thanks go to my family for their unwavering support and understanding during this demanding academic pursuit. Their love and encouragement have been my anchor throughout this challenging journey.

Finally, I extend my gratitude to all those who, directly or indirectly, have played a role in the realization of this research endeavor. Your support has been indispensable, and I am deeply appreciative.

Abstract

The silent flight ability of owls is often attributed to their unique wing morphology and its interaction with their wingbeat kinematics. Among these distinctive morphological features, leading-edge serrations stand out – these are rigid, miniature, hook-like patterns located at the leading edge of the primary feathers of their wings. It had been hypothesized that these leading-edge serrations serve as a passive flow control mechanism, influencing the aerodynamic performance and potentially affecting the boundary layer development over the wing, subsequently influencing wake flow dynamics. Despite being the subject of research spanning multiple decades, a consensus regarding the aerodynamic mechanisms underpinning owls' leading-edge serrations remains elusive. While the literature extensively explores the aerodynamic and aeroacoustic properties of serrated wing geometries, the predominant focus had been on "owl-like" serrations, including sawtooth patterns, wavy configurations, cylindrical shapes, and slitted variations. This emphasis has often overshadowed the authentic geometry of owl wing serrations, which are notably shorter than the wing's chord and oriented at an angle relative to the freestream airflow. In order to shed light on the flow dynamics associated with owls' leading-edge serrations, this study delves into numerically simulating the flow field surrounding an owl wing, meticulously replicating the serrated leading-edge geometry, at an intermediate chord-based Reynolds number (40000). A direct numerical simulation (DNS) approach is employed to simulate the fluid flow problem, where the Navier-Stokes equations for incompressible flow are solved on a Cartesian

grid with sufficient resolution to resolve all the relevant flow scales, while the wing is represented using an immersed boundary method. Two wing planforms are considered for numerical analysis: one featuring leading-edge serrations and another without them. The findings suggest that the serrations improve suction surface flow by promoting sustained flow reattachment via streamwise vorticity generation at the shear layer, prompting weaker reverse flow, and thus augmenting stall resistance. However, aerodynamic performance is negatively impacted due to the shear layer passing through the serration array which results in altered surface pressure distribution over the upper surface. It is also found that serration increases turbulence level in the downstream flow. Turbulent momentum transfer near the trailing edge is significantly increased due to the presence of serrations upstream the flow which also influences the mechanisms associated with separation vortex formation and its subsequent development over the upper surface of the wing. Turbulent budget analysis at the leading-edge shear layer demonstrates that serration reduces turbulence production in the immediate vicinity; however, the reduction effect does not persist further downstream when the shear layer rolls up, and eventually merges with a large separation vortex. In the wake of the serrated wing, integral scale was found to be larger than the smooth wing which implies that serrations at the leading-edge does not promote scale reduction at the wake.

Table of contents

| | |
|--|------|
| List of figures | viii |
| Nomenclature | xvii |
| 1. Introduction | 1 |
| 1.1 Research objectives | 3 |
| 1.2 Thesis outline | 4 |
| 2. Literature survey..... | 6 |
| 2.1 Low to moderate Reynolds number aerodynamics | 6 |
| 2.2 Special morphological features of owls' wing | 12 |
| 2.3 Flow over owl wing: state of the art | 17 |
| 3. Methodologies | 23 |
| 3.1 Numerical solver..... | 23 |
| 3.1.1 Temporal and spatial discretization..... | 24 |
| 3.1.2 Poisson solver..... | 31 |
| 3.2 Boundary conditions..... | 33 |
| 3.2.1 Dirichlet and Neumann boundary condition..... | 34 |
| 3.2.2 Convective boundary condition..... | 36 |
| 3.2.3 Periodic boundary condition..... | 36 |
| 3.3 Embedded boundary method..... | 37 |
| 3.4 Validation of the numerical solver..... | 43 |
| 3.4.1 Validation case: flow over a 2D cylinder | 43 |
| 3.4.2 Validation case: two-dimensional (2D) flow over an Eppler airfoil..... | 46 |

| | |
|--|-----|
| 4. Computational setup..... | 49 |
| 4.1 Owl wing model..... | 50 |
| 4.2 Computational domain and grid resolution..... | 53 |
| 5. Flow physics..... | 58 |
| 5.1 Time-averaged characteristics..... | 58 |
| 5.2 Instantaneous flow dynamics..... | 66 |
| 5.3 Influence of serrations on turbulence: statistical analysis..... | 82 |
| 5.4 Influence of serrations on instantaneous turbulence..... | 91 |
| 5.5 Turbulent kinetic energy (TKE) budget..... | 98 |
| 5.6 Estimation of integral scales at the wake..... | 108 |
| 6. Experimental study using 3D printed owl wing | 111 |
| 6.1 Boundary layer characteristics | 114 |
| 7. Summary and conclusion..... | 119 |
| Bibliography | 125 |

List of figures

| | |
|--|----|
| Figure 2.1.1: A depiction of turbulence energy spectrum. The horizontal axis denotes to wavenumber (k) and the vertical axis denotes to energy spectrum of turbulence ($E(k)$) | 8 |
| Figure 2.2.1: A dorsal view of a (A) Barn owl wing and a (B) Pigeon wing (Bachmann, 2010) | 13 |
| Figure 2.2.2: Anatomy of a Barn owl's feather (Bachmann and Winzen, 2014) | 14 |
| Figure 2.2.3: Comb-like structures at the leading edge of Barn owl's 10th primary feather in different magnifications (Bachmann, 2010) | 14 |
| Figure 2.2.4: Trailing-edge fringes of a 5th primary feather of a Barn owl wing in different magnification (A, B, C) (Bachmann, 2010); schematic diagram of trailing-edge fringes (D) (Bachmann <i>et al.</i> , 2012) | 16 |
| Figure 2.2.5: Velvety upper surface of a 10th primary feather of a barn owl (Bachmann and Winzen, 2014) | 16 |
| Figure 3.1.1: Velocity and pressure variable arrangement in a cartesian grid | 27 |
| Figure 3.1.2: Staggered grid in x-z plane..... | 28 |
| Figure 3.2.1: Implementation of Dirichlet and Neumann boundary conditions..... | 34 |
| Figure 3.2.2: Implementation of periodic boundary condition..... | 37 |

| | |
|--|----|
| Figure 3.3.1: The parametrized description of interfaces of arbitrary shapes using marker particles (Yang, 2005) | 38 |
| Figure 3.3.2: Relation between interface and Cartesian grid (a) a parametrized elliptical body immersed in fluid (b) a zoom-in view of the body where tagging process is shown. Here, ■ solid points; □ fluid points (Yang, 2005) | 40 |
| Figure 3.3.3: Illustration of ■ body points, Δ forcing points and □ fluid points (Yang, 2005)..... | 40 |
| Figure 3.3.4: Interpolation procedure at the forcing point (Yang, 2005) | 43 |
| Figure 3.4.1: Computational domain around the cylinder of diameter, D..... | 44 |
| Figure 3.4.2: A section of the computational grid around the cylinder in the x-z plane. Here, x denotes to cross-stream direction and z denotes to streamwise direction..... | 45 |
| Figure 3.4.3: Spanwise vorticity (ω_y) contour in the vicinity of the cylinder at (A) Re=20 and (B) Re=40. Here, x denotes to cross-stream direction and z denotes to streamwise direction..... | 46 |
| Figure 3.4.4: Computational domain around the airfoil; here, c denotes to chord length, x is cross-stream direction and z denotes to streamwise direction..... | 47 |
| Figure 3.4.5: Comparison of lift coefficient (C_L) and drag coefficient (C_D) over non-dimensional flow time (tU_∞/c)..... | 47 |

Figure 3.4.6: Comparison of spanwise vorticity contours (ω_y) between the current study and Rahromostaqim *et al.* (2016). The data are displayed on x-z plane; (A) and (C) are time-spanwise averaged ω_y ; (B) and (D) are instantaneous ω_y48

Figure 4.1.1: Profile of the owl airfoil extracted from Liu *et al.* (2006)50

Figure 4.1.2: Leading-edge serrations assembled with the 3D owl wing.....51

Figure 4.1.3: Schematic of a first-order approximation of a serration in different views (A–D). (E) Tilt angle and distance. (F) Inclination angle towards the leading edge of a wing (Bachmann and Wagner, 2011)52

Figure 4.2.1: Computational domain around a section of the owl wing. Here, c denotes to average chord length; z-axis denotes to streamwise direction, x-axis is the cross-stream direction while the spanwise direction is represented by y-axis.....54

Figure 4.2.2: Non-uniform grid step size in the (A) streamwise (z) direction, and (B) cross-stream (x) direction. Here, dz and dx denote to grid step size in the streamwise and cross-stream direction, respectively. Leading-edge of the wing is at [0,0] while trailing edge ends at [0.95, -0.34] in the zx plane.....55

Figure 4.2.3: Cartesian grid around the serrated owl wing in the xz plane.....56

Figure 5.1.1: Contour plots of time-averaged skin friction coefficient, $\overline{C_f}$: (a) serration (b) smooth; time-averaged pressure coefficient, $\overline{C_p}$: (c) serration (d) smooth.....61

Figure 5.1.2: Comparison of (b) time-averaged skin friction coefficient, $\overline{C_f}$ and (c) time-averaged pressure coefficient, $\overline{C_p}$. For both cases, the coefficients were taken from a slice (black line) shown in (a). The horizontal axis represents normalized streamwise locations (z/c).....61

Figure 5.1.3: Time and spanwise averaged streamwise velocity, $\langle \bar{w}/U_\infty \rangle$ for (a) serration, (b) smooth case; streamlines from time and spanwise averaged velocity field for (c) serration, (d) smooth case shown over velocity magnitude contour plot.....63

Figure 5.1.4: Wall normal distance (d/c) vs time and spanwise averaged streamwise velocity profiles ($\langle \bar{w} \rangle / U_\infty$) over serrated and smooth wing's upper surface (S4-S16). Locations of the profiles over the upper surface are shown in (A)64

Figure 5.1.5: Time and spanwise averaged spanwise velocity, $\langle \bar{v}/U_\infty \rangle$ for (a) serrated, (b) smooth case65

Figure 5.1.6: Frequency spectrum of the lift coefficients (C_L). PSD abbreviates to power spectral density66

Figure 5.2.1: Evolution of spanwise vorticity, $\omega_y c / U_\infty$ during one shedding period, T_s ; figure a-f illustrates $\omega_y c / U_\infty$ of the serrated wing (left) while a'-f' denotes to ω_y of the smooth case (right). Figure A-F/A'-F' shows instantaneous streamlines colored with velocity magnitudes during each shedding phase shown in the spanwise vorticity contours. Time interval between two consecutive sub-figures is $T_s/5$ 70

Figure 5.2.2: Vorticity magnitude, $|\omega|$ during $t=0, 2T_s/5$ and $3T_s/5$ instances shown in figure 5.1.7 (left: serrated wing; right: smooth wing). Black lines illustrate the locations where vorticity magnitude data were extracted from. The lines were placed in such a manner so that they pass through the vortex cores and its boundaries. Figure a”-c” are the line plots of the extracted vorticity magnitude data74

Figure 5.2.3: Instantaneous iso-surface of Q-criterion ($Q=1000$) colored with streamwise vorticity ($\omega_z c/U_\infty$), during the instances shown in figure 5.1.7.....78

Figure 5.2.4: Frequency spectra of the velocity fluctuations at the leading edge inside the separated shear layer; left: serrated wing, right: smooth wing. Probe locations are shown in row (a), frequency spectra of streamwise velocity fluctuations in row (b) and spanwise velocity fluctuations in row (c). PSD abbreviates to power spectral density80

Figure 5.2.5: Time and spanwise averaged streamwise gradient of spanwise velocity profiles (dv/dz); taken at three locations shown in (a) where location (1) is the leftmost and location (3) is the rightmost81

Figure 5.2.6: 3D streamlines showing flow deflection effect by serrations. Streamlines colored with time averaged spanwise velocity.....82

Figure 5.3.1: (a) Time and spanwise averaged turbulent kinetic energy (TKE) of serrated case, (a’) smooth case; RMS of streamwise velocity fluctuations for (b) serrated wing, (b’) smooth wing; RMS of vertical velocity fluctuations for (c) serrated wing (c’) smooth wing; RMS of spanwise velocity fluctuations for (d) serrated wing

(d') smooth wing. Note that, TKE and RMS values are normalized by U_∞^2 and U_∞ , respectively.....85

Figure 5.3.2: Comparisons of TKE profiles. Data taken at the locations shown with black lines over the contour plot; (a) profiles over the wing (b) at the wake. Location numbering (i.e., a1, a2..., a5) starts from the leftmost line in the contour maps in (a) and (b).....86

Figure 5.3.3: From left: RMS of streamwise velocity fluctuations, RMS of cross-stream velocity fluctuations, RMS of spanwise velocity fluctuations at location (a1, a2, a3, a4, a5) as shown in figure 15(a)87

Figure 5.3.4: Spanwise averaged Reynolds stress $\langle \overline{u'w'} \rangle / U_\infty^2$ of (a) serrated wing (a') smooth wing; $\langle \overline{u'v'} \rangle / U_\infty^2$ of (b) serrated wing (b') smooth wing90

Figure 5.3.5: Reynolds stress ($\langle \overline{u'w'} \rangle / U_\infty^2$) profile comparison. Data taken at the locations shown with black lines over the contour plot. Location numbering (i.e., a1, a2..., a5) starts from the leftmost line in the contour map (a)91

Figure 5.4.1: Evolution of local helicity density fluctuations ($\overline{u'} \cdot \overline{\omega'} / cU_\infty^2$) during one shedding period, T_s . The subfigures on the left (a-f) depict the helicity density field of the serrated wing while the ones on the right exhibit smooth wing's helicity density field. Note that, the figures correspond to the instantaneous snapshots shown in figure 5.2.194

Figure 5.4.2: Histograms of velocity fluctuations inside the shear layer near the leading-edge (point 1 in sub-figure (a)) of both the wing. Note that, point 1 in sub-figure (a) shows the probe location in the x-z plane while sub-figure (a') shows the x-z plane location (blue circle) on the wing in 3D (i.e., plane intersecting the middle of a serration). Sub-figure (b) depicts the histogram of the serrated wing while (b') shows the histogram of the smooth wing. Here, N represents the number of occurrences during ~20 shedding cycles96

Figure 5.4.3: Histograms of velocity fluctuations inside the shear layer near the leading-edge (point 1 in sub-figure (a)) of both the wing. Note that, point 1 in sub-figure (a) shows the probe location in the x-z plane while sub-figure (a') shows the x-z plane location (blue circle) on the wing in 3D (i.e., between two neighboring serrations). Sub-figure (b) depicts the histogram of the serrated wing while (b') shows the histogram of the smooth wing. Here, N represents the number of occurrences during ~20 shedding cycles97

Figure 5.5.1: Local production and dissipation of turbulence inside the shear layer (c) for both the serrated and the smooth wing. The terms were calculated from the data points shown in (b) located in two planes (plane 1 and plane 2) shown in (a). Plane 1 intersects a serration geometry at the leading-edge while plane 2 is located between two serrations. Same setup has also been maintained for the smooth leading-edge case101

Figure 5.5.2: Comparison of constituent terms of turbulence production and dissipation inside the shear layer (b) for both the serrated and the smooth wing. The

terms were calculated from the data points shown in (b) located in two planes (plane 1 and plane 2) shown in (a). Plane 1 intersects a serration geometry at the leading-edge while plane 2 is located between two serrations. The subfigures (c)-(k) depict the following constituent terms in plane 1 and 2: (c) P11, D11 (d) P12, D12 (e) P13, D13 (f) P21, D21 (g) P22, D22 (h) P23, D23 (i) P31, D31 (j) P32, D32 (k) P33, D33104

Figure 5.5.3: Comparison of streamwise gradients of the mean flow inside the shear layer of both the serrated and the smooth wing. The terms were calculated from the data points shown in figure 5.5.2b in plane 1 (figure 5.5.2a)105

Figure 5.5.4: Local production and dissipation of turbulence at the wake of both the serrated and the smooth wing. The terms were calculated at the profiles shown in (b). Two spanwise planes (plane 1 and 2 as shown in (a)) were considered for the comparison of the profiles for both the serrated and the smooth wing107

Figure 5.6.1: Longitudinal and transverse length scales (L_w, L_u) estimated at the wake profile (e) in plane 1 as shown in figure 5.5.4(a) and figure 5.5.4(b).....110

Figure 6.1: A: Barred owl wing (left) with the specific features commonly found in nocturnal owls' species: leading-edge serrations, velvety upper surface (elongated pennula), and trailing-edge fringes. B: 3D printed wing with a closeup of the serrations (Saussaman *et al.*, 2023)113

Figure 6.2: Schematic description of the field of view locations where measurements were performed. Left: wing cross section divided into three arbitrary regions:

leading-edge (R1), separation (R2), and reattachment (R3), where c is the chord. Right: wing planform; blue lines represent the five different measured PIV planes where b is the wing spanwise length (Saussaman *et al.*, 2023).....113

Figure 6.1.1: The mean streamwise velocity profile deficit ratio within the boundary layer between the serrated and smooth case in the streamwise-normal planes at different spanwise locations (P1, P2, P3, P4, P5). In the sub-panel, c denotes to chord length of the wing (Saussaman *et al.*, 2023)115

Figure 6.1.2: The ratio of the maximal Reynolds stress component $(\overline{w'u'})$ between the serrated and smooth case in the streamwise-normal planes at different spanwise locations (P1, P2, P3, P4, P5). Here, w' refers to streamwise velocity fluctuation, and u' refers to vertical velocity fluctuation (Saussaman *et al.*, 2023)117

Figure 6.1.3: The ratio of the maximal turbulent kinetic energy $(\overline{w' + u'})$ between the serrated and smooth case in the streamwise-normal planes at different spanwise locations (P1, P2, P3, P4, P5). Here, w' refers to streamwise velocity fluctuation, and u' refers to vertical velocity fluctuation (Saussaman *et al.*, 2023)118

Nomenclature

Abbreviations

| | |
|-----|-----------------------------|
| AOA | Angle of Attack |
| CFL | Courant-Friedrichs-Levy |
| DNS | Direct Numerical Simulation |
| FFT | Fast Fourier Transform |
| LEV | Leading Edge Vortex |
| LHS | Left Hand Side |
| PIV | Particle Image Velocimetry |
| PSD | Power Spectral Density |
| RHS | Right Hand Side |
| SV | Separation Vortex |
| TE | Trailing Edge |
| TEV | Trailing Edge Vortex |
| TKE | Turbulent Kinetic Energy |
| UAV | Unmanned Aerial Vehicle |

Roman symbols

| | |
|-----------------|--|
| A | Coefficient matrix |
| a_i, b_i, c_i | Coefficients in quadratic polynomial |
| C_d | Drag coefficient |
| C_f | Skin friction coefficient |
| C_l | Lift coefficient |
| C_p | Pressure coefficient |
| c | Wing chord length |
| D | Diameter of sphere |
| f_s | Shedding frequency |
| L | Integral length scale |
| N_x, N_y, N_z | Number of grid points in x, y, z direction |
| Re | Reynolds number |
| St | Strouhal number |
| S_{ij} | Strain rate tensor |
| t | Time |
| U_∞ | Freestream velocity |
| U_{conv} | Convection velocity |

| | |
|-----------------|--|
| u, v, w | Cross-stream, spanwise and streamwise velocity component |
| u', v', w' | Fluctuating cross-stream, spanwise and streamwise velocity component |
| u_t, v_t, w_t | Tangential velocity components at the boundary of the computational domain |
| x, y, z | Cross-stream, spanwise and streamwise coordinates |

Greek symbols

| | |
|---------------|--|
| δ_{ij} | Kronecker's delta |
| τ_w | Wall shear stress |
| ω'^2 | Enstrophy |
| Δt | Time step |
| \mathcal{H} | Helicity density |
| λ | Wavelength |
| ω | Vorticity |
| η | Kolmogorov length scale |
| ϑ | Kinematic viscosity |
| ε | Dissipation rate of turbulent kinetic energy |

ρ Density

Other symbols

$\langle \rangle$ Span-averaging operator

$\overline{\langle \rangle}$ Time and span-averaging operator

Chapter 1

Introduction

Owls are widely known for their silent flight. Most of them are nocturnal raptors and can fly silently while the diurnal owl species generate sound during their flights akin to any other bird species. The silent owl species have three distinctive wing microfeatures that set them apart from the other non-silent birds including the diurnal owl species. These unique wing features are referred to as: leading-edge (LE) combs/serrations which are rigid miniature hook-like patterns located at the leading edge of their wings at an angle to the freestream; trailing edge (TE) fringes which are soft, flexible hair-like extensions of their feathers located at the trailing edge of their wings; and velvety upper surface that is comprised of elongated soft filaments (known as pennulae) projected from the upper surface of their wings (Graham, 1934; Kroger *et al.*, 1972). Most of the owls have bigger wings compared to their body mass which allows them to fly without spending much efforts (i.e. low wingbeat frequency) (Wagner *et al.*, 2017). They are slow fliers and great at maneuvering among the trees during their hunts. Despite being large, some of the owl species can even hover for a short duration of time (e.g. barn owl, short eared owl, great gray owl, etc.). These aerodynamic performances make them a potential candidate for bioinspired design

research, in particular, for the design improvement of Unmanned Air Vehicle (UAV) wings as they operate at the similar Reynolds number range.

UAVs can be of three types: rotary wing type, fixed wing type and hybrid. Each of the types has its own advantages and limitations. As an example, hybrid and rotary types do not require a runway for takeoff and landing in contrast to the fixed wing types, however, their range is significantly lower compared to the latter ones. On the other hand, despite having a longer range compared to the rotary type UAVs, fixed wing UAVs lack agile maneuverability, are more vulnerable to stalls and incapable of sustaining flight at low speed (Townsend *et al.*, 2020). Due to operating at low to moderate Reynolds number flow regime, they are highly susceptible to flow separation, LSB (laminar separation bubble) formation, etc. which affects their flight performance and stability. To improve their flight characteristics, owl-inspired leading-edge serrations are of great research interest due to their potential as a passive flow control device. It had been hypothesized that owls' leading-edge serrations alter the adjacent flow field partially to suppress aerodynamic noise, impact its aerodynamic performance and function as a passive flow control mechanism (Graham, 1934; Kroger *et al.*, 1972; Lilley, 1998; Wagner *et al.*, 2017; Jaworski and Peake, 2020). Aerodynamic and aeroacoustic characteristics of serrated wing geometries have been studied extensively in literatures, however, the focus was mainly on "owl-like" serrations (i.e. sawtooth types, wavy, slitted, etc.) rather than the actual geometry of the owl's wings' serrations which are significantly shorter than the wing chord and at an angle with the freestream. Also, the impact of the microscale LE serrations on the turbulent characteristics of the flow field is not clearly understood

yet. This gap in the literatures resulted from the fact that the microscale serrations are significantly smaller than the wing itself and numerically simulating their effects are exceptionally difficult due their microscale size and large numbers at the leading edge. Besides, wind tunnel experiments of preserved owl wing or live birds cannot shed light on the flow physics associated with a particular aspect (i.e. LE serrations, TE fringes, etc.) rather the flow field data encompasses the effects from all micro and macro features of the wing.

1.1 Research objectives

The objective of this thesis research is to illuminate the intricacies of flow dynamics attributed to the incorporation of "owl's leading-edge serrations" into an owl-airfoil-based wing. This study aims to characterize the turbulent flow field around an owl wing with LE serrations and to elucidate its flow control mechanisms. To capture the full spectrum of small-scale motions, a Direct Numerical Simulation (DNS) approach is employed to resolve the flow field dynamics across the range of scales. Most numerical research today on owl wings simplifies the airfoil by utilizing symmetric profiles, such as the NACA0012, while many studies turn to simplified, bio-inspired serrations, including sinusoidal, sawtooth, and similar patterns, to circumvent the complexities associated with meshing and solution convergence due to the intricate nature of actual serrations (Jaworski and Peake, 2020; Wang *et al.*, 2019). This study utilizes the same size and shape as those found on actual owl wings, which were designed using data from the research conducted by Bachmann and Wagner (2011).

1.2 Thesis outline

The outline of this thesis is as follows:

Chapter 2 is focused on describing the important concepts of low to moderate Reynolds number aerodynamics, owls' unique morphological features, recent studies that investigate owls' wing features as well as its flow physics, etc. to establish the groundwork required for comprehensive understanding of the subsequent analysis and results.

Chapter 3 provides a detailed account of the computational methodologies utilized in this study to model the flow field around the owl wing. The chapter covers solution procedures for governing fluid flow equations, the use of immersed boundary formulations to handle fluid-solid interface boundary conditions, and validation cases aimed at confirming the accuracy of the employed code.

In Chapter 4, the simulation setup for the fluid flow around the model owl wing is meticulously described. Geometric characteristics of the owl wing model, as well as the configuration of leading-edge serrations, are briefly discussed. This chapter also addresses grid resolution and outlines certain limitations inherent in the current setup.

Chapter 5 centers on the interpretation of the results obtained from the numerical simulations. The influence of serrations on the flow field around the owl wing is elucidated by comparing results with the same wing lacking serrations. The section focuses on time-averaged flow patterns, instantaneous flow field properties

illustrating the spatial-temporal development of the flow field, and both instantaneous and time-averaged turbulence characteristics to elucidate alterations in flow dynamics due to serrations.

Finally, conclusions are presented in Chapter 6.

Chapter 2

Literature survey

2.1 Low to moderate Reynolds number aerodynamics

An important non-dimensional number to describe the nature of the fluid flow is Reynolds number ($Re = \frac{\rho U_{\infty} L}{\mu}$; where, ρ, U_{∞}, L, μ denotes to fluid density, freestream velocity, characteristic length and viscosity, respectively.) which is a ratio of inertial force to viscous force in the flow. Low Re indicates viscous force is significant in the flow while high Re implies viscous force can be neglected as inertial force dominates the flow. To estimate the Re of small flying insects, birds, UAVs, etc., their wing chord (c) is used as the characteristic length. In such cases, the chord-based Reynolds number (Re_c) ranges from $10^4 - 1.5 \times 10^5$ which falls under low to moderate Reynolds number regime (Tank *et al.*, 2016; Shy *et al.*, 2008). Complex viscous flow phenomena such as LSB (laminar separation bubble) formation, laminar to turbulent transition, flow reattachment, etc. are prevalent in this flow regime. On the other hand, fluid flows with high Reynolds number are invariably turbulent. Turbulent flows are characterized by chaotic changes of flow properties. They exhibit three-dimensional vorticity fluctuations, high diffusivity (causes rapid mixing and transport of mass, energy, and momentum), high dissipation (decays rapidly in the absence of

kinetic energy from the mean flow) which commonly are associated with high Reynolds number flows (Tennekes and Lumley, 1972).

Turbulence is a flow phenomenon emanated from instability driven by flow shear, buoyancy, Coriolis force, etc. which contains eddying motions that vary greatly over time and space. Pope (2000) defines an eddy as “An ‘eddy’ eludes precise definition, but it is conceived to be a turbulent motion, localized within a region of its characteristic size, that is at least moderately coherent over this region. The region occupied by a large eddy can also contain smaller eddies.” The largest size of the eddies corresponds to the characteristic width of the flow, and they are affected by the geometry of the boundaries (Tsinobar, 2001). The size of the smallest eddy is determined by the viscous dissipation of energy supplied by the mean flow; this is known as Kolmogorov microscale ($\eta_k \equiv \left(\frac{\nu^3}{\varepsilon}\right)^{\frac{1}{4}}$, where, ν is the kinematic viscosity and ε is the dissipation rate of turbulent kinetic energy) and is the smallest scale in turbulent flows. The dissipation rate is independent of viscosity but the scales at which dissipation occurs depends on both viscosity and dissipation rate. The sequential process through which energy is transferred from the largest eddies to gradually smaller eddies and consequently to the smallest eddies at which energy is dissipated by viscosity is known as turbulent energy cascade (Richardson, 1922). This energy transfer process is valid in large Reynolds number regime, away from the boundary while the turbulent flow is fully developed. Large scale eddies (integral scale) are fueled by the shear in the mean flow and they contain most of the turbulent kinetic energy and are low in wavenumber whereas the smallest eddies (Kolmogorov

scale) are high in wavenumber but contains little energy and eventually dissipates into heat (Figure 2.1.1). Taylor microscale is the intermediate scale which corresponds to Kolmogorov's inertial sub-range. Eddies of this size are weakly influenced by the viscosity of the fluid (McDonough, 2007). In the inertial subrange, eddies do not receive energy from the mean flow or are not subjected to viscous dissipation (Tennekes and Lumley, 1972). The energy transfer from large to small scales is driven by self-amplification of the rate of strain production as well as vortex compression as opposed to the vortex stretching mechanism which contributes to suppressing the cascade instead (Tsinobar, 2001). The length scales in the flow are important in owl's flight as these scales should be different as compared to a bird flight which does not have the micro wing features like owl.

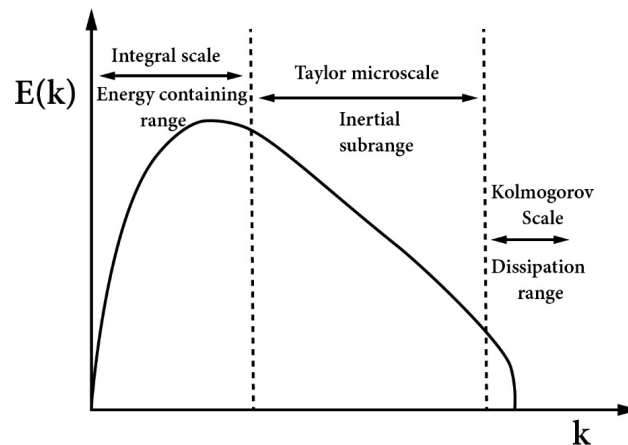


Figure 2.1.1: A depiction of turbulence energy spectrum. The horizontal axis denotes the wavenumber (k) and the vertical axis denotes the energy spectrum of turbulence ($E(k)$).

When a body/surface is in contact with a moving stream, boundary layer forms due to the fluid viscosity. With low to moderate Reynolds number flows, the boundary layer over the wing is initially laminar which may separate from the surface due to adverse pressure gradient (APG); as a result, detached shear layer forms which is highly unstable and very susceptible to transition. Depending on the flow conditions, the flow may reattach to the surface and separation bubble is formed. The characteristics of an 'ideal' laminar separation bubble (LSB) is briefly discussed in the study by O'Meara and Mueller (1987). Typically, an LSB will have a "dead air region" immediately after the separation point followed by a "recirculation zone" where the reverse flow occurs. However, an LSB can also be unsteady in nature when the angle of attack (AOA) of the airfoil is relatively very high. Rinoie and Takemura (2004) investigated the nature of such LSBs formed on NACA0012 airfoil at 11.5° AOA with 1.3×10^5 Reynolds number. They found that the mean velocity profiles over the upper surface was signifying the aspects of a long LSB (~35% of the chord), however, the instantaneous upper surface flow was switching back and forth between a short LSB (~10% of the chord) and a long LSB. This phenomenon is termed as "bubble bursting" (Pauley *et al.*, 1990; Zaman *et al.*, 1989, Sandham, 2008). Vortex shedding might also occur when there's bubble bursting present in the flow depending on the Reynolds number and the strength of the APG (Pauley *et al.*, 1990). Vortex shedding is a ubiquitous phenomenon as it was found to occur over a wide range of cases with low to high Reynolds number as well as for different shapes of bodies in the fluid (Bearman, 1984). The term "vortex" or "vortices" does not have a universally accepted definition (Jeong and Hussain, 1995). A simple definition of vortex was

suggested by Saffmen and Baker (1979) which is “rotational fluid having a finite volume, bounded by solid wall or irrotational fluid”. When fluid flows over a solid body and “vortices” are generated and eventually shed in the flow downstream the body, this phenomenon is referred to as vortex shedding. Vortex shedding is also very common in flapping flight due to the unsteady motion of the wing. For lifting surfaces, vortex shedding is also observed when it operates beyond a critical AOA (at which the airfoil generates maximum lift) which is known as “stall”.

Stall phenomenon can be dynamic or static. Static stall refers to the condition when airfoil is operating at a fixed AOA beyond the critical AOA while the dynamic stall is associated with time-dependent increase in AOA beyond the critical AOA. Generally, airfoils/wings operating below the critical AOA generates higher lift with the increase in AOA. When stall occurs, production of lift is significantly lessened. This occurs due to flow separation over the airfoil without subsequent reattachment. Stall is categorized into three types, namely: leading-edge stall, trailing-edge stall and thin airfoil stall (McCullough and Gault, 1951; Anderson, 2017). Leading-edge stall is associated with “abrupt” flow separation at the leading edge which does not reattach over the airfoil surface downstream in the flow. Trailing edge stall is characterized by separated flow at the trailing edge region; however, the flow at LE is attached for such cases. This type of stall is commonly observed in the flows over thick airfoils. Thin airfoil type stalls (i.e. bird airfoils, flat plate, etc.) is also termed as “soft” stall due to the loss of lift not being very severe unlike the other two types of stalls. This type of stall is a result of minimal thickness to chord ratio of the airfoil; such cases exhibit separation bubble at the leading edge even at small AOA. When the airfoil is at critical

AOA, the separation bubble covers most of the upper surface. (Broeren and Bragg, 2001; Anderson, 2017). During thin airfoil stall, the force fluctuations (i.e. lift, drag, etc.) are much more severe compared to the two other types. In addition to these three fundamental stall types, Broeren and Bragg (2001) also reported two “combination type” stalls, namely: trailing edge/leading-edge stall and thin airfoil/trailing edge stall. These types of stall have flow characteristics of the two fundamental stall types combined at the same time. However, irrespective of stall types, all of them are undesired during flights as they significantly diminish aerodynamic performance ($\frac{Lift}{Drag}$).

Aerodynamic performance of airfoils at low to moderate Reynolds number range have been studied extensively by Schmitz (1942), Abbott and Von Doenhoff (1959), Mcmasters and Henderson (1979). These studies demonstrate that there exist a critical Reynolds number range for most airfoils ($Re \sim 10^4 - 10^6$) when aerodynamic performance suffers due to excessive drag force compared to the cases with Reynolds number range above the critical Re . In this flow regime, laminar, transitional, turbulent regions of the flow have a significant effect on the aerodynamic forces, as a result, conventional turbulence models fail to accurately predict the flow. Owl’s flight Reynolds number (30,000-120,000) also falls under this Reynolds number range. However, the presence of special microfeatures over the wing have additional effects on the aforementioned viscous flow phenomena that modulate the flow to alter the overall flow dynamics.

2.2 Special morphological features of owls' wing

Owls can be found almost all over the world except icy Antarctica. The owl taxa contain about 250 different species. Apart from some fish-eating owls (e.g., Malay fish owl, Tawny fish owl, etc.) that are diurnal raptors, most of them are nocturnal and can fly silently. In 1934, Graham reported the differences in wing morphology between nocturnal owls and fish-eating owls and listed three distinct characteristics that set the nocturnal owls apart from the fish-eating owls. These three distinct characteristics are named as leading-edge combs/serrations, trailing edge fringes and velvety upper surface. Apart from silent owls, all other birds (including fish-eating owls) do not possess these three distinct morphological features collectively; as an example, the velvety feathers were found to be present on the wings of some hawks (e.g., Kites, Harrier, etc.) and nightbirds (*nocturnal Caprimulgiformes*), however, other two owl wing features were not present. The plumage of the avian wing can be divided into two categories: remiges (flight feathers such as primaries, secondaries, etc. and alula) and coverts. Typical wing profiles (dorsal view) of a Pigeon and a Barn owl are shown in Figure 2.2.1. Both wings show similarity in terms of major features such as having primaries, secondaries, alula, and coverts. But the wing edges as well as the wing surface are smooth for Pigeon wing whereas owl wings have serration at the edges and the wing surface feathers are loose and velvety. Owl's feathers are very different as compared to other birds which form these differences in the wing.

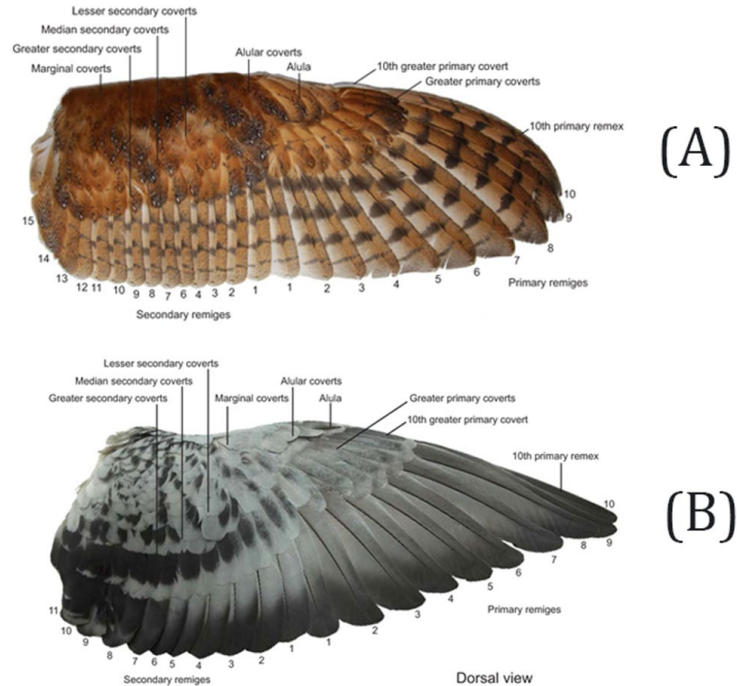


Figure 2.2.1: A dorsal view of a (A) Barn owl wing and a (B) Pigeon wing (Bachmann, 2010)

A typical flight feather of a Barn owl (Figure 2.2.2) comprises a rachis and a vane (the narrow side of the vane is known as outer vane and the wider side is known as inner vane). Each vane is comprised of barbs that stem from the rachis. The basal section of the rachis which is known as calamus, or quill does not have any barbs and embedded into the birds' skin. A barb is comprised of a base (central shaft), hook (distal) and bow (proximal) radiates (Figure 2.2.2). There are tiny hooklets attached to the hook radiates which connect with grooves formed by the bow radiates of neighboring feathers and creates a continuous surface. Every feather has filament like structures at the tip of the hook radiates which are known as pennula (Bachmann and Winzen, 2014).

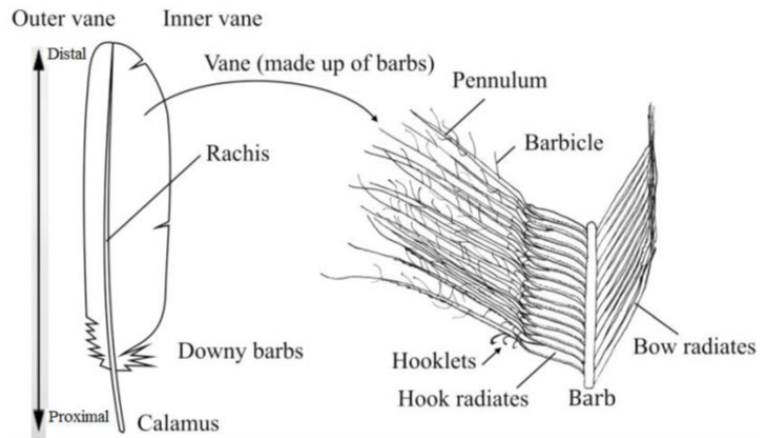


Figure 2.2.2: Anatomy of a Barn owl's feather (Bachmann and Winzen, 2014)

The primary feathers (p) which form the leading-edge of the owl wing (i.e., p7, p8, p9, p10, etc. for a Eurasian eagle-owl (Weger and Wagner, 2016)) incorporate comb-like structures which are the separated barb endings of the outer vanes of the feathers (Bachmann, 2010). Figure 2.2.3 shows the photograph of leading-edge combs/serrations of a Barn owl's 10th primary feathers in different magnification (Bachmann, 2010).

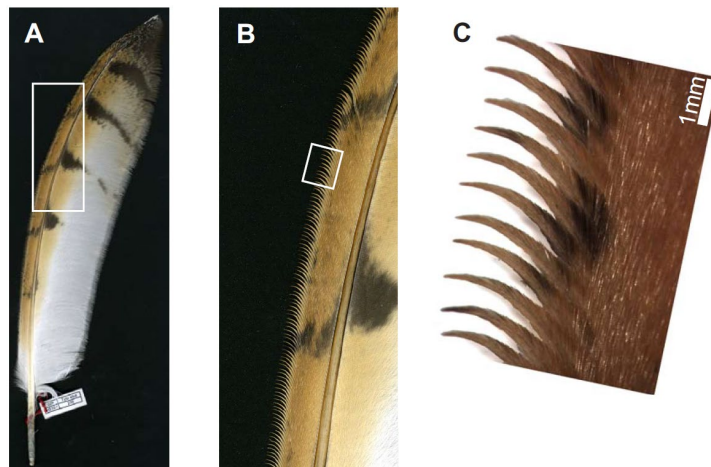


Figure 2.2.3: Comb-like structures at the leading edge of Barn owl's 10th primary feather in different magnifications (Bachmann, 2010)

The presence of trailing-edge fringes in all feathers is another characteristic feature of an owl wing (Figure 2.2.4D). Due to the lack of hooklets near the edges of inner vanes of the feathers, the barb endings separate and form thin feathers fibers known as “fringes”. The length of the fringes is smaller near the tip regions of the feathers as compared to the basal regions (Bachmann *et al.*, 2012). When the wing is fully extended (i.e., during gliding), the trailing edge fringes can merge with the adjacent feathers to form a continuous smooth surface. When the wing is not fully extended, air can pass through the gap between adjacent feathers and trailing edge fringes of all feathers are subjected to air flow (Bachmann and Winzen, 2014).

Owl wings have a velvety upper surface which is formed by pennula present in every feather (Figure 2.2.5). As compared to the other birds, owls have extremely elongated pennula which overlap up to five neighboring barbs (Bachmann and Winzen, 2014). These pennula develop differently on different areas of the wing. The longest pennula are located on areas covered by the neighboring feather vanes whereas the shorter pennula (brush like shape) are located on uncovered areas which are subjected to direct air flow.

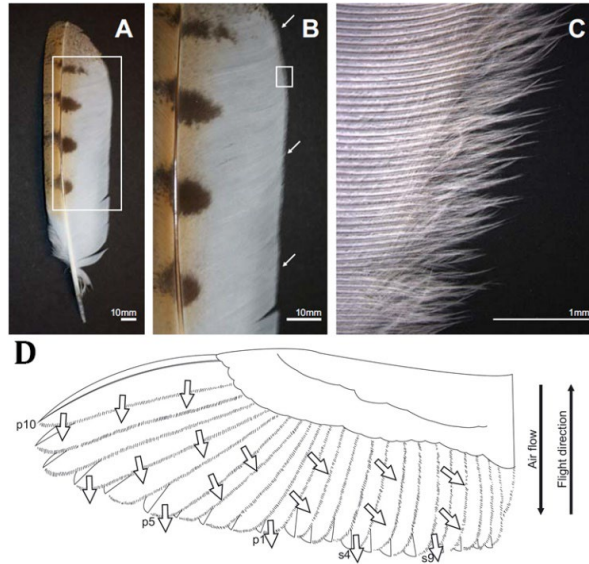


Figure 2.2.4: Trailing-edge fringes of a 5th primary feather of a Barn owl wing in different magnification (A, B, C) (Bachmann, 2010); schematic diagram of trailing-edge fringes (D) (Bachmann et al., 2012)

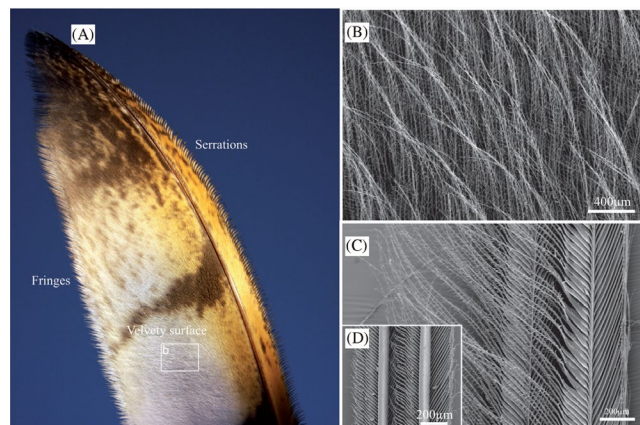


Figure 2.2.5: Velvety upper surface of a 10th primary feather of a barn owl (Bachmann and Winzen, 2014).

The specific functions of these unique adaptations in owl's wings have always been a matter of debate among the researchers. Over the past few decades, there have been

much efforts by the researchers to unveil the flow physics associated with these wing microfeatures. A brief review of the available literatures concerning owls' special wing microfeatures, particularly focusing on the leading-edge combs/serrations is presented in the subsequent section.

2.3 Flow over owl wing: state of the art

Owls' special wing morphology was first reported by Mascha in 1904 where he described the peculiarities of the "comb-shaped" structures located at the leading-edge of the outermost feathers (flight feathers). Later Graham (1934) provided a brief description of the owls' special feathers that demarcates owls from the other species of birds. Graham (1934) suggested that leading edge comb might generate a slot effect at positive angles of attack. As a result, the flow will experience lower angle of attack when it reaches the leading edge behind the comb. He also surmised that the leading-edge comb would reduce the airflow speed, preventing abrupt pressure drop on the suction side of the wing surface. In the case of trailing edge fringe, it influences the process of mixing between the airflow from the upper and the lower side of the wing (Graham, 1934). As for role of the downy upper surface, he suggested that it is associated with stabilizing the boundary layer in rear of the leading edge which might delay flow separation. Despite the lack of any experimental investigation, the observations and the logical reasonings laid out by Graham (1934) encouraged the scientists to seek better understanding of the wing attributes and their impacts on the flow field around owl wings.

Early studies concerning flights of owls were mainly focused on flight noise measurements rather than the flow dynamics aspects (Thrope and Griffin, 1962; Gruschka *et al.*, 1971; Kroeger *et al.*, 1972; Neuhaus *et al.* 1973). Kroeger *et al.* (1972) found that removal of leading-edge combs/serrations from a Florida barred owl's wing did not impact the noise spectrum during its gliding flight. Wind tunnel tests on two prepared owl wings were also included in the scope of the work by Kroeger *et al.* (1972). The removal of leading-edge serrations prompted flow separation near the leading edge. They suggested that the leading-edge serrations served as vortex sheet generators (several angled plates that are usually attached to an aerodynamic surface to generate swirling flow behind them) that kept the flow attached over half of the wing surface from the leading-edge. Kroeger *et al.*'s (1972) experimental results served as a basis for postulating theories regarding the roles of owls' special wing features by the contemporary researchers. Anderson (1973) revisited Kroeger *et al.*'s (1972) experimental data as well as he also investigated leading edge serrations found on a great horn owl wing using microphotography. He took note of the slanting angle of the serrations relative to the wing leading edge and based on the findings, he built several cascade configurations of conventional airfoils (that resemble the owl's leading-edge serrations) to emulate the owl wing and conducted flow visualization experiments on them. The results showed the presence of a spanwise vortex sheet (LEV) on the suction surface similar to of what forms on a delta wing. At low angle of attack, the presence of cascade introduced very negligible drag penalty, but at high angles of attack, they turned the flow towards the spanwise direction, forming a vortex sheet that significantly enhanced aerodynamic performance. Leading edge

serrations enhance aerodynamic performance – this opinion was also shared by Lilley (1998), but he offered a different explanation. According to Lilley (1998), serrations are like a set of equally spaced co-rotating vortex generators (that generate streamwise vortices) which stabilizes laminar boundary layer; as a result, prevents flow separation and keeps the flow attached up to the trailing edge.

One of the most detailed study on owl's morphometric characteristics was conducted by Bachmann *et al.*, (2007) where the authors compared wing feather characteristics of a barn owl (*tyto alba*) and pigeon (*columba livia*). There were differences in size and shape between these two species' feathers where the owl had the bigger feathers. They also found that owl feathers were more porous than the pigeon feathers meaning more air could pass through the owl wing while in flight. Using confocal laser scanning microscopy, Bachmann and Wagner (2011) reconstructed the leading-edge serration shape from a barn owl wing. They provided complete information of length, profile, inclination, orientation of serrations on a barn owl wing. Klan *et al.* (2009, 2010) conducted surface scanning of several dead barn owl wings and reconstructed a three-dimensional barn owl wing model based on the data. Based on the geometrical shape of the serrations, they constructed an array of solid and flexible comb-like structures to investigate their influence on the flow field of a NACA airfoil at low angles of attack ($0^\circ, 3^\circ, 6^\circ$) with Reynolds number being 40,000, 60,000, 120,000 (Klan *et al.*, 2010). Their PIV study results showed that the influence of leading-edge serrations on the flow field was strongly depended on multiple factors (e.g., Reynolds number, angle of attack, flexibility, orientation of the combs in the spanwise direction, etc.). Also, in all the experiments, they observed that the size of

the separation bubble was impacted due to the leading-edge serrations; however, the bubble always occurred at the leading-edge. Winzen *et al.* (2014) conducted time-resolved PIV and force measurement studies using two types of cylindrical shaped serrations, one of the them was made out of metal, and the other was made with silicon. They were assembled on a barn owl wing model. The authors reported increase in drag coefficients with similar lift coefficients (compared to the smooth leading-edge case) for all the observations. They also observed that the length of the separation bubble was independent of the Reynolds number (40,000-120,000) effects when the metal serrations were used.

Geyer *et al.*, (2017) conducted acoustic wind tunnel experiments on prepared barn owl wings and demonstrated that leading edge serrations induced a slight increase in lift and a small decrease in noise during gliding flight. Also, in comparison, the clean wing without serrations had a strong noise source at the wing tip which suggested that the leading-edge serrations might eliminate/reduce wing tip noise. It is interesting that these serrations are only present in primary feathers which form the leading edge of the distal part of the wing. To investigate their functionalities during gliding flights as well as noise reduction characteristics, Rao *et al.* (2017) conducted a combined study of numerical and experimental measurements on an idealized (flat plate) single feather model with straight slitted LE serrations. They showed that LE serrations could control laminar-turbulent transition on the suction side of the model at all angles of attack. They also observed that high frequency noise was suppressed and a slight lift augmentation was achieved due to serrations at the leading edge. However, reduced aerodynamic performance was observed below 15° angle of attack

for the serrated model. A recent particle image velocimetry study by Lawley *et al.* (2019) demonstrates downstream wake flow of a freely flying boobook owl (*ninox boobook*) having flow scales that was an order of magnitudes smaller than non-owl species (European starling, sandpiper). The findings suggest that flow scales modulation occurs in owl's flight, and this might be associated with the special microfeatures of the owl wing.

From the brief literature survey above, it is apparent that aerodynamic and aeroacoustic characteristics of serrated wing geometries have been studied extensively by researchers, however, the focus was mainly on “owl-like” serrations (i.e. sawtooth types, wavy, sinusoidal, slitted, etc.) rather than the actual geometry of the owl's wings' serrations which are significantly shorter than the wing chord and at an angle with the freestream (Jaworski and Peake, 2020). Also, the impact of the microscale LE serrations on the turbulent characteristics of the flow field is not clearly understood yet. This gap in the literature resulted from the fact that the microscale serrations are significantly smaller than the wing itself and numerically simulating their effects are exceptionally challenging due their size and large numbers at the leading edge. Besides, wind tunnel experiments of preserved owl wings or live birds cannot shed light on the flow physics associated with a particular aspect (i.e., LE serrations, TE fringes, velvety surface, etc.) rather the flow field data encompasses the effects from all micro and macro features of the wing. Therefore, the objective of this study is to elucidate the flow physics associated with “owl's leading-edge serrations” incorporated on the leading edge of an owl-airfoil based wing. Characterizing the turbulent flow field around the wing is also in the scope of the

current study. To account for all the small-scale motions underlying the large-scale dynamics of the flow, we employ DNS approach to resolve the flow field. In the next section, numerical methods of the DNS solver will be discussed briefly followed by the description of the relevant boundary conditions.

Chapter 3

Methodologies

3.1 Numerical solver

To resolve the flow field around the owl wing, the governing equations of the flow must be solved numerically (as there is no exact solution for the governing equations). For low to intermediate Reynolds number, the flow can be assumed incompressible ($\rho = \text{constant}$). The governing equations of flow for Newtonian, incompressible fluid can be written in dimensionless form:

$$\frac{\partial u_i}{\partial t} + \frac{\partial u_i u_j}{\partial x_j} = -\frac{\partial p}{\partial x_i} + \frac{1}{Re} \frac{\partial^2 u_i}{\partial x_j \partial x_j} \quad (3.1.1)$$

$$\frac{\partial u_i}{\partial x_i} = 0 \quad (3.1.2)$$

where x_i, x_j ($i, j = 1, 2, 3$) are the cartesian coordinates, u_i, u_j ($i, j = 1, 2, 3$) are the velocity components, t is time, and p is pressure. The lengths are normalized by a reference length L , velocities by a reference velocity U , the time by $\frac{L}{U}$, and the pressure by ρU^2 (where ρ is density of the fluid). To solve the equations 3.1.1 and 3.1.2, time and space discretization of the equations are required so that the velocity and pressure data can be obtained over the domain at every time instance. The discretization of the differential equations will result with a set of algebraic equations

that can be solved in incremental steps. To convert the differential equations (3.1.1 and 3.1.2) into algebraic equations, finite difference method is employed that describes velocity and pressure by means of point samples at the node point of a grid of a coordinate system.

3.1.1 Temporal and spatial discretization

The fluid flow domain is divided into a set of discrete points (grid generation) to discretize the equations. A rectangular prism domain is adopted and divided into $N_x \times N_y \times N_z$ grid cells where N_x, N_y, N_z are the total number of cells in the cross-stream (X-axis), spanwise (Y-axis) and streamwise direction (Z-axis). As the owl wing within the domain does not align with the grid lines, it was introduced using an embedded boundary formulation (section 3.3) so that the no-slip boundary condition representing the owl wing can be reconstructed inside the domain; this strategy enables the cartesian solver handle complex geometries with ease (Balaras, 2004; Yang and Balaras, 2006). The boundary conditions will be discussed briefly in section 3.3.

The governing equations of fluid flow are discretized on a staggered cartesian grid where the velocity components are stored in cell face centers and the pressure is stored in cell center (Figure 3.1.1). In the subsequent sections, half-cell nomenclature for velocity components (such as $i \pm \frac{1}{2}, j \pm \frac{1}{2}, k \pm \frac{1}{2}$) is discarded to be consistent with the numerical implementation in the code. First, by applying standard second-order finite difference scheme, the equations are discretized in a computational space. For convenience, non-uniform grids in the physical space are converted into uniform

grids in the computational space. The mapping between the physical and the computational space is:

$$x = x(\xi), \quad y = y(\eta), \quad z = z(\zeta)$$

and

$$\xi = \xi(x), \quad \eta = \eta(y), \quad \zeta = \zeta(z) \quad (3.1.1.1)$$

where, ξ, η, ζ are the coordinates in the computational space and correspond to coordinates in the physical space (x, y, z) . The transformed derivatives are:

$$\frac{\partial}{\partial x} = \frac{\partial}{\partial \xi} \xi_x, \quad \frac{\partial}{\partial y} = \frac{\partial}{\partial \eta} \eta_y, \quad \frac{\partial}{\partial z} = \frac{\partial}{\partial \zeta} \zeta_z$$

with

$$\xi_x = \frac{2\Delta\xi}{x_{i+1} - x_{i-1}}, \quad \eta_y = \frac{2\Delta\eta}{y_{j+1} - y_{j-1}}, \quad \zeta_z = \frac{2\Delta\zeta}{z_{k+1} - z_{k-1}} \quad (3.1.1.2)$$

where $x_{i+1}, x_{i-1}, y_{j+1}, y_{j-1}, z_{k+1}, z_{k-1}$ are the discrete cartesian coordinates in the physical space. As mentioned earlier, the cell sizes are uniform in the computational space, hence, $\Delta\xi = \Delta\eta = \Delta\zeta = 1$. An example of 2D uniform grid and variable arrangement in $x - z$ coordinates is shown in figure 3.1.2. Transformation of equation 3.1.1 and 3.1.2 in the computational space:

$$\begin{aligned} \frac{\partial u_x}{\partial t} = & - \left[\xi_x \frac{\partial(u_x u_x)}{\partial \xi} + \eta_y \frac{\partial(u_y u_x)}{\partial \eta} + \zeta_z \frac{\partial(u_z u_x)}{\partial \zeta} \right] - \xi_x \frac{\partial p}{\partial \xi} \\ & + \left[\xi_x \frac{\partial}{\partial \xi} \left(v \xi_x \frac{\partial u_x}{\partial \xi} \right) + \eta_y \frac{\partial}{\partial \eta} \left(v \eta_y \frac{\partial u_x}{\partial \eta} \right) + \zeta_z \frac{\partial}{\partial \zeta} \left(v \zeta_z \frac{\partial u_x}{\partial \zeta} \right) \right] \\ & + \left[\xi_x \frac{\partial}{\partial \xi} \left(v_t \xi_x \frac{\partial u_x}{\partial \xi} \right) + \eta_y \frac{\partial}{\partial \eta} \left(v_t \xi_x \frac{\partial u_y}{\partial \xi} \right) + \zeta_z \frac{\partial}{\partial \zeta} \left(v_t \xi_x \frac{\partial u_z}{\partial \xi} \right) \right] \end{aligned}$$

$$\begin{aligned} \frac{\partial u_y}{\partial t} = & - \left[\xi_x \frac{\partial(u_x u_y)}{\partial \xi} + \eta_y \frac{\partial(u_y u_y)}{\partial \eta} + \zeta_z \frac{\partial(u_z u_y)}{\partial \zeta} \right] - \eta_y \frac{\partial p}{\partial \eta} \\ & + \left[\xi_x \frac{\partial}{\partial \xi} \left(v \xi_x \frac{\partial u_y}{\partial \xi} \right) + \eta_y \frac{\partial}{\partial \eta} \left(v \eta_y \frac{\partial u_y}{\partial \eta} \right) + \zeta_z \frac{\partial}{\partial \zeta} \left(v \zeta_z \frac{\partial u_y}{\partial \zeta} \right) \right] \\ & + \left[\xi_x \frac{\partial}{\partial \xi} \left(v_t \eta_y \frac{\partial u_x}{\partial \eta} \right) + \eta_y \frac{\partial}{\partial \eta} \left(v_t \eta_y \frac{\partial u_y}{\partial \eta} \right) + \zeta_z \frac{\partial}{\partial \zeta} \left(v_t \eta_y \frac{\partial u_z}{\partial \eta} \right) \right] \end{aligned}$$

$$\begin{aligned} \frac{\partial u_z}{\partial t} = & - \left[\xi_x \frac{\partial(u_x u_z)}{\partial \xi} + \eta_y \frac{\partial(u_y u_z)}{\partial \eta} + \zeta_z \frac{\partial(u_z u_z)}{\partial \zeta} \right] - \zeta_z \frac{\partial p}{\partial \zeta} \\ & + \left[\xi_x \frac{\partial}{\partial \xi} \left(v \xi_x \frac{\partial u_z}{\partial \xi} \right) + \eta_y \frac{\partial}{\partial \eta} \left(v \eta_y \frac{\partial u_z}{\partial \eta} \right) + \zeta_z \frac{\partial}{\partial \zeta} \left(v \zeta_z \frac{\partial u_z}{\partial \zeta} \right) \right] \\ & + \left[\xi_x \frac{\partial}{\partial \xi} \left(v_t \zeta_z \frac{\partial u_x}{\partial \zeta} \right) + \eta_y \frac{\partial}{\partial \eta} \left(v_t \zeta_z \frac{\partial u_y}{\partial \zeta} \right) + \zeta_z \frac{\partial}{\partial \zeta} \left(v_t \zeta_z \frac{\partial u_z}{\partial \zeta} \right) \right] \end{aligned}$$

$$\xi_x \frac{\partial u_x}{\partial \xi} + \eta_y \frac{\partial u_y}{\partial \eta} + \zeta_z \frac{\partial u_z}{\partial \zeta} = 0 \quad (3.1.1.3)$$

The discretization of the above equations on a staggered grid are described briefly in Balaras (1995). Here, as an example, discretization of the diagonal convective term in w -momentum equation is shown below:

$$\begin{aligned} \left. \frac{\partial(ww)}{\partial z} \right|_{i,j,k}^w & \approx \zeta_z |k^w \left. \frac{\delta(ww)}{\delta \zeta} \right|_{i,j,k}^w \\ & = \zeta_z |k^w \frac{1}{\Delta \zeta} \left[\frac{w_{i,j,k} + w_{i,j,k+1}}{2} - \frac{w_{i,j,k-1} + w_{i,j,k}}{2} \right] \end{aligned} \quad (3.1.1.4)$$

The diagonal diffusive term can be discretized as:

$$\begin{aligned} \frac{\partial}{\partial z} \left(v \frac{\partial w}{\partial z} \right) \Big|_{i,j,k}^w &\approx \zeta_z |^w_k \frac{\partial}{\partial \zeta} \left(v \zeta_z \frac{\partial w}{\partial \zeta} \right) \Big|_{i,j,k}^w \\ &= \zeta_z |^w_k \frac{1}{\Delta \zeta} \left[\left(v \zeta_z \frac{\delta w}{\delta \zeta} \right) \Big|_{i,j,k+1}^p - \left(v \zeta_z \frac{\delta w}{\delta \zeta} \right) \Big|_{i,j,k}^p \right] \end{aligned}$$

where

$$\left(v \zeta_z \frac{\delta w}{\delta \zeta} \right) \Big|_{i,j,k+1}^p = \frac{v |_{i,j,k} + v |_{i,j,k+1}}{2} \zeta_z \Big|_{k+1}^p \frac{w |_{i,j,k+1} - w |_{i,j,k}}{\Delta \zeta}$$

and

$$\left(v \zeta_z \frac{\delta w}{\delta \zeta} \right) \Big|_{i,j,k}^p = \frac{v |_{i,j,k-1} + v |_{i,j,k}}{2} \zeta_z \Big|_k^p \frac{w |_{i,j,k} - w |_{i,j,k-1}}{\Delta \zeta} \quad (3.1.1.5)$$

Here, $|_{i,j,k+1}^p$ and $|_{i,j,k+1}^w$ means quantities are computed in the storage locations of p and w in the grid, respectively. To estimate the variables between points (where the variable is defined), arithmetic average were performed.

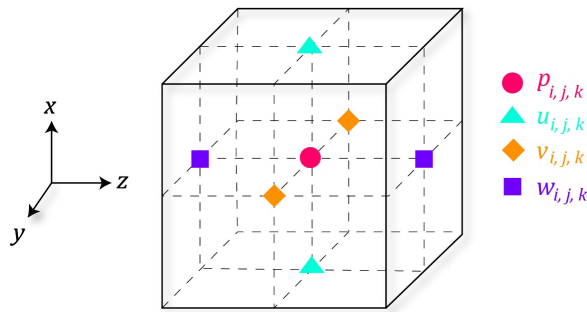


Figure 3.1.1: Velocity and pressure variable arrangement in a cartesian grid

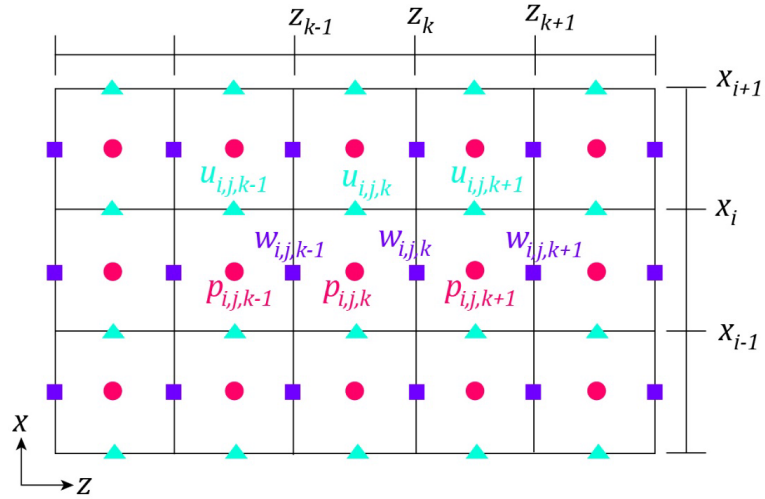


Figure 3.1.2: Staggered grid in x - z plane

After spatial discretization of the Navier-Stokes equations which turn them into a set of algebraic equations for each grid point, time marching is done to obtain solutions for the variables. To obtain a solution at every time step, information up to that time step is required for explicit formulation. Generally, information of previous time step would suffice. On the other hand, implicit formulation requires information about the next time step to calculate values for the current time step. Explicit schemes are simple but have a tendency to be unstable whereas implicit schemes are computationally expensive and unconditionally stable. In this study, a semi-implicit projection method has been used to perform time integration at every time step. In the spanwise direction, all terms are treated implicitly to advance in time using a second-order Crank-Nicholson scheme in order to eliminate restriction to the time step while all other terms are advanced explicitly using a third-order Runge-Kutta scheme. For simplicity, explicit time integration scheme for time integration is described briefly afterwards.

Time integration of the governing equations are carried out using fractional step procedure. In this approach, an intermediate velocity field is initially computed (that does not satisfy continuity equation), then using that intermediate velocity, a virtual scalar quantity is developed which is later used to estimate velocity and pressure field. Either a third order Runge-kutta scheme (RK3) or a second-order Adams-Bashforth (AB2) scheme will be employed for the time integration (explicit). For AB2 method, the procedure is implemented once to advance a step in time whereas for RK3 method, the procedure is done three times (three substeps) to advance one time step. The time integration scheme can be written as:

$$\frac{\hat{u}_i^k - u_i^{k-1}}{\Delta t} = \gamma_k A(u_i^{k-1}) + \rho_k A(u_i^{k-2}) - \alpha_k \frac{\partial p^{k-1}}{\partial x_i} \quad (3.1.3)$$

$$\frac{\delta^2 \phi^k}{\delta x_i \delta x_i} = \frac{1}{\alpha_k \Delta t} \frac{\delta \hat{u}_i^k}{\delta x_i} \quad (3.1.4)$$

$$u_i^k = \hat{u}_i^k - \alpha_k \Delta t \frac{\delta \phi^k}{\delta x_i} \quad (3.1.5)$$

$$p^k = p^{k-1} + \phi^k \quad (3.1.6)$$

where k is the substep index and ranges from 1 to 3 for the Runge-Kutta scheme and is 1 for the Adams-Bashforth scheme. The coefficients $(\alpha_k, \gamma_k, \rho_k)$ of the AB2 scheme can be derived after Taylor series expansion of the time derivative and manipulating the resulting terms; brief description can be found in Moin (2010). The coefficients for the low storage RK3 scheme are obtained by expanding the equation 3.1.3 and determining their relationships among them as well as comparing them with the coefficients of the general third order RK3 scheme. The full method of derivation can be found in Orlandi (2001). Above equations show intermediate velocity (\hat{u}_i^k) is used

to project into a divergence free space by solving the scalar ϕ (equation 3.1.4) as the intermediate velocity does not satisfy continuity equation. The spatial operator A contains convective and viscous terms and Δt is the time step. The RK3 coefficients are:

$$\alpha_1 = \frac{8}{15}, \quad \gamma_1 = \frac{8}{15}, \quad \rho_1 = 0;$$

$$\alpha_2 = \frac{2}{15}, \quad \gamma_2 = \frac{5}{12}, \quad \rho_2 = -\frac{17}{60};$$

$$\alpha_3 = \frac{1}{3}, \quad \gamma_3 = \frac{3}{4}, \quad \rho_3 = -\frac{5}{12};$$

with

$$\sum_{k=1}^3 \alpha_k = \sum_{k=1}^3 (\gamma_k + \rho_k) = 1$$

and AB2 coefficients are:

$$\alpha_1 = 1, \quad \gamma_1 = \frac{3}{2}, \quad \rho_1 = -\frac{1}{2};$$

with

$$\alpha_1 = \gamma_1 + \rho_1 \tag{3.1.1.6}$$

For explicit formulations, numerical scheme has to be stable so that the errors do not amplify at each subsequent time step. To ensure that, timestep length is constrained so that the distance that information propagates within this timestep must be lower than the distance between mesh nodes. The following stability criterion (or the generalized CFL number including the time step constraint from the viscous terms) is conserved:

$$CFL = \Delta t \left[\frac{|u|}{\Delta x} + \frac{|v|}{\Delta y} + \frac{|w|}{\Delta z} + 2\nu \left(\frac{1}{\Delta x^2} + \frac{1}{\Delta y^2} + \frac{1}{\Delta z^2} \right) \right] \quad (3.1.1.7)$$

In this study, for the RK3 scheme, CFL number was 1.1, whilst using AB2 scheme, the CFL number was 0.6.

3.1.2 Poisson solver

It is apparent from the incompressible momentum and continuity equations that pressure and velocity are not coupled. To resolve this issue, divergence of momentum equation is taken and using the continuity equation, pressure poisson equation is developed which couples velocity and pressure. The poisson equation in cartesian coordinates is:

$$\left(\frac{\delta^2}{\delta^2 x} + \frac{\delta^2}{\delta^2 y} + \frac{\delta^2}{\delta^2 z} \right) \phi_{i,j,k} = f_{i,j,k} \quad (3.1.7)$$

where $\phi = p^n - p^{n-1}$ and n is the substep index for RK3 or AB2 scheme and f denotes to the RHS of equation 3.1.4. In computational space, the discretized form of the above equation (equation 3.1.7) is:

$$\begin{aligned} & \xi_x |_i^p \frac{1}{\Delta \xi^2} \{ [\xi_x |_i^u (\phi_{i+1,j,k} - \phi_{i,j,k})] - [\xi_x |_{i-1}^u (\phi_{i,j,k} - \phi_{i-1,j,k})] \} \\ & + \eta_y |_j^p \frac{1}{\Delta \eta^2} \{ [\eta_y |_j^v (\phi_{i,j+1,k} - \phi_{i,j,k})] - [\eta_y |_{j-1}^v (\phi_{i,j,k} - \phi_{i,j-1,k})] \} \\ & + \zeta_z |_k^p \frac{1}{\Delta \zeta^2} \{ [\zeta_z |_k^w (\phi_{i,j,k+1} - \phi_{i,j,k})] - [\zeta_z |_{k-1}^w (\phi_{i,j,k} - \phi_{i,j,k-1})] \} \\ & = f_{i,j,k} \end{aligned}$$

Or

$$\begin{aligned} & am_i \phi_{i-1,j,k} + bm_i \phi_{i,j,k} + cm_i \phi_{i+1,j,k} + al_j \phi_{i,j-1,k} + bl_j \phi_{i,j,k} + cl_j \phi_{i,j+1,k} \\ & + an_k \phi_{i,j,k-1} + bn_k \phi_{i,j,k} + cn_k \phi_{i,j,k+1} = f_{i,j,k} \end{aligned} \quad (3.1.8)$$

with the coefficients

$$am_i = \frac{1}{\Delta \xi^2} \xi_x \Big|_i^p r_u \Big|_{i-1} \xi_x \Big|_{i-1}^u$$

$$cm_i = \frac{1}{\Delta \xi^2} \xi_x \Big|_i^p r_u \Big|_i \xi_x \Big|_i^u$$

$$bm_i = -am_i - cm_i$$

$$al_j = \frac{1}{\Delta \eta^2} \eta_y \Big|_j^p \eta_y \Big|_{j-1}^v$$

$$cl_j = \frac{1}{\Delta \eta^2} \eta_y \Big|_j^p \eta_y \Big|_j^v$$

$$bl_j = -al_j - cl_j$$

$$an_k = \frac{1}{\Delta \zeta^2} \zeta_z \Big|_k^p \zeta_z \Big|_{k-1}^w$$

$$cn_k = \frac{1}{\Delta \zeta^2} \zeta_z \Big|_k^p \zeta_z \Big|_k^w$$

$$bn_k = -an_k - cn_k \tag{3.1.2.1}$$

Equation 3.1.8 is solved using a combination of fast Fourier Transform (FFT) (Swarztrauber,1984) solver which performs FFT in the spanwise direction (y) then solves the system of linear equations using a direct solution procedure. Using FFT, we assume the flow is homogenous and periodic in the y direction; thus, grid should be

uniform in that direction. To perform FFT, equation 3.1.7 is transformed into a set of 2D Helmholtz equations in the uncoupled wave number space:

$$\left(\frac{\delta^2}{\delta^2 x} + k_{l'} + \frac{\delta^2}{\delta^2 z} \right) \phi_{i,j,k} = f_{i,j,k} \quad (3.1.9)$$

where $k_{l'}$ is the modified wave number and defined as:

$$k_{l'} = \frac{2}{\Delta y^2} \left[1 - \cos \left(\frac{2\pi l}{N_y} \right) \right]$$

Here, N_y is the number of grid cell in the y direction (not including ghost cells (see section 4.2)), l is the wave number and Δy the grid size in the y direction. Equation 3.1.8 can be rewritten as:

$$\begin{aligned} am_i \hat{\phi}_{i-1,l,k} + \left(bm_i - \frac{k_{l'}}{r_p^2 |i} \right) \hat{\phi}_{i,l,k} + cm_i \hat{\phi}_{i+1,l,k} \\ + an_k \hat{\phi}_{i,l,k-1} + bn_k \hat{\phi}_{i,l,k} + cn_k \hat{\phi}_{i,l,k+1} = \hat{f}_{i,l,k} \end{aligned} \quad (3.1.10)$$

The equation 3.1.10 is solved for each wavenumber using the “BLKTRI” routine from the FISHPACK library, which is a generalized cyclic reduction algorithm (solves large linear system of equations by repeatedly splitting the problem and eliminating odd or even numbers of rows/columns of a matrix at every step) (Swarztrauber,1974).

3.2 Boundary conditions

Boundary conditions are a set of mathematical relations that are needed to be imposed at the boundaries of a numerical domain to obtain a solution for any boundary value problem. In this study, to apply boundary conditions, ghost cell

approach was employed. Ghost cells are cells in the solid (where the flow intersect with the body/wall/structure) that have at least one neighbor in the fluid; the values of these cells are set at the beginning of every time step so that the values in the interior fluid cells can evolve based on them. An advantage of this approach is that numerical algorithm near the boundaries remain the same as for the interior cells. Also, parallelization of the code is easier in this way via domain decomposition technique which is employed in this numerical solver (Beratlis, 2008). MPI (message passing interface) library is used to carry out the communications among the processors.

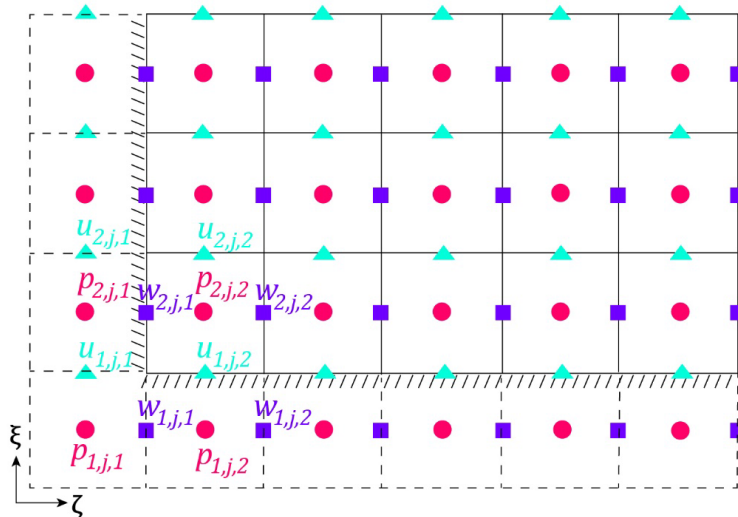


Figure 3.2.1 Implementation of Dirichlet and Neumann boundary conditions

3.2.1 Dirichlet and Neumann boundary condition

Figure 3.2.1 depicts the implementation of Dirichlet and Neumann boundary conditions on the lower left corner of $x - z$ plane ($\xi - \zeta$ in computational space). When the value of a function is specified on a surface, it is known as Dirichlet

boundary condition and in this case, Dirichlet boundary condition for u and w velocity components is being enforced:

$$u_{1,j,k} = u_b \text{ and } w_{i,j,1} = w_b \quad (3.2.1.1)$$

where u_b and w_b are the prescribed normal velocity components on the lower wall and the left wall, respectively.

No-slip boundary conditions for wall tangent components:

$$\begin{aligned} v_t &= \frac{1}{2}(v_{1,j,k} + v_{(2,j,k)}) \text{ or } v_{1,j,k} = 2v_t - v_{2,j,k} \\ w_t &= \frac{1}{2}(w_{1,j,k} + w_{(2,j,k)}) \text{ or } w_{1,j,k} = 2w_t - w_{2,j,k} \end{aligned} \quad (3.2.1.2)$$

where w_t and v_t are the prescribed wall tangential velocity components. For stationary walls, $w_t = 0$ and $v_t = 0$.

For an arbitrary variable (φ), Neumann boundary condition:

$$\frac{\partial \varphi}{\partial n} = f \quad (3.2.1.3)$$

where n is the normal direction of a boundary and f is a known function. This condition can be implemented as (lower boundary in Figure 3.2.1):

$$\varphi_{1,j,k} = \varphi_{2,j,k} - f\Delta x$$

Or

$$\varphi_{1,j,k} = \varphi_{2,j,k} \quad (3.2.1.4)$$

for homogeneous boundary condition.

3.2.2 Convective boundary condition

The outflow boundary condition must allow the fluid to exit the domain without distorting the flow by interacting with the boundary. In this regard, convective outflow boundary condition eliminates distortions associated with the flow structures near the boundary in the computational domain by making the flow “non-reflecting”. This scheme was proposed by Orlanski (1976) which was found to generate stable results if the convection speed is close to the group velocity of the flow (Bostrom, 2015). This method assumes the flow to be purely advective near the boundary and can be written as:

$$\frac{\partial u_i}{\partial t} + U_{conv} \frac{\partial u_i}{\partial z} = 0 \quad (3.2.1)$$

where U_{conv} is the convective velocity which is determined by calculating the mean streamwise velocity and is updated at every time step to conserve mass. To discretize the equation 3.2.1, explicit Euler scheme in time was used. For streamwise velocity component, equation 3.2.1 was discretized using backward difference formula and for the other velocity components, central difference formula was employed.

3.2.3 Periodic boundary condition

As mentioned earlier, the flow must be periodic in the spanwise direction (y) to implement the equation 3.1.9 (Poisson solver). For this purpose, two boundary faces have to be treated in such a way that they are physically connected. Figure 3.2.2 shows the implementation of the periodic boundary condition where, in $\xi - \zeta$ plane,

solution values from the left side are copied to the ghost cells (dashed cells) on the right side and vice versa. It can be written as:

$$\begin{aligned} u_{i,j,N_z+2} &= u_{i,j,2}, v_{i,j,N_z+2} = v_{i,j,2}, w_{i,j,N_z+2} = w_{i,j,2}, p_{i,j,N_z+2} = p_{i,j,2} \\ u_{i,j,1} &= u_{i,j,N_z+1}, v_{i,j,1} = v_{i,j,N_z+1}, w_{i,j,1} = w_{i,j,N_z+1}, p_{i,j,1} = p_{i,j,N_z+1} \end{aligned} \quad (3.2.3.1)$$

In this way, the cyclic situation of the flow across the boundary surface is enforced.

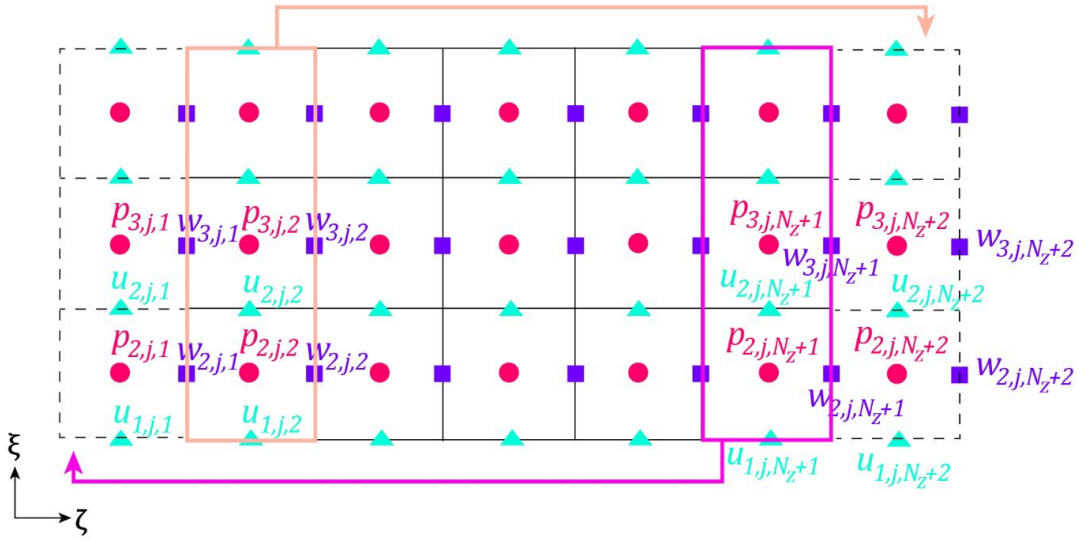


Figure 3.2.2: Implementation of periodic boundary condition

3.3 Embedded boundary method

For complex boundaries (such as bird wing), special treatment is required to use cartesian grid solvers as the grid lines do not align with the geometry. In this work, to establish the interface-grid relation, a front (fluid-solid interface) tracking scheme (Udaykumar *et al.*, 1999) was used. Methods that use marker points to track the location of the interface are referred to as front tracking methods. In this approach,

the interface has to be defined with a series of marker points, then the interface-grid relation has to be defined.

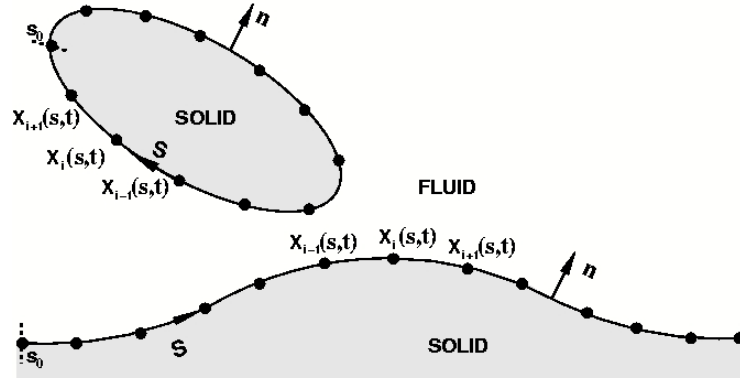


Figure 3.3.1: The parametrized description of interfaces of arbitrary shapes using marker particles (Yang, 2005).

Figure 3.3.1 shows an example of 2D fluid-solid interface marked by equally spaced (similar spacing as the local grid size) marker particles. The geometry of any arbitrary body (i.e., CAD geometry) can be defined using the series of marker points of which the coordinates are known ($\vec{X}(s, t)$, s is the arc-length coordinate). The arclength coordinates are defined in such a way that the fluid is always on the left side of the observer as one travels forward along the arclength. A quadratic polynomial can be written for a marker point coordinate (i) by curve fitting with the two neighboring particles ($i+1$ and $i-1$):

$$x(s) = a_x s^2 + b_x s + c_x \text{ and } y(s) = a_y s^2 + b_y s + c_y \quad (3.3.1)$$

The coefficients ($a_{x,y}, b_{x,y}, c_{x,y}$) for each marker point are determined by fitting the polynomial with neighboring points. The normal from any point on the interface is calculated as:

$$n_x = -\frac{y_s}{\sqrt{x_s^2 + y_s^2}} \text{ and } n_y = -\frac{x_s}{\sqrt{x_s^2 + y_s^2}} \quad (3.3.2)$$

where x_s and y_s are derivative of $x(s)$ and $y(s)$ with respect to s .

$$x_s = 2a_x s + b_x \text{ and } y_s = 2a_y s + b_y \quad (3.3.3)$$

For three-dimensional interface bi-spline fitting is used. After defining the interface with a series of marker particles, the relationship between interface and the Eulerian grid has to be defined. The tagging process (selection of solid and fluid points in the cartesian grid based on the interface co-ordinates) is summarized below:

- A subdomain around the geometry is (figure 3.3.2a) chosen which encloses all the co-ordinates of the solid body. The points outside of this subdomain are tagged as fluid points.
- For each Eulerian grid point, closest marker particle (s_b) is identified by building a vector (\vec{r}) from the marker particle and calculating the dot product between it and the normal (equation 3.3.2). If the dot product results in negative in value, the grid point is assigned as solid/body point (-1) otherwise it is a fluid point (1) (Figure 3.3.1).

To apply the boundary conditions, boundary points or forcing points are needed where velocity will be reconstructed (because the Eulerian grid points does not coincide with the interface marker points). The boundary points are defined as those points in the subdomain which have at least one neighboring solid point. Figure 3.3.2 and 3.3.3 illustrates the result of the tagging process (fluid points, solid points and forcing points identified). For a stationary body, these points are flagged once at the

beginning of solution procedure but for a moving body this process is repeated at every time step.

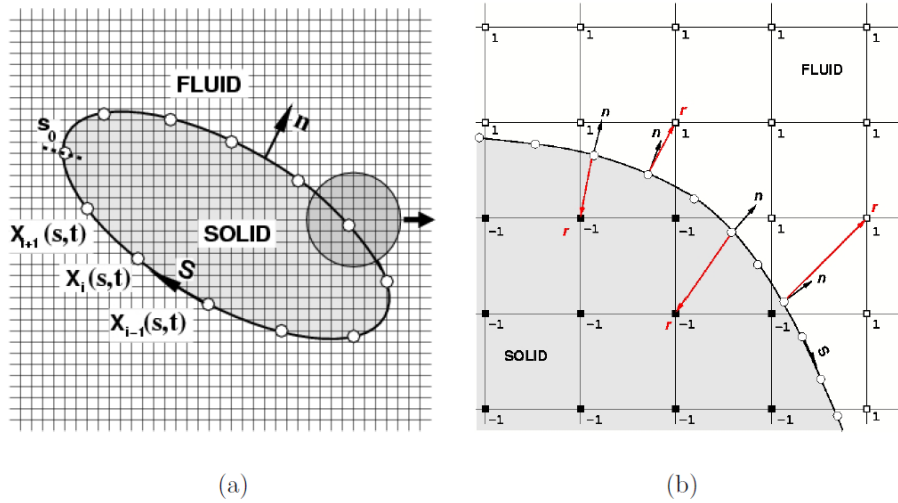


Figure 3.3.2: Relation between interface and Cartesian grid (a) a parametrized elliptical body immersed in fluid (b) a zoom-in view of the body where tagging process is shown. Here, \blacksquare solid points; \square fluid points (Yang, 2005)

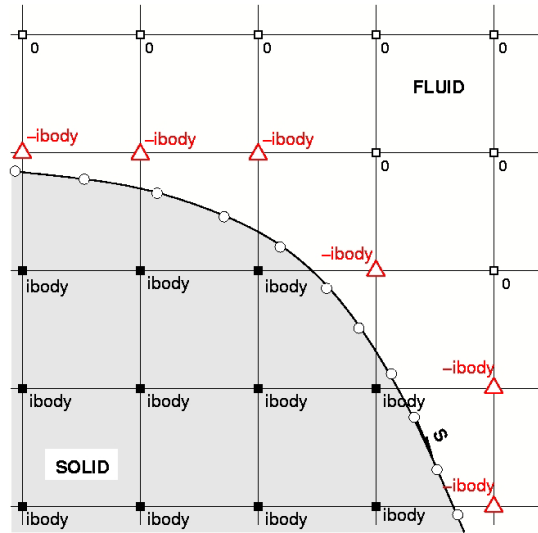


Figure 3.3.3: Illustration of \blacksquare body points, Δ forcing points and \square fluid points (Yang, 2005)

Suppose an interface's (Ψ) marker points coincide with Eulerian grid points and a Dirichlet boundary condition (u_Ψ) is to be imposed on the interface grid points. It is done by setting $\hat{u}_i^k = u_\Psi$ and solving for an external forcing function (f_i^k) using equation 3.1.3:

$$f_i^k = \frac{u_\Psi - u_i^{k-1}}{\Delta t} - RHS_i^k \quad (3.3.1.1)$$

Here, RHS is RHS of equation 3.1.3. Using this forcing function in equation 3.1.3:

$$\frac{\hat{u}_i^k - u_i^{k-1}}{\Delta t} = \gamma_k A(u_i^{k-1}) + \rho_k A(u_i^{k-2}) - \alpha_k \frac{\partial p^{k-1}}{\partial x_i} + f_i^k \quad (3.3.1.2)$$

This will impose the Dirichlet boundary condition on the predicted velocity field. But Eulerian grid rarely coincides with geometry. So, f_i^k must be calculated on the forcing points that are nearest neighbors of the interfacial marker points and u_Ψ is not known there which has to be interpolated based on the interface and surrounding velocity field. The velocities at the forcing points need to be reconstructed and this is done by interpolating using the two surrounding fluid points along the normal of the body. To calculate the normal from the forcing point to the body:

$$\begin{aligned} \frac{x_i - x_n}{\sqrt{(x_i - x_n)^2 + (y_j - y_n)^2}} &= n_x = \frac{-y_s}{\sqrt{(x_s^2 + y_s^2)}} \\ \frac{y_j - y_n}{\sqrt{(x_i - x_n)^2 + (y_j - y_n)^2}} &= n_y = \frac{x_s}{\sqrt{(x_s^2 + y_s^2)}} \end{aligned} \quad (3.3.4)$$

where (x_i, y_i) is the forcing point, (x_n, y_n) or s_n is the point on the body where the normal from the forcing point intersects. Using equation 3.3.3 to substitute in equation 3.3.4:

$$(x_i - x_n)(2a_x s_n + b_x) + (y_j - y_n)(2a_y s_n + b_y) = 0$$

Or

$$s_n = \frac{-b_x(x_i - x_n) - b_y(y_j - y_n)}{2a_x(x_i - x_n) + 2a_y(y_j - y_n)} \quad (3.3.5)$$

Using equation 3.3.1 to substitute equation 3.3.5 results in:

$$\begin{aligned} & (2a_x^2 + 2a_y^2)s_n^3 + (3a_x b_x + 3a_y b_y)s_n^2 \\ & + (2a_x c_x + 2a_y c_y + b_x^2 + b_y^2 - 2a_x x_i - 2a_y y_j)s_n \\ & + (b_x c_x + b_y c_y - b_x x_i - b_y y_j) = 0 \end{aligned} \quad (3.3.6)$$

Using Newton-Raphson method this equation 3.3.6 is solved iteratively, and the initial guess is the closest interfacial marker point. After s_n is derived, using equation 3.3.1 and 3.3.2, the co-ordinates and the unit normal vector can be obtained.

Figure 3.3.4 shows the interpolation procedure. Here, using the magnitudes in point 1 (interface-normal intersection point) as well as surrounding two fluid points (2 and 3), interpolation is performed to obtain magnitudes in the forcing point. The fluid points can be either along the diagonal or x or z grid lines of the cell containing the forcing point. Any variable ϕ in two-dimensional space (shaded area, Figure 3.3.4) can be written as:

$$\phi = b_1 + b_2 x + b_3 y \quad (3.3.7)$$

The coefficients (b_1, b_2, b_3) can be obtained after solving the following equation:

$$\begin{bmatrix} b_1 \\ b_2 \\ b_3 \end{bmatrix} = A^{-1} \begin{bmatrix} b_1 \\ b_2 \\ b_3 \end{bmatrix} = \begin{bmatrix} 1 & x_1 & y_1 \\ 1 & x_2 & y_2 \\ 1 & x_3 & y_3 \end{bmatrix}^{-1} \begin{bmatrix} \phi_1 \\ \phi_2 \\ \phi_3 \end{bmatrix} \quad (3.3.1.3)$$

where A is the co-ordinates of three points as shown in figure 3.3.3.

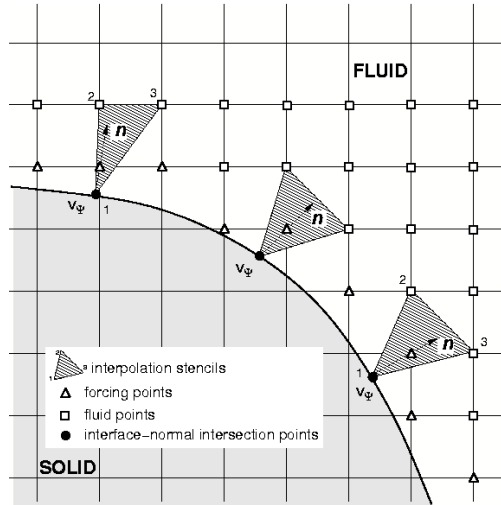


Figure 3.3.4: Interpolation procedure at the forcing point (Yang, 2005)

For stationary body, this procedure is done at the beginning of the simulation only and the values are stored in memory but for moving boundaries, this step is done at every time step as the locations of boundary points change every time step. The procedure can be extended for three-dimensional applications by adding an extra term (b_4z) in equation 3.3.7 then solving the next equation.

3.4 Validation of the numerical solver

The code has been validated for numerous cases in a similar Reynolds number range as is adopted in current study, for example, flapping foils (Rahromostaqim *et al.* 2016), rotating foils (Posa *et al.* 2016; Posa and Balaras 2018), and bluff bodies (Posa

and Balaras 2016; Pal *et al.* 2017). To show examples, two cases are listed briefly in the subsequent sections.

3.4.1 Validation case: flow over a 2D cylinder

Numerical simulations of flow over a 2D cylinder at different Reynolds numbers were conducted to evaluate the accuracy of the solver. The computational domain for this analysis is shown in Figure 3.4.1 which is based on the study conducted by Posdziech and Grundmann (2007). The number of grid points in the computational domain was $240 \times 3 \times 412$ ($N_x \times N_y \times N_z$) in the cross-stream (x), spanwise (y), and streamwise (z) directions, respectively. The resolution of the grid near the cylinder was set to $0.009D$. A section of the grid (x-z plane) around the cylinder is shown in Figure 3.4.2.

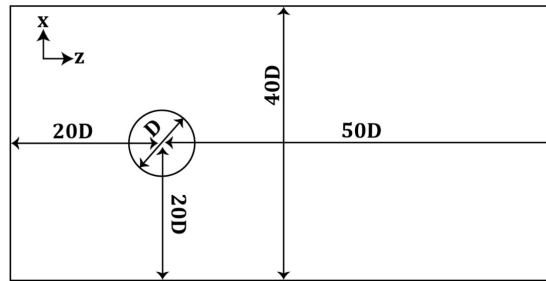


Figure 3.4.1: Computational domain around the cylinder of diameter, D

Table 3.4.1: Comparison of drag coefficients

| Cases | Reynolds Number | Drag coefficient (C_d) |
|--------------------------------|-----------------|----------------------------|
| Current study | 20 | 2.0354 |
| | 40 | 1.5119 |
| Posdziech and Grundmann (2007) | 20 | 2.0786 |
| | 40 | 1.5484 |

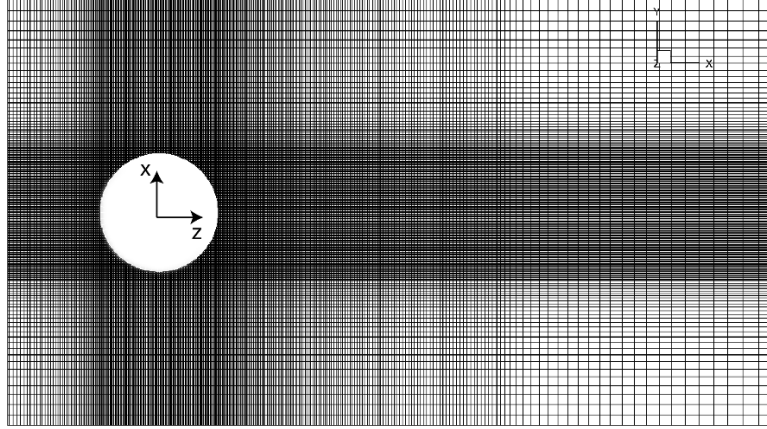


Figure 3.4.2: A section of the computational grid around the cylinder in the x - z plane. Here, x denotes to cross-stream direction and z denotes to streamwise direction.

Taking the cylinder diameter (D) as the characteristic length and the freestream velocity (U_∞) to be unity, Reynolds number of 20 and 40 were adopted, and the drag coefficients were compared (Table 3.4.1) with the study conducted by Posdziech and Grundmann (2007). For both cases, the coefficients are within 5% of the benchmark values (Table 3.4.1). The spanwise vorticity contours for both cases ($Re=20$ and $Re=40$) are shown in Figure 3.4.3. In both cases, the flow reaches steady state and a pair of stationary recirculating wake (stationary counter-rotating vortex pair) forms downstream, which also conforms to the results provided by Lee (2017). As Reynolds number increases, separation point moves upward behind the cylinder, recirculation zone also increases in size (Figure 3.4.3). If the Reynolds number is increased further (~ 100), von Karman shedding will ensue.

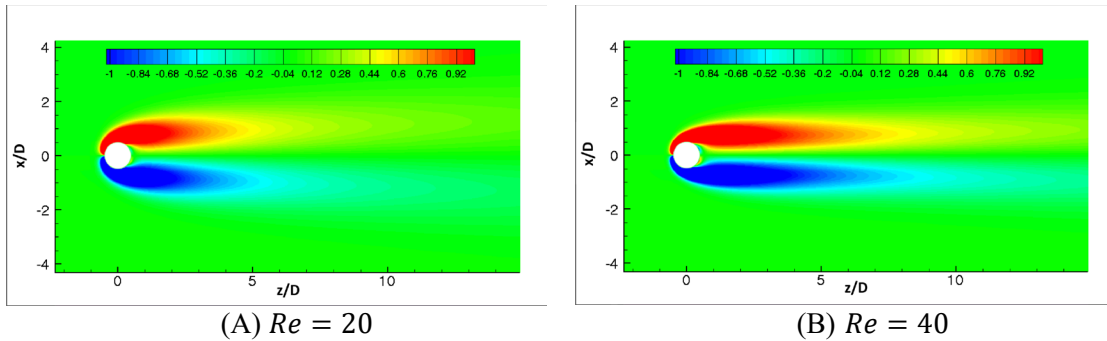


Figure 3.4.3: Spanwise vorticity (ω_y) contour in the vicinity of the cylinder at (A) $Re=20$ and (B) $Re=40$. Here, x denotes to cross-stream direction and z denotes to streamwise direction.

3.4.2 Validation case: two-dimensional (2D) flow over an Eppler airfoil

Unlike symmetrical airfoils (i.e., NACA 0012), birds' wing cross-sections are highly cambered, and it varies in size from the root to the tip (Shy *et al.*, 2007). As an example, owl's airfoil (see section 4.1) shown in next chapter is extremely cambered. Although increased camber introduces lift augmentation, it is also associated with early flow separation (as a result, increased form drag is generated). The flow field of a cambered airfoil differs significantly compared to a symmetric one. Validation data

for the flow field of an Eppler airfoil (Eppler 387, max camber 3.2% of chord) is presented and compared with the existing literatures hereinafter.

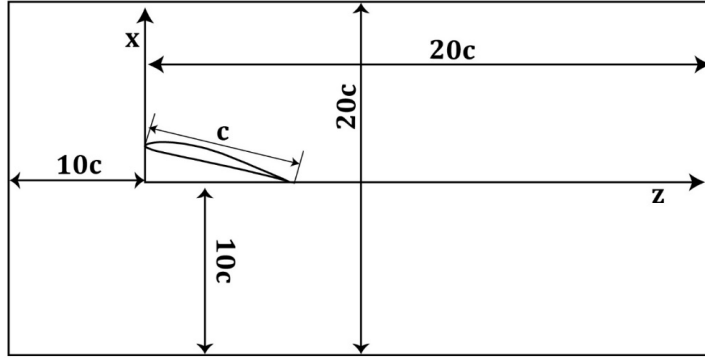


Figure 3.4.4: Computational domain around the airfoil; here, c denotes to chord length, x is cross-stream direction and z denotes to streamwise direction.

Figure 3.4.4 shows the extent of the computational domain in the x - z plane. The domain size as well as the grid resolutions were chosen to match the setup used in the study by Rahromostaqim *et al.* (2016). The spanwise extent was $20c$ and the number of grid points

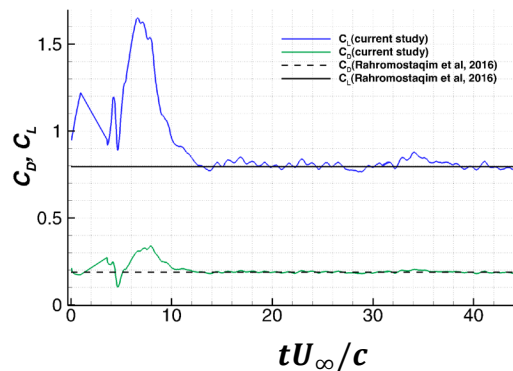


Figure 3.4.5: Comparison of lift coefficient (C_L) and drag coefficient (C_D) over non-dimensional flow time (tU/c)

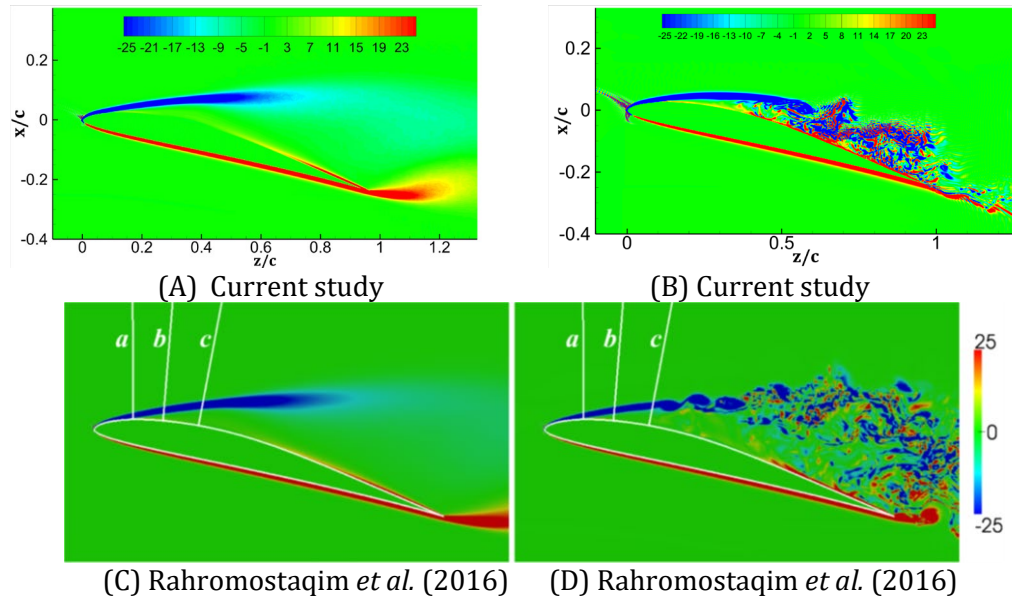


Figure 3.4.6: Comparison of spanwise vorticity contours (ω_y) between the current study and Rahromostaqim *et al.* (2016). The data are displayed on x - z plane; (A) and (C) are time-spanwise averaged ω_y ; (B) and (D) are instantaneous ω_y .

in the computational domain was $608 \times 202 \times 1002$ ($N_x \times N_y \times N_z$) in the cross-stream, spanwise, and streamwise directions, respectively. The chord-based Reynolds number for this study was 30,000 and the wing was fixed at 14° angle of attack. Our simulation results are in close agreement with the study by Rahromostaqim *et al.* (2016). Figure 3.4.5 shows the comparison of drag (C_D) and lift (C_L) coefficients between the current study and the reference. For both the coefficients, the values converge to the reference values from the study by Rahromostaqim *et al.* (2016). We also compare the spanwise vorticity contours (ω_y) and we see similar distribution of vorticity over the wing (Figure 3.4.6).

Chapter 4

Computational setup

Feathers of different size and shapes constitute a bird's wing. Hence, the surface structure of a bird wing is not entirely smooth unlike an aircraft wing. Moreover, the presence of other aspects such as alula, down feathers, etc. yield a significant difference between a bird wing and an artificial wing. In this regard, owl wing comprises further complexities due to the presence of distinct wing microfeatures such as LE serrations/combs, TE fringes, velvety feathers, etc. To understand the flow physics of each microstructure, segregation is required so that the applicability of each individual component can be configured for specific purposes such as in UAV wings. Therefore, in this thesis research, the impact of LE serrations on the flow field of an owl wing is considered exclusively; configured at a higher AOA (20°) inspired by the research work of Kroger *et al.* (1972), Anderson (1973) and Geyer *et al.* (2017) where they suggested that serrations are effective mostly at high angles of attack when the boundary layer separation is predominant. For computational purpose, a DNS solver (discussed in the previous chapter 3.0) is utilized which will simulate the fluid flow around the solid body, which is an owl wing geometry in our case. The wing geometry as well as the accurate representation of the LE serrations are required for

the simulation setup which were modeled based on several studies which will be discussed briefly in the next section.

4.1 Owl wing model

The airfoil used in this study is a generic owl airfoil (Liu *et al.*, 2006) which was also used in the study by Beratlis *et al.* (2020) to simulate the flapping flight of an owl. This airfoil has also been utilized in the experimental study by Anyoji *et al.* (2018). The owl airfoil can be characterized by high camber and very low thickness near the trailing edge (see figure 4.1.1). The surface of the owl wing is smooth in this study unlike a real owl wing which is covered with elongated pennulae (velvety surface). The leading-edge (LE) serrations were modeled separately and then, assembled with the 3D wing which was modeled from the owl airfoil (Figure 4.1.2). The LE serrations have been modeled based on the data from the study by Bachmann and Wagner (2011). They estimated three-dimensional shape of the natural serrations of a Barn owl wing using confocal laser scanning microscopy. In this study, we utilize their first order approximation to model the serration shapes and orientations along the leading edge of our model wing (Figure 4.1.3).



Figure 4.1.1: Profile of the owl airfoil extracted from Liu et al. (2006)



Figure 4.1.2: Leading-edge serrations assembled with the 3D owl wing

Owls have leading-edge serrations of different sizes and shapes which varies species to species; however, the larger species have larger serrations (Weger and Wagner, 2016). Also, the lengths of the serrations are not same across the span of a species (i.e., from the mid span to the wing tip). The average length of serrations for a Barn owl wing is $2670\mu m$ and the gap between two neighboring serrations is $575\mu m$ while the mean wing chord being approximately 17.1 cm (Bachman, 2010; Jaworski and Peake, 2019). The tilt angle and inclination angle (figure 4.1.3) of each serration vary by $1^\circ - 3^\circ$ across the span; on average, the tilt angle and inclination angle are 36° and 29° , respectively. The width (w_s) and thickness (t_s) of a serration can be described with: $w_s = 0.2067s + 640$ and $t_s = 0.0149s + 86$ where s denotes to length of serration from its root (Bachmann and Wagner, 2011). Their flight Reynolds number also varies based on their flight speed (2.5 m/s – 7.0 m/s) (Wagner *et al.*, 2017) which amounts to a chord-based flight Reynolds number range of 30,000 to 90,000.

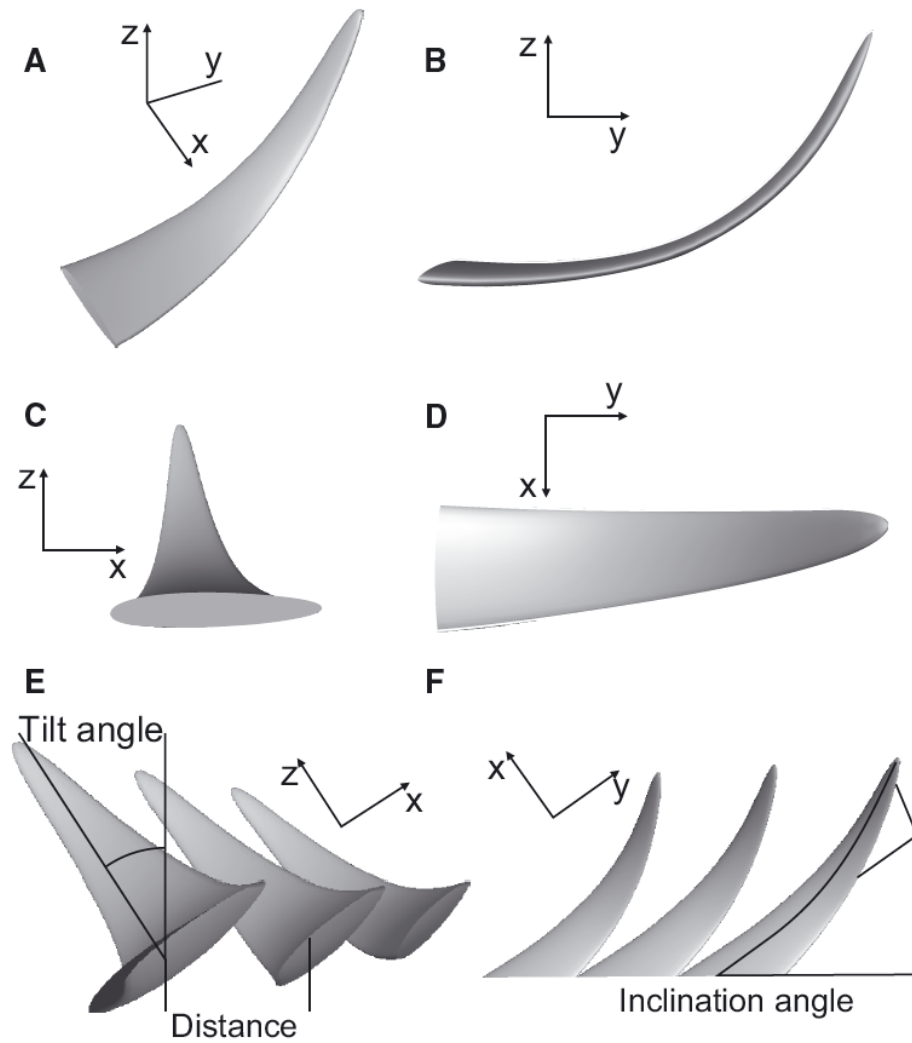


Figure 4.1.3: Schematic of a first-order approximation of a serration in different views (A–D). (E) Tilt angle and distance. (F) Inclination angle towards the leading edge of a wing (Bachmann and Wagner, 2011).

From Kroger *et al.*'s (1972) experimental study with real owl wings (which was later revisited by Anderson (1973)), it was suggested that serrations are particularly effective at delaying stall as much as until 30-degree AOA. However, real owl wings were used for the experiments which had surface features, alula, slotted wingtip, etc.

intact which may have additional effects on the flow downstream the leading edge. Geyer *et al.* (2017) reported aerodynamic performance increase at 20° AOA due to the presence of serrations (using prepared Barn owl wing). Therefore, in this research, serration induced alteration of flow dynamics at a large AOA is investigated with an intermediate Reynolds number in order to assess the effectiveness of serrations in delaying stall (i.e., mitigating flow separation). For the current setup, 20° AOA was chosen and the chord-based Reynolds number was set to be 40,000. This high AOA configuration represents birds' landing, prey-capture phase (Norberg, 2012), hence, will demonstrate large scale flow separations (stall) and the influence of serrations on the modifications of flow features.

4.2 Computational domain and grid resolution

The choice of computational domain size around the owl wing in this research is based on the study by Beratlis *et al.* (2020). Flapping flight of a great horned owl (GHO) was studied by the authors utilizing the same DNS solver employed in this study. The key difference in terms of the solution process between a moving wing and a non-moving one is that the interface-grid (see section 3.3) tracking scheme is repeated at each timestep in the case of the moving wing while for the non-moving wing, this is done only once at the beginning of the computation. The computational domain around the owl wing in this study is shown in Figure 4.2.1

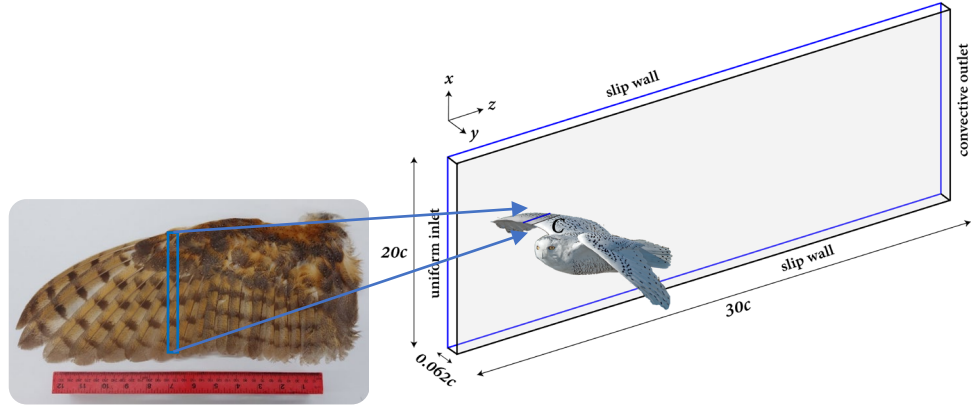


Figure 4.2.1: Computational domain around a section of the owl wing. Here, c denotes to average chord length; z -axis denotes to streamwise direction, x -axis is the cross-stream direction while the spanwise direction is represented by y -axis.

Two cases have been investigated in this setup: with and without serrations (at 20° AOA). The computational domain (shown in Figure 4.2.1) extends to $20c$ (c denotes to average chord length) in the downstream direction from the wing mid-chord and $10c$ in the upstream direction. The vertical extent of the domain is $20c$ while the spanwise length is $0.062c$. The gap between neighboring serrations is very small ($575\mu m$) which necessitates high grid resolutions in the spanwise direction; as a result, the spanwise extent is chosen to enclose 11 serrations resulting in $0.062c$ spanwise domain length to reduce the computational cost. The grid resolution is $1141 \times 402 \times 1202$ ($N_x \times N_y \times N_z$) in this study which is based on the grid convergence study by Beratlis *et al.* (2020). For example, spatial resolution near the wing surface is $0.0015c$ in the streamwise direction and $0.00055c$ in the cross-stream direction. For the cells neighboring the serrations, both streamwise and cross-stream grid resolution is $0.0005c$ (see Figure 4.2.2 and 4.2.3). Grid step size distributions across

the streamwise and cross-stream direction inside the computational domain are shown in Figure 4.2.2. Note that, the LE of the wing starts at location $[0 \frac{z}{c}, 0 \frac{x}{c}]$ while the TE of the wing ends at $[0.95 \frac{z}{c}, -0.34 \frac{x}{c}]$ in the zx plane.

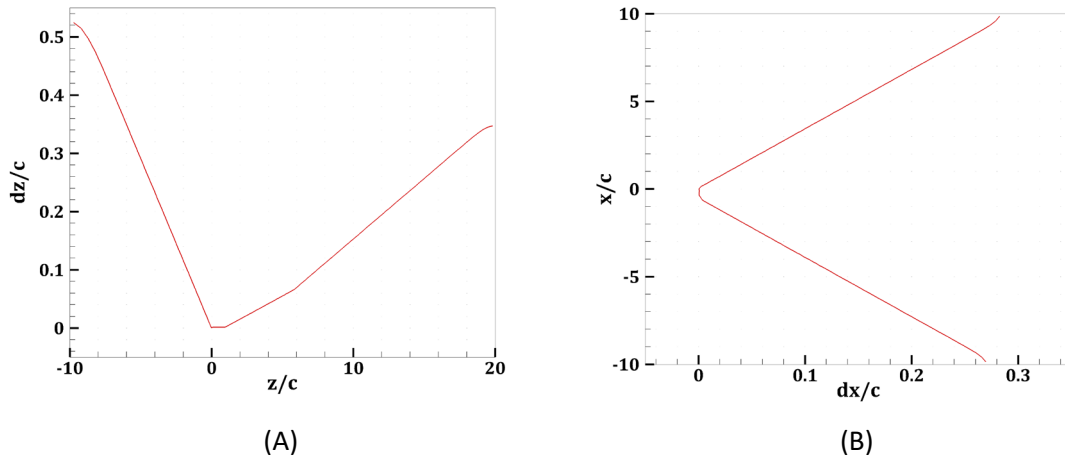


Figure 4.2.2: Non-uniform grid step size in the (A) streamwise (z) direction, and (B) cross-stream (x) direction. Here, dz and dx denote to grid step size in the streamwise and cross-stream direction, respectively. Leading-edge of the wing is at $[0,0]$ while trailing edge ends at $[0.95, -0.34]$ in the zx plane.

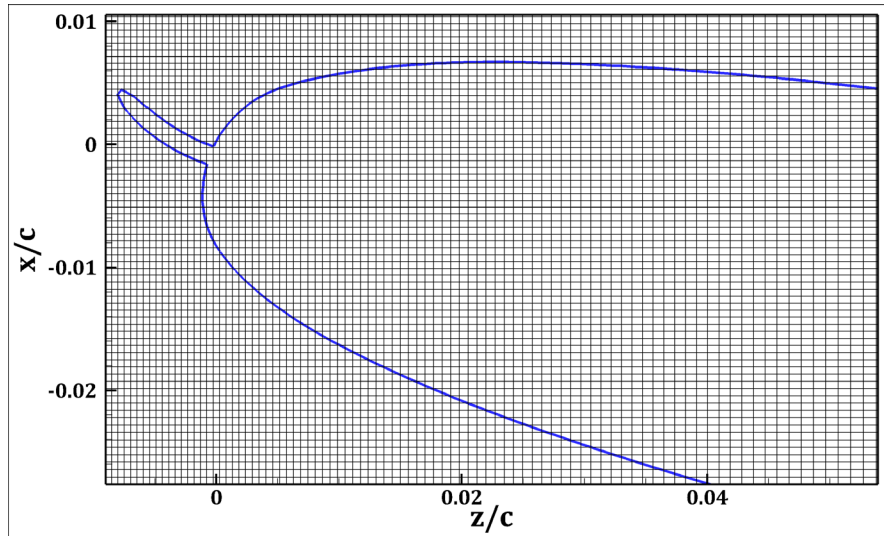


Figure 4.2.3: Cartesian grid around the serrated owl wing in the xz plane

In this research, grid resolution in the spanwise direction was uniform (due to periodic boundary condition, see section 3.2.3) and was set to $0.000155c$. Just to recap, our spanwise domain length is $0.062c$ which is inadequate to resolve some 3D flow phenomena. However, the spanwise grid resolution is capable of capturing three dimensionalities in the flow with some limitations (such as ineffectiveness of capturing the formation of the large stall cells (Taira and Colonius, 2009)). Unlike experimental studies, where end plates (flat plate perpendicularly mounted at the tip of the wing and aligned parallelly with the freestream to obstruct the spanwise flow, preventing formation of tip vortex) are used to improve mean spanwise uniformities (although vortex shedding frequency does not get affected when aspect ratio, $AR \geq 7c \times \sin(AOA)$, where, $AR = \frac{span}{chord}$, see Boutilier and Yarusevych, 2012), numerical simulations utilize periodic boundary conditions to simulate an infinite medium in the spanwise direction. Such practices are to reduce the computational costs and

require large spanwise domain so that the stochasticity of the fully developed turbulent flow in the spanwise direction can be ensured. Hence, the best practice among the researchers is to adopt a spanwise domain length of $0.5c$ for high AOA cases (massive flow separations) and $0.2c$ for low AOA cases (Eisenbach and Friedrich, 2007; Kitosis *et al.*, 2011; Breuer and Jovicic, 2001; Hoarau *et al.*, 2003; Zang and Samtaney, 2016). It is apparent that the spanwise domain extent is not large enough in our case to meet the aforementioned criterion, particularly, large scale 3D flow structures such as stall cells cannot be captured. Hence, this study can be considered as a quasi-3D solution for the current fluid flow problem rather than being capable of fully capturing all 3D flow phenomena. Zang and Samtaney (2016) studied the effects of spanwise AR extensively using DNS at 50000 Reynold number. According to their findings, minimal effects were observed on the mean aerodynamic quantities (mean location of separation and reattachment as well) due to the AR variation, however, turbulent quantities (i.e. Reynolds stress components, budget terms, etc.) were mostly overpredicted in the case of small aspect ratios (AR). Since our study mainly focuses on the comparison of flow physics between the serrated and the smooth leading-edge wing, it will provide insights on the qualitative aspects of the current fluid flow problem despite the limitations with the spanwise extent of the computational domain.

In the next chapter, results obtained from the simulated cases (smooth and serrated) will be briefly discussed and interpreted to shed light on the flow physics associated with owls' gliding flight at high AOA.

Chapter 5

Flow physics

The organization of this chapter is as follows: time-averaged quantities are discussed in section 5.1 to elucidate the impacts of serrations on surface integral quantities as well as the mean flow pattern. Unsteady effects of serrations on the flow field are briefly discussed in section 5.2 while its impacts on turbulence are detailed in section 5.3. This approach will provide us an overall perspective of the flow dynamics alteration via leading-edge serrations. Note that, in the research work, x, y, z denotes to cross-stream, spanwise and streamwise directions, respectively. Similarly, w, u, v are the velocity components. All the results shown in the subsequent sections have been normalized for ease of comparative analyses.

5.1 Time-averaged characteristics

Time averaged lift and drag coefficients for the serrated and smooth case (20° AOA) are shown in table 5.1.1. From the differences between the two cases, we can remark that the footprint of owls' LE serrations on aerodynamic performance are not pronounced even at this AOA. Decrease of aerodynamic performance (by 3.2%) can be observed due to serration; however, production of lift is increased by 2% along with the increase of drag by 5.4%. We have also calculated the skin friction coefficient and the pressure coefficient along the wing surface (see figure 5.1.1) in order to

obtain the spatial distribution of the aerodynamic loads on the wings to look for discrepancies, if exist.

Table 5.1.1: Comparison of aerodynamic force coefficients and dominant frequencies at different AOA's

| Case | Angle of attack | Time-averaged C_L | Time-averaged C_D | $\frac{C_L}{C_D}$ | $St = \frac{fc}{U_\infty}$ |
|-----------|-----------------|---------------------|---------------------|-------------------|----------------------------|
| Serration | 20° | 1.56 | 0.58 | 2.69 | 0.2375 |
| Smooth | 20° | 1.53 | 0.55 | 2.78 | 0.2 |

Figure 5.1.1a (serrated case) and figure 5.1.1b (smooth case) depict the surface contours of time-averaged skin friction coefficient ($\overline{C_f}$) whereas the $\overline{C_f}$ profile comparison is shown in figure 5.1.2b. In figure 5.1.2, the coefficients are extracted from the slice (location indicated with black line over the wing) shown in figure 5.1.2a. Black contour lines on the wings' surfaces in figure 5.1.1a and 5.1.1b denotes to $\overline{C_f} = 0$ (zero-crossings). Comparing the two cases, the skin friction profiles as well as the pressure coefficients ($\overline{C_p}$, figure 5.1.2c) of the lower surfaces are identical since the serration does not appear to impact the lower surface flow at this AOA. However, the upper surface embodies the effects of modified profiles induced by serrations at the leading edge.

It is evident from the upper surface $\overline{C_f}$ profile (figure 5.1.2b) that the flow separates at the leading edge (zone of negative $\overline{C_f}$) and then reattaches close to the leading edge for both cases (0.05 z/c for smooth wing and 0.08 for serrated wing). The $\overline{C_p}$ profiles in this region (0-0.05 z/c for smooth, 0-0.08 z/c for serration) shows nearly constant

profile (pressure plateau) which, after reattachment, have a steeper negative gradient for the serrated case. The regions of favorable (negative) and adverse (positive) pressure gradients can reflect the location of secondary vortices which will be shown in the subsequent sections. From the $\overline{C_f}$ profile of the serrated case, sustained reattached flow is observed from $0.08 z/c$ to $0.5 z/c$ while the smooth wing depicts scattered zones of reattached flow within this separated region which can be referred to secondary separation (Jones *et al.*, 2008). Near the trailing edge, the difference is more prominent as the reattached zone is significantly larger for the serrated wing which is also evident from the favorable pressure gradient at this region (figure 5.1.2b). The magnitude of $\overline{C_p}$ is larger for the serrated case (over almost entire upper surface) compared to the smooth wing which explains higher drag force production as an airfoil at high AOA can be considered as a bluff body and the main drag component will be form drag in that case (Buresti, 2000; Swalwell *et al.*, 2003).

The $\overline{C_f}$ profile over the LSB location has a common shape for airfoils which generally contains a pronounced negative $\overline{C_f}$ peak which indicates transition point (Jones *et al.*, 2008; Klose *et al.*, 2021). In our case, we observe this peak right at the leading edge ($0.0 z/c$) in figure 5.1.2b for both cases which means that the transition point coincides with the separation point. This is also evident from the Reynolds stress, turbulent kinetic energy, etc. which will be shown in the later sections (section 5.3).

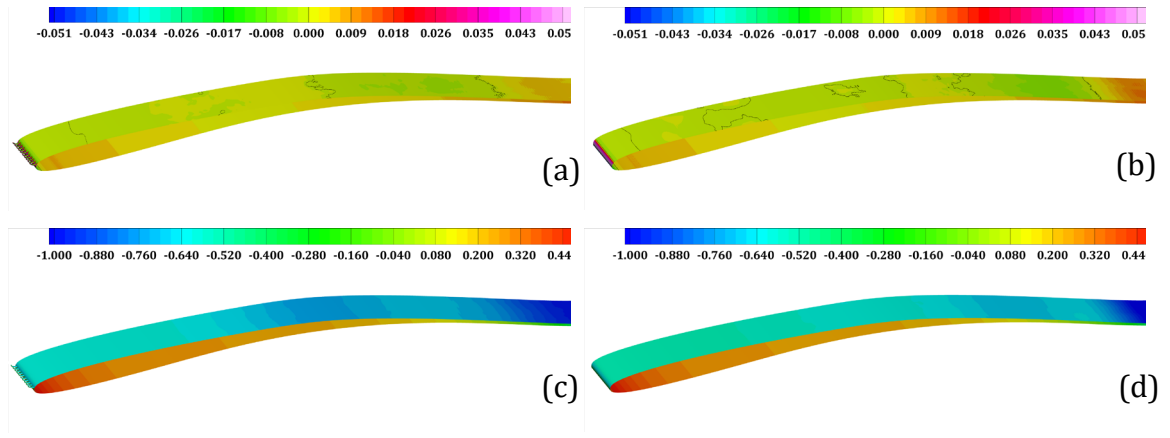


Figure 5.1.1: Contour plots of time-averaged skin friction coefficient, \overline{C}_f : (a) serration (b) smooth; time-averaged pressure coefficient, \overline{C}_p : (c) serration (d) smooth

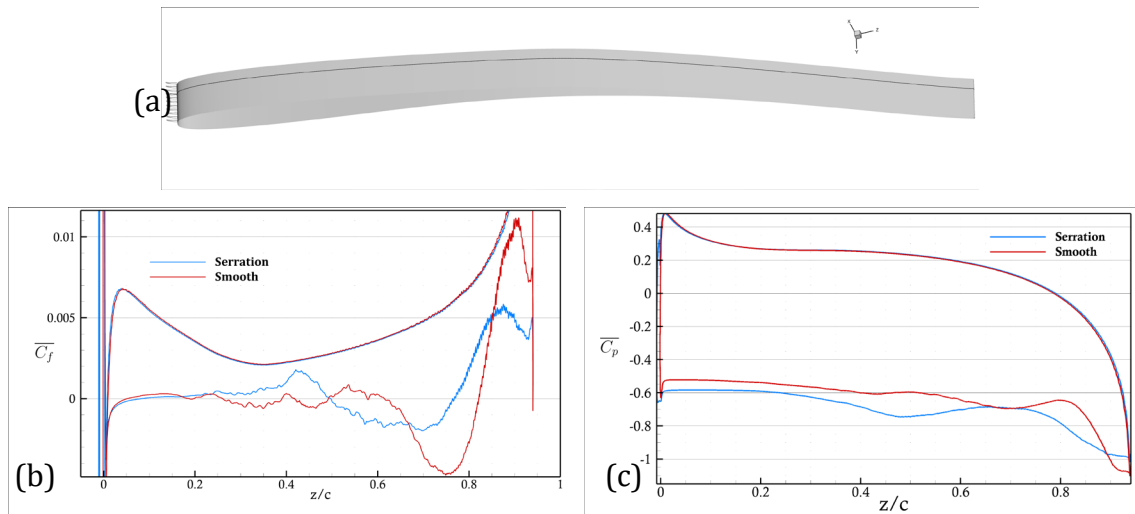


Figure 5.1.2: Comparison of (b) time-averaged skin friction coefficient, \overline{C}_f and (c) time-averaged pressure coefficient, \overline{C}_p . For both cases, the coefficients were taken from a slice (black line) shown in (a). The horizontal axis represents normalized streamwise locations (z/c).

The main flow features associated with the surface contours of $\overline{C_p}$ can be visualized from time and spanwise averaged streamwise velocity ($\langle \overline{w}/U_\infty \rangle$) contours and streamlines colored with velocity magnitudes shown in the figure 5.1.3. The vortex shedding frequencies for both cases (table 5.1.1; $St \sim 0.2$) are similar to bluff body like shedding characteristics (Zaman *et al.*, 1989; Yarusevych *et al.*, 2009) of the flow which originates from the leading-edge separation bubble and so-called trailing edge vortex, and influenced by their interactions (Huang *et al.*, 2001). Note that, there is no universal definition for the term “vortex” (Jeong and Hussain, 1995) but it is generally accepted that a vortex will have spiraling/closed-loop instantaneous streamline pattern with the vortex core having the most concentrated vorticity (Robinson, 1991; Chakraborty *et al.*, 2005). Mean location of both the separation bubble/vortex (SV) and TEV can be observed in figure 5.1.3 for both cases, however, the differences lie in topology (i.e.: size), velocity profiles (i.e.: reverse flow intensity) and other secondary features (i.e. transition location, secondary bubbles, etc.). In regards to the size of the separation bubble, smooth wing’s upper surface depicts a bigger one in comparison to the serrated case. The velocity profiles inside the bubble show much stronger recirculation region for the smooth wing as shown in figure 5.1.4 (S4 – S9) based on time and spanwise averaged streamwise ($\langle \overline{w}/U_\infty \rangle$) velocity profiles. The profiles are taken at several surface normal locations marked as S# shown in figure 5.1.4 (A). From $\overline{C_f}$ profiles (figure 5.1.2a) and velocity profiles, we can see that the flow is attached near trailing edge for both cases; however, the TEV which usually forms due to the shear layer roll-up from the lower surface of the airfoil (Huang *et al.*, 2001) appears to be weaker (figure 5.1.4: S15, S16) in the case of serration. In addition, the

streamlines do not exhibit counter clockwise rotation loop in that region despite having a low velocity vortex core region. This “half saddle” pattern may appear due to leading-edge vortex residing longer in that region than the TEV (Perry and Steiner, 1987). In figure 5.1.1c and 5.1.1d, surface contours of $\overline{C_p}$ shows a noticeable difference at the middle of the wings where serrated case has larger region of low-pressure zone compared to the smooth case. This is due to the presence of secondary vortex in these locations which can be observed in figure 5.1.3c and 5.1.3d. The serrated wing features a larger vortex in this region compared to the smooth case (figure 5.1.4: S7, S8); however, their direction of rotation is the opposite: CCW for serration and CW for smooth case, hence, only the serrated wing shows an attached flow.

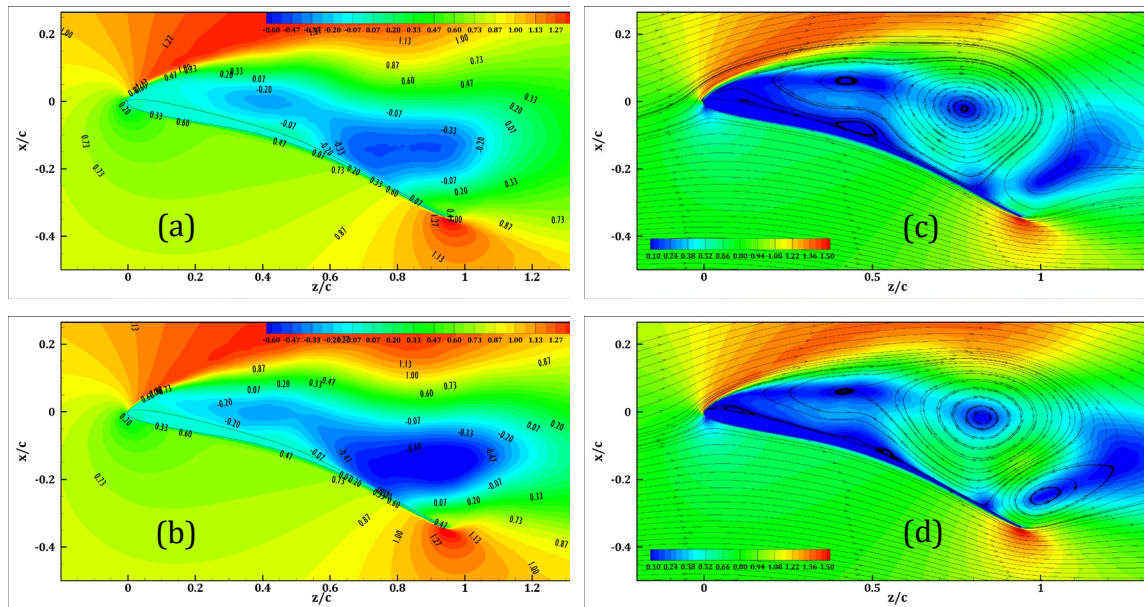


Figure 5.1.3: Time and spanwise averaged streamwise velocity, $\langle \bar{w}/U_\infty \rangle$ for (a) serration, (b) smooth case; streamlines from time and spanwise averaged velocity field for (c) serration, (d) smooth case shown over velocity magnitude contour plot.

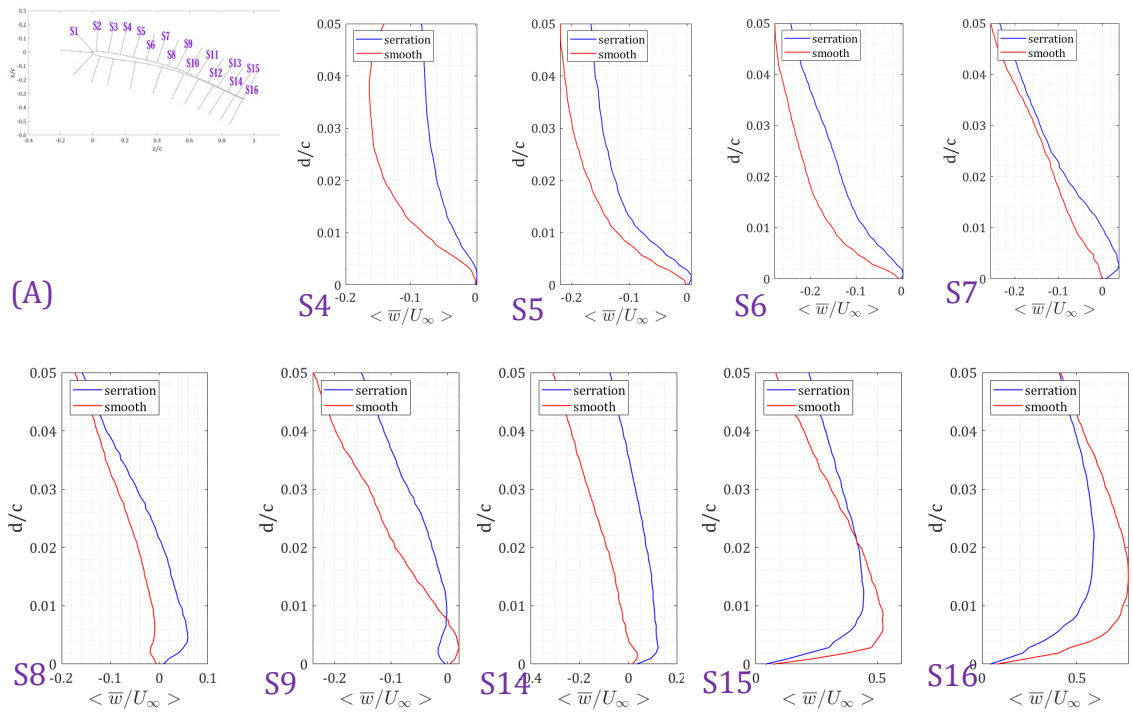


Figure 5.1.4: Wall normal distance (d/c) vs time and spanwise averaged streamwise velocity profiles ($\langle \bar{w} \rangle / U_\infty$) over serrated and smooth wing's upper surface (S4-S16).

Locations of the profiles over the upper surface are shown in (A).

Figure 5.1.5 exhibits time and spanwise averaged spanwise velocity ($\langle \bar{v} \rangle / U_\infty$) isocontours. We observe that serration promotes enhanced spanwise momentum transfer in the immediate downstream vicinity of the serrations. This feature of the flow may be associated with facilitation of LEV stabilization during flapping flight. To stabilize LEV, root-to-tip spanwise flow is required as it contributes to the spanwise advection of vorticity that balances the production of vorticity at the leading edge (Jardin and David, 2014; Ben-Gida *et al.*, 2020). Also, spanwise flow facilitates smooth merging of leading-edge and tip vortex flows (Linehan and Mohseni, 2020). Over the

entire upper surface, significant increase in spanwise momentum transfer can be observed for the serrated wing, especially, near the wall which also signifies increased three-dimensionality in the near wall turbulence (Busse *et al.*, 2015; Huai *et al.*, 2015). Note that the spanwise flow development near LE was also observed in the experimental studies (with real owl wing) conducted by Kroeger *et al.* (1972) and Geyer *et al.* (2017).

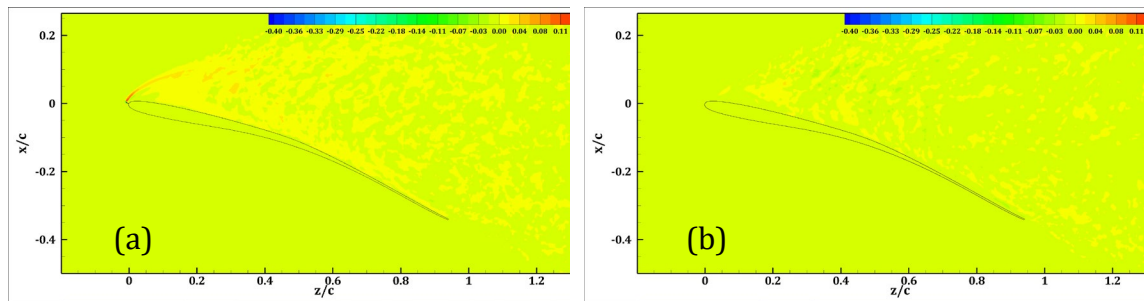


Figure 5.1.5: Time and spanwise averaged spanwise velocity, $\langle \bar{v} / U_\infty \rangle$ for (a) serrated, (b) smooth case

At 20° angle of attack, vortex shedding due to flow separation introduces lift force oscillations on the both wings. The oscillation frequencies are shown in the lift coefficients spectra in Figure 5.1.6 for both the serrated and the smooth wing. The highest energy containing peak is generally associated with the vortex shedding for lifting surface at high angles of attack, whereas, the other dominant frequencies/harmonics are generally associated with periodic merging of rollup vortices, bubble bursting, small-scale vortices impinging on the upper wing surface, etc. (Yarusevych and Boutilier, 2011; Nedic and Vassilicos, 2015; Huang *et al.*, 2011;

Chang *et al.*, 2022). In our case, $St=0.2$ and $St=0.2375$ are the vortex shedding/fundamental frequencies of the smooth wing and the serrated wing, respectively (table 5.1.1). Also, both cases exhibit higher harmonics. For airfoils operating at high angles of attack and low Reynolds numbers, the higher harmonics are generally due to the effect of surface impingement of small-scale vortices generated from the interactions of large-scale vortices such as TE vortex/LE separation vortex (Chang *et al.*, 2022, Pérez-Torró and Kim, 2017).

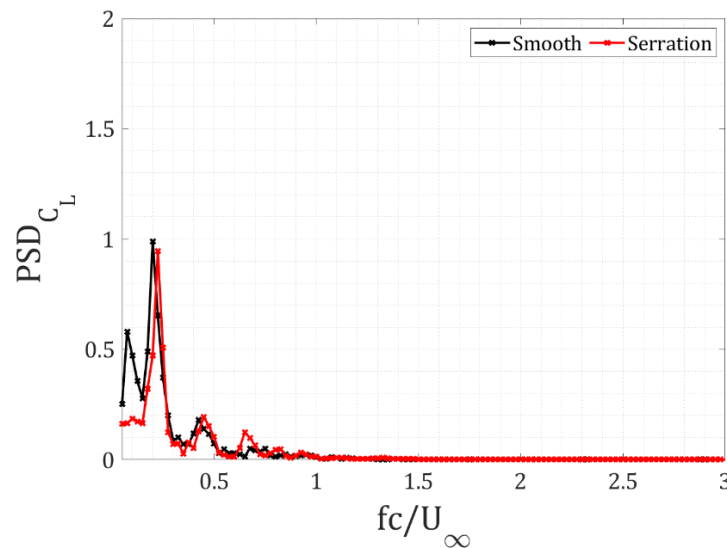


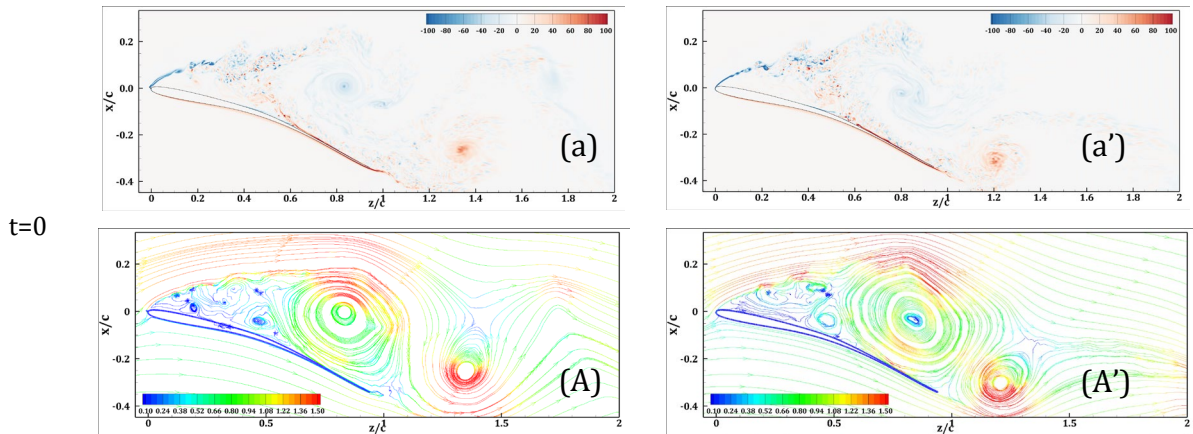
Figure 5.1.6: Frequency spectrum of the lift coefficients (C_L). PSD abbreviates to power spectral density

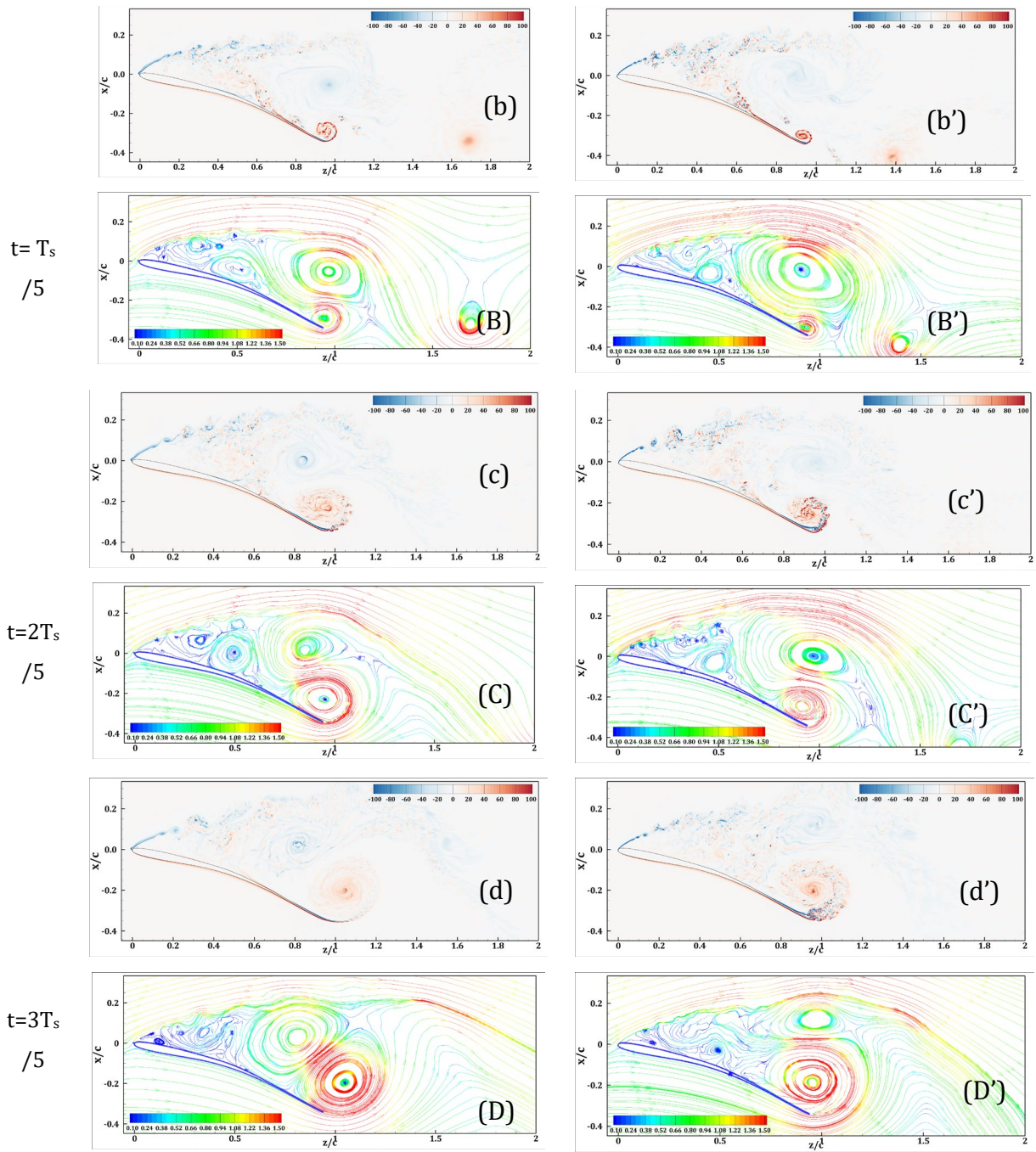
5.2 Instantaneous flow dynamics

Spatial and temporal development of spanwise vortices are shown in Figure 5.2.1. The figure depicts six different phases for both cases during a shedding cycle. The sub-figures are sequenced based on the initiation of TEV formation (Figure 5.2.1, $t=0$)

on the upper surface of the wing. It can be observed that there is a phase difference between the two cases. From $t=0$ and $t=T_s/5$ ($t=5$ as well), we can see that smooth wing develops TEV over the upper surface when the shedded TEV is located further away from the trailing edge compared to the serrated wing. Based on the formation and development of TEV as well as the separation vortex, the whole process for these two cases can be generalized: shear layer generated from leading-edge flow separation rolls up and merges, forming a large CW rotating separation vortex; CCW vortex is also generated at the trailing edge from the rollup of lower and upper surface shear layers. After the shedding event of a TEV, the CW separation vortex grows larger over time (vorticity is fed from the LE shear layer roller vortices), interacts with the other secondary vortex/vortices over the airfoil surface and eventually covers almost half of the aft ward portion of the airfoil (Figure 5.2.1, $t=0$). Afterwards, a new TEV forms again; as it gets bigger in size and strength, it stretches the CW separation vortex, eventually splitting some of its vorticity into the wake which is convected downstream. Meanwhile, the growing TEV entrains fluid from the wake as evident by the saddle point (Cantwell and Coles, 1983), transport it towards the other secondary vortices located at the mid-chord of the airfoil. Eventually, when the TEV grows in size and strength to a certain extent, it gets detached from the upper surface and is convected downstream. The general flow patterns shown in our study for this airfoil at high AOA is in close agreement with the study by Breuer and Jovicic (2001) and Lam (2016). However, some differences exist, especially, over the middle portion of the airfoil where interaction of TEV and separation vortex with the secondary vortices take place.

The shedding characteristics of the flow over an airfoil at high AOA is mainly dependent on the interplay between the two large counter-rotating vortex (Breuer and Jovivic, 2001; Lam, 2016). As a result of the interactions, the strength and size of the two shed vortices at the wake do not remain the same unlike the classical bluff body vortex shedding where symmetric wake is observed and vortices of equal size and strength persist downstream the flow. Hence, airfoil and flat plate at high incidence may produce asymmetric wake containing vortices of unequal strength (Breuer and Jovičić, 2001; Lam, 1996; Freymouth *et al.*, 1984) which has also been observed in our study as evident from the instantaneous streamlines and vorticity shown in figure 5.2.1 where the shedded TEV is the stronger one while the shedded CW vorticity is negligible (for both the cases).





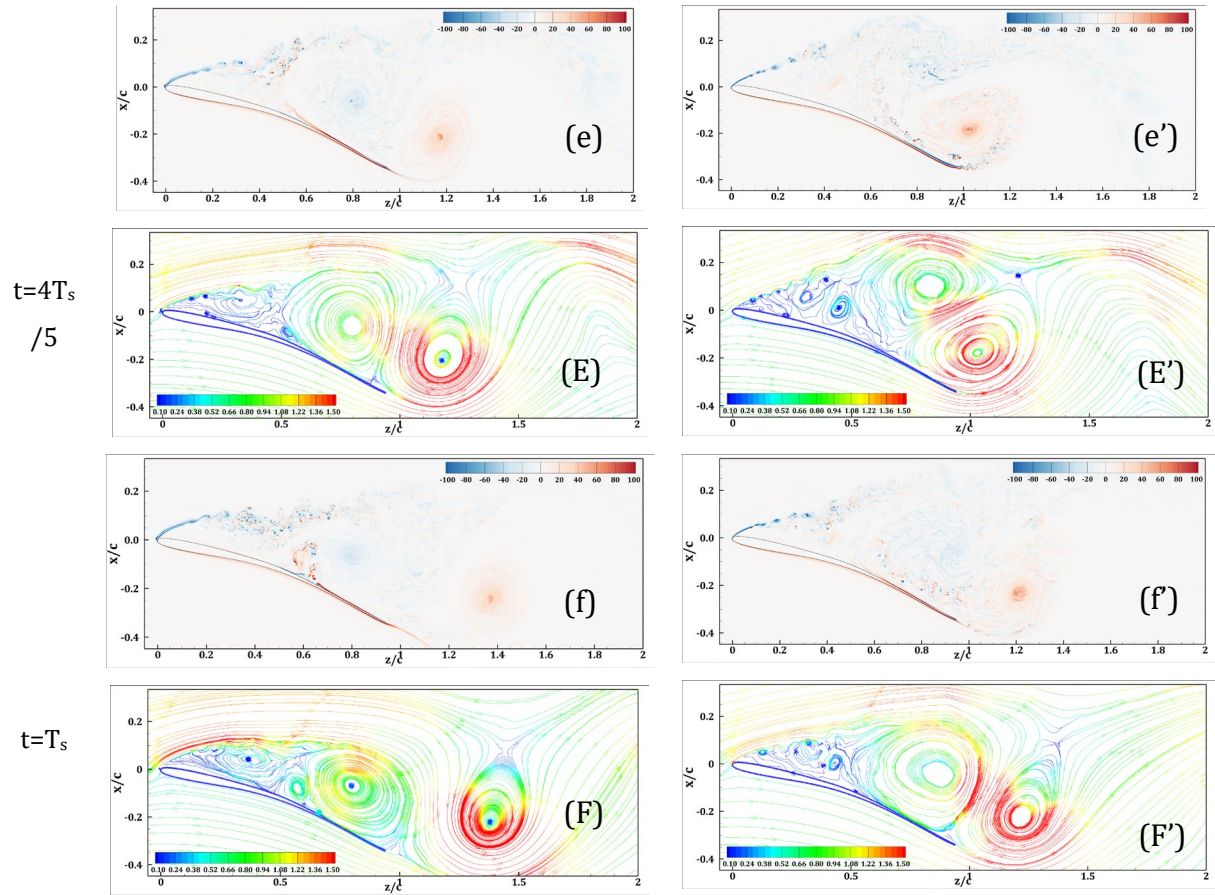


Figure 5.2.1: Evolution of spanwise vorticity, $\omega_y c/U_\infty$ during one shedding period, T_s ; figure a-f illustrates $\omega_y c/U_\infty$ of the serrated wing (left) while a'-f' denotes to ω_y of the smooth case (right). Figure A-F/A'-F' shows instantaneous streamlines colored with velocity magnitudes during each shedding phase shown in the spanwise vorticity contours. Time interval between two consecutive sub-figures is $T_s/5$.

From figure 5.2.1: $t=2T_s/5$, $3T_s/5$ (c', d'), we can observe that near the TE, flow separation occurs for the smooth wing during the TEV expansion period while the serrated case shows attached flow at that region. Both cases illustrate the so-called

“eruption phenomena” when separation vortex is close to the no slip wall (after the shedding of TEV) and subjected to intense viscous action. As a result, wall layer vorticity ejection occurs and secondary vortices form near the wall ($t=0, T_s/5, 2T_s/5$) (Luton *et al.*, 1995; Balci *et al.*, 2015). This process is regenerative and feeds vorticity to the regions upstream. When Reynolds number is more than 5000, this process generates a whole sequence of vortical structures to be ejected from the boundary layer (Kudela and Malecha, 2009). The formation of CCW vortex near the wall ($\sim 0.5 z/c$) is also owing to this phenomenon which causes area reduction of the recirculation zone.

The main differences that can be observed from the instantaneous figures that the eruption phenomena produce secondary vortices at the middle of the wings that appear to be of different sizes (also evident from time-averaged contours in figure 5.1.3) as well as the turbulent boundary layer at TE separates for the smooth case during the TEV enlargement period. The differences point towards wall layer vorticity eruption via (1) separation vortex as the eruption phenomenon depends on its strength while it is near the wall (i.e. pressure gradient at the wall under the vortex) and viscosity (Kudela and Malecha, 2009; Doligalski *et al.*, 1994); TBL separation during TEV enlargement phase (smooth wing) due to (2) complex trailing edge vortex dynamics that generates APG near trailing edge. To determine the intensity of the vortical structures during these phenomena, we analyze the instantaneous flow fields’ vorticity magnitude profiles during the aforementioned phases which are shown at figure 5.2.2.

In figure 5.2.2 ($t=0$, a''), the vorticity magnitude profiles are plotted to compare the local strength of the vorticity over the airfoil surface. The other two rows of sub-figures ($t=2T_s/5$, $3T_s/5$) shows the vorticity magnitude during the TEV expansion phases as shown in figure 5.2.1. From all sub-figures of figure 5.2.2, we can observe that the core region of the separation vortex (SV) appears to be stronger for the serrated wing. Here, we adopt the vortex center definition provided by Strawn *et al.* (1999) which is the local maxima of vorticity magnitude inside a rotational region of the flow. It is also evident from the profiles shown in (figure 5.2.2: a'') where the peak vorticity of the serrated wing's SV is higher in terms of magnitude. Similar trend can be observed regarding the TEV intensity when the smooth case is considered. During the expansion of TEV, smooth case depicts a significantly stronger TEV at the trailing edge as shown in the profiles (figure 5.2.2: b'') and (c''). A stronger SV will promote more vorticity ejection from the wall, as a result, the secondary CCW vortex formation would also be intensified accompanied with a strength reduction of SV while it's near the surface (Luton *et al.*, 1995). On the other hand, a stronger TEV will generate a stronger induced velocity field which, in conjunction with the SV induced velocity field would determine the overall flow pattern. The TEV, being stronger than the SV during the enlargement phase (higher vorticity magnitude at the vortex core), draws in fluids from the wake as well as the bottom surface of the wing, transport it towards the region where secondary vortices are located (figure 5.2.1: $t= T_s/5$, $2T_s/5$, $3T_s/5$). The SV undergoes more pronounced deformation than the TEV during the development of TEV as interaction between two unequal-strength counter-rotating vortices will cause weaker one to deform more than the stronger one due to unequal

induced strain field, however, both vortices will experience deformation due to the mutual induced strain field (Soo *et al.*, 2007). In our case, we see similar phenomenon for both wings where the weaker SV undergoes significant deformation (figure 5.2.1) compared to the stronger TEV during its enlargement phase. Also, smooth wing's trailing edge exhibits flow separation during this TEV enlargement phase which is associated with the stronger TEV strength. The initial formation of TEV before shedding resembles that of a wing tip vortex formation where the bottom boundary layer (pressure side) rolls up over the upper surface (due to pressure difference between upper and lower surface of the wing). A strong tip-crossing flow from the pressure surface to the suction surface ensues flow separation from the suction surface boundary layer at the wingtip, forms secondary and tertiary vortices inside the tip vortex close to the tip (known as tip vortex system). It has been observed that during the early stage of tip vortex formation (over the wingtip of the frontal half of the wing) when the tip crossing flow is not strong enough, favorable APG persists resulting in lack of flow separation in the tip region (Guini and Green, 2013; Duraisamy, 2005). Hence, TEV strength beyond a certain limit might contribute to APG development as vortices by nature will always change the pressure distribution over a solid surface due to viscous-inviscid interactions.

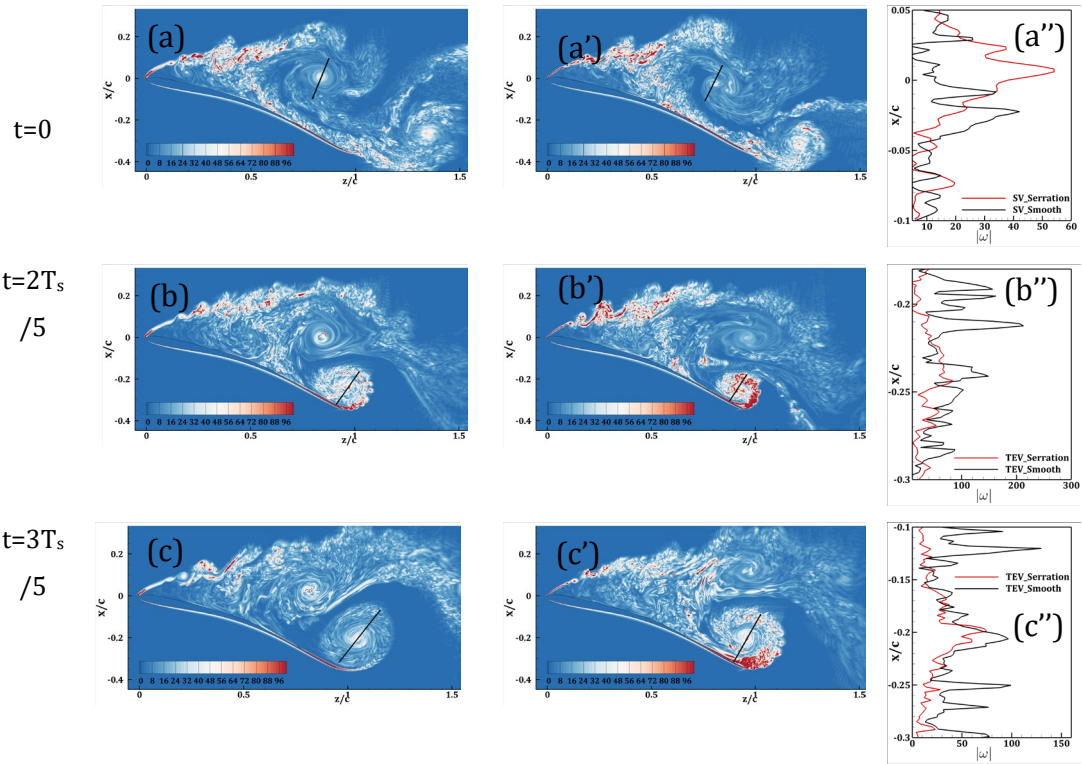
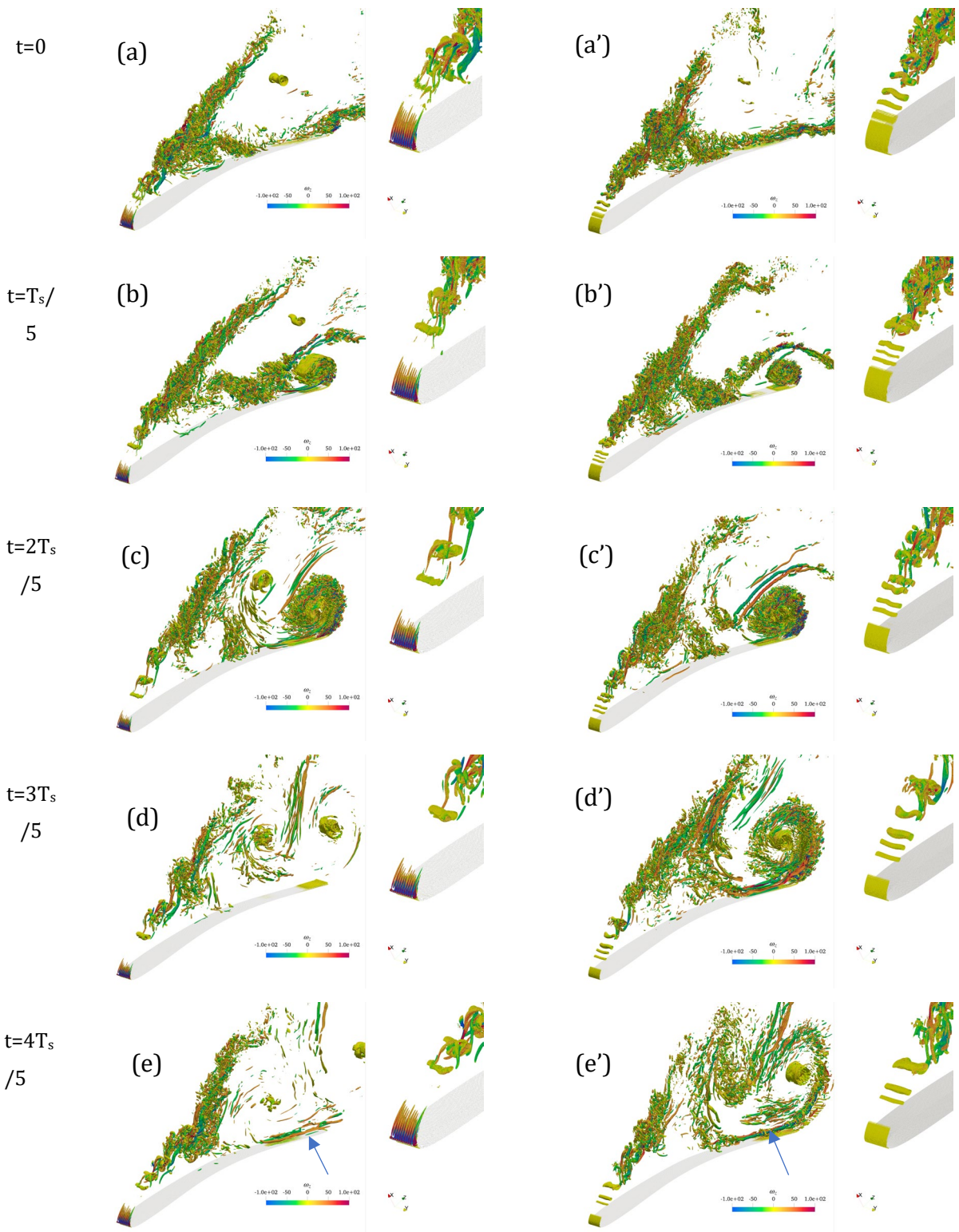


Figure 5.2.2: Vorticity magnitude, $|\omega|$ during $t=0$, $2T_s/5$ and $3T_s/5$ instances shown in figure 5.1.7 (left: serrated wing; right: smooth wing). Black lines illustrate the locations where vorticity magnitude data were extracted from. The lines were placed in such a manner so that they pass through the vortex cores and its boundaries. Figure $a''-c''$ are the line plots of the extracted vorticity magnitude data.

Serrations are located upstream where the leading-edge flow separation initiates. As a result, the shear layer pass through the serrations. As they are angled and placed in a series across the span, their impacts on the three-dimensionality of the flow is significant. To observe the three-dimensional flow patterns around both wings, Q-criterion (second invariant of the velocity gradient tensor) values (Hunts *et al.*, 1988) are estimated to identify rotation dominated regions in the flow. In figure 5.2.3, iso-

surface of Q-criterion is presented during a shedding cycle as shown in figure 5.2.1. The iso-surfaces are colored with streamwise vorticity ($\omega_z c/U_\infty$). Both wings show dominant flow features: shear layer generated from the flow separation at the leading-edge rolls up into quasi two-dimensional Kelvin–Helmholtz vortices (Yarusvesch *et al.*, 2008; Visbal, 2011; Klose *et al.*, 2021) also known as KH rollers. In addition to the presence of large-scale structures such TEV and SV, we can also observe abundance of rib vortices in between the rollers. In the boundary layer near the trailing edge, longitudinal vortex pair ($t=4T_s/5$) can also be observed for both cases which are known for their turbulent boundary layer thickening (when their common flow is away from the surface) and thinning (when their common flow is towards the surface) effects (Pauley and Eaton, 1988). These longitudinal vortices can occur naturally in TBL flows (can also be generated artificially) and significantly alter the dynamics of the boundary layer. Boundary layer thinning is associated with boundary layer separation prevention (via interaction of the vortices pair) but at the expense of enhanced skin friction drag (Pauley and Eaton, 1988), on the other hand, promoting BL thickening leads to flow separation. However, their effects are entirely dependent on how close/strong the vortices pairs are. As shown earlier in figure 5.2.1 ($t= T_s/5, 2T_s/5, 3T_s/5$), serrated wing exhibits attached flow during the TEV enlargement phase. This can also be observed in the Q contours. TE surface of the serrated wing contains vortices pairs of “common flow up” (clockwise at the edge then anti-clockwise at the middle) whereas the smooth wing contains vortices pairs of “common flow down” which signifies TE BL thickening of the smooth wing (can also be observed in figure 5.2.1 ($t=2T_s/5, 3T_s/5$)).

Typically, KH instability is the primary instability mechanism for flows involving laminar-turbulent transition with a separation bubble in the scope (Yang and Voke, 2001). Secondary instabilities may also be present in the vortex sheet (shear layer) which may coexist and coupled with the KH mechanism. Two such secondary instabilities have been reported often in literatures: one of them is two-dimensional subharmonic vortex pairing instability which involves pairing/merging of two KH rollers into one whereas the other one is a three-dimensional instability associated with rib vortices formation which undergo stretching in the streamwise direction and bend the core of the KH rollers (Metcalf *et al.*, 1987; Yang, 2013; Zauner *et al.*, 2019). In figure 5.2.4, frequency spectra of the streamwise and spanwise velocity fluctuations are shown for the temporal data of 20 shedding cycles which were collected from the locations inside the shear layer (figure 5.2.4(a)). The fundamental frequency (Table 5.1.1) along with its harmonics can be observed at all probe locations in figure 5.2.4 (b) for both cases. A noticeable difference between serration and smooth case can be observed in Figure 5.2.4 (c), where probe 1, 2 and 3 showing no distinguishable frequency peaks for smooth wing at this frequency range. This indicates that three dimensional perturbations emerge earlier when serration facing the freestream. As a result, early formation of rib vortices ensues (figure 5.2.3) (compared to the smooth case), which deforms the two-dimensional roller vortices. The shear layer eventually undergoes expansion through pairing/merging process of two neighboring quasi two-dimensional rollup vortices as evident by the subharmonic of the fundamental frequency which is found to be present in both spectra.



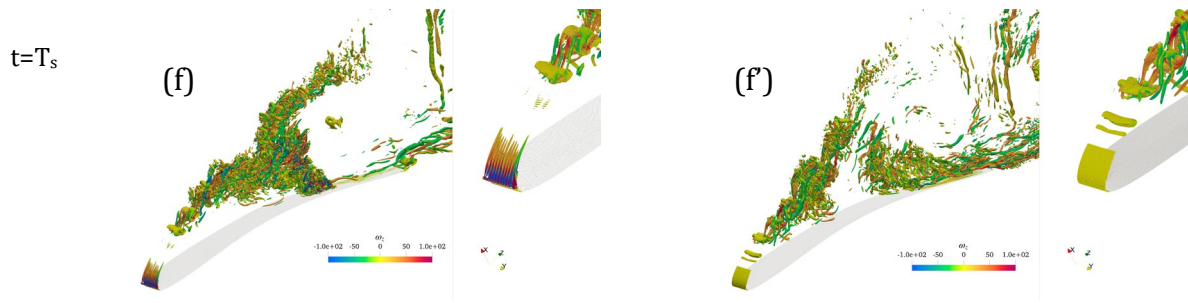
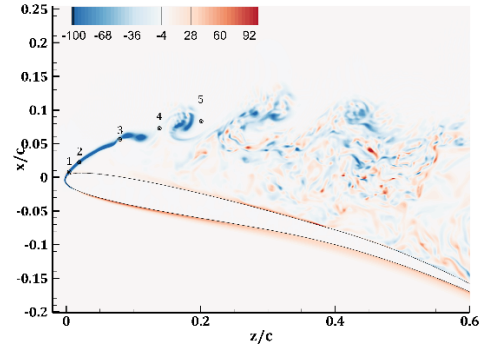
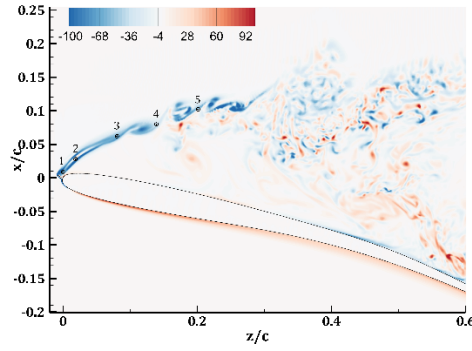


Figure 5.2.3: Instantaneous iso-surface of Q -criterion ($Q=1000$) colored with streamwise vorticity ($\omega_z c / U_\infty$), during the instances shown in figure 5.1.7.

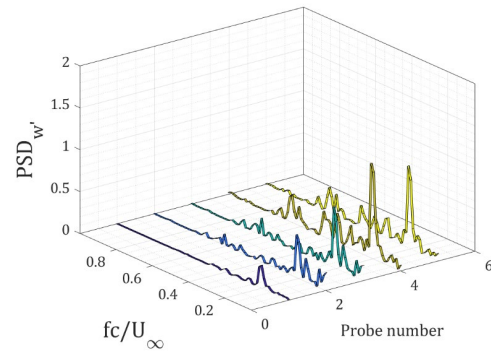
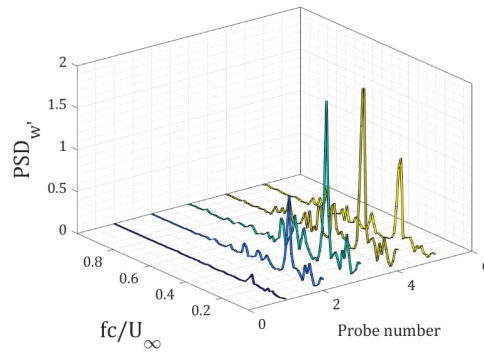
In figure 5.2.3, a notable difference exists between the two cases in terms of streamwise vorticity generation at the leading-edge shear layer. Serrated wing shows finite values whereas the smooth case depicts null values close to where the leading-edge separation occurs. The origin of this streamwise vorticity generation can be traced back to streamwise gradient of the spanwise velocity (Bradshaw, 1987) which is shown in figure 5.2.5. The profiles are for time and span averaged quantity which were extracted from the locations close to the leading-edge shown in figure 5.2.5(a). From the mean vorticity equations, Bradshaw (1987) showed that “skewing” of spanwise vortex lines arises from streamwise gradient of the spanwise velocity which means three dimensionalities in the flow is originated from the flow deflection. Indeed, when the shear layer pass through the serrations, it deflects the flow towards the direction of the serration tip (see figure 5.2.6). Note that, negative gradients in figure 5.2.5 (1,2,3) refers to the location where foremost portion of the separation bubble is while the positive gradients are the location of the LE shear layer.

It can be observed from all subfigures of figure 5.2.3 and figure 5.2.1 that SV never shed completely from the upper surface of the wing rather it splits and parts of its vorticity is shed into the wake (also, see the animation showing iso-surfaces of Q-criterion during a shedding cycle in Appendix A). SV is sustained by the instability mechanisms at the LE. Due to the subharmonic instability, two KH vortices will have different convective velocity (one will shift upward closer to the higher velocity side of the shear layer) which will eventually merge into a stronger one. During this merging process, abundance of small-scale turbulence is observed (McAuliffe and Yaras, 2009). Guha and Rahmani (2019) showed that turbulence intensity due to merging is dependent on the initial asymmetry of the KH billow shape (high initial asymmetry generates high turbulence during the merging). From the contour plot of the average TKE we can see, serrated wing shows high TKE (figure 5.3.1: a, a') in the downstream of the LE shear layer. Also, from visual inspection of the spanwise vorticity plots (figure 5.2.1), we can observe that the LE shear layer is of wavy shape starting from the location of separation. Hence, we can surmise that serrations may intensify the vortex merging process, leading to enhanced momentum transport.

Probe locations
(a)



Streamwise velocity fluctuation spectra
(b)



Spanwise velocity fluctuation spectra
(c)

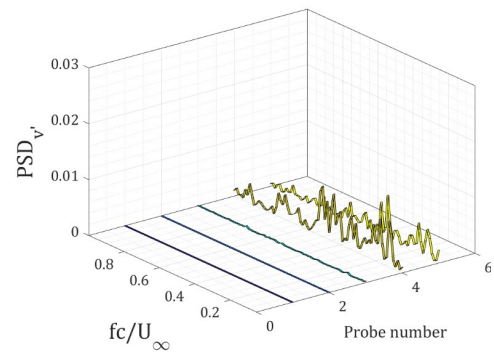
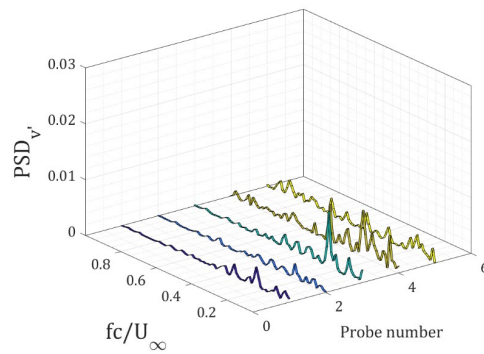


Figure 5.2.4: Frequency spectra of the velocity fluctuations at the leading edge inside the separated shear layer; left: serrated wing, right: smooth wing. Probe locations are shown in row (a), frequency spectra of streamwise velocity fluctuations in row (b) and spanwise velocity fluctuations in row (c). PSD abbreviates to power spectral density.

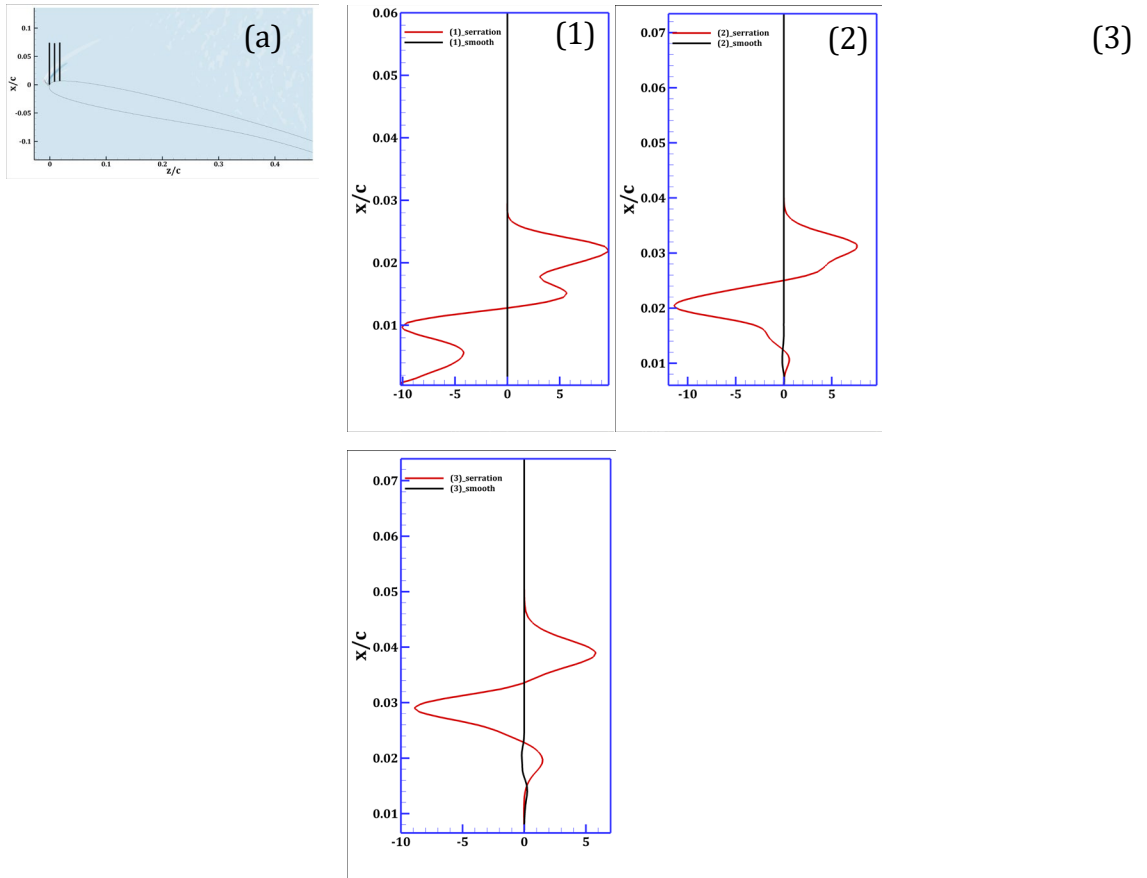


Figure 5.2.5: Time and spanwise averaged streamwise gradient of spanwise velocity profiles (dv/dz); taken at three locations shown in (a) where location (1) is the leftmost and location (3) is the rightmost.

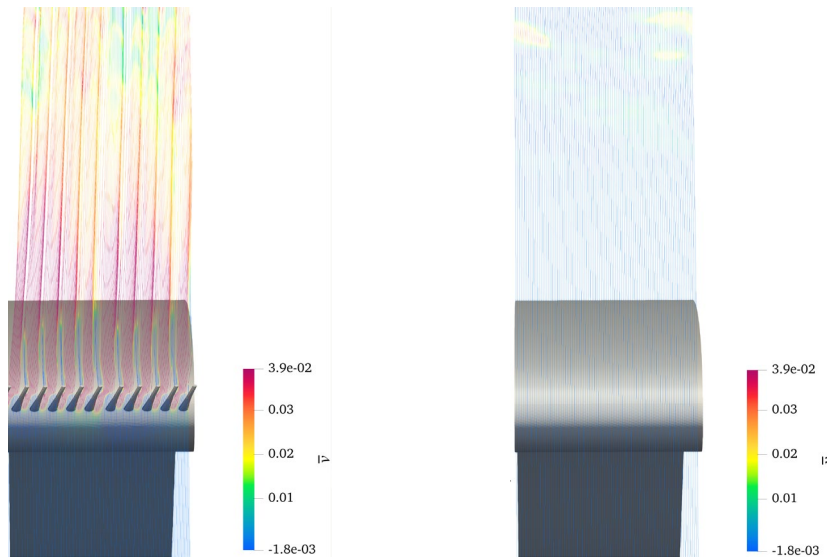


Figure 5.2.6: 3D streamlines showing flow deflection effect by serrations. Streamlines colored with time averaged spanwise velocity.

5.3 Influence of serrations on turbulence: statistical analysis

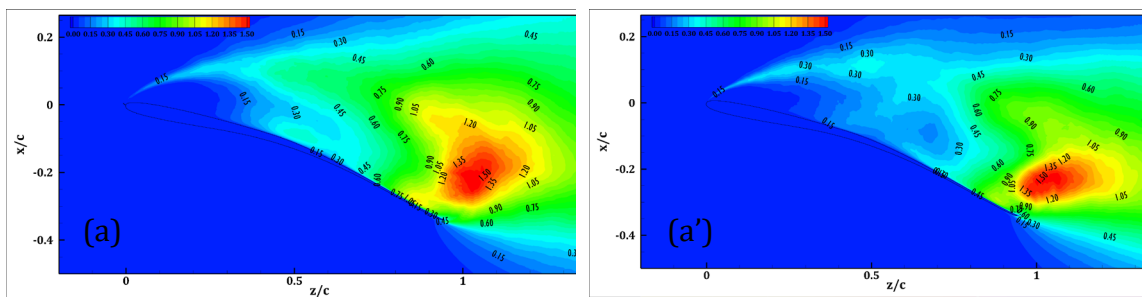
From the previous discussions, we showed serration induced effects on the flow patterns. In this section, turbulent flow features around the wings is characterized. In figure 5.3.1 TKE (turbulent kinetic energy) and RMS (root mean square) of streamwise and spanwise velocity fluctuations are presented. As mentioned earlier, in our study, transition does not occur in a location over the separation bubble rather the flow is turbulent starting from the onset of separation. From the comparison between figure 5.3.1: (a) and (a'), we can observe that TKE contour level is relatively higher in the frontal half of the serrated wing, especially, at the mean location of the secondary vortices (see figure 5.1.3) over the upper surface ($0.3-0.5 z/c$) and its surroundings. This signifies stronger mixing between the high momentum fluid above the shear layer and low momentum fluid inside the bubble region. Both wings

exhibit low TKE near the leading edge starting from $0 z/c$ to approximately $0.2 z/c$. The fluid inside this region is relatively still (but not completely stagnant, see figure 5.1.3), resembles that of a “dead air zone” inside an LSB; however, KH vortices and their interactions transport momentum in this region which can be observed in figure 5.2.1 instantaneous streamlines. Interestingly, serrated wing depicts a larger zone of high TKE above the trailing edge compared to the smooth wing. This zone is where TEV and SV interacts before the TEV being shedded into the wake; a larger zone of high TKE signifies SV and TKE (counter rotating vortex pairs) interactions promote a higher turbulent transport of momentum from the surrounding fluid. As a result, intensity of the reverse flow is reduced for the serrated wing.

From figure 5.3.2 (a), it can be observed that TKE is higher in profile a3, a4, a5 for serration as can be seen in the contour plots in 5.3.1 (a); however, near the LE shear layer (profile a1) peak value of TKE is higher for the smooth case whereas in profile a2 both of the profiles are very similar in terms of peak values. Although serrations exhibit a turbulence reduction feature in profile a1, it is actually impacting the shear layer to develop 3D turbulence instead (see figure 5.3.3 a1). The streamwise, cross-stream and spanwise velocity fluctuations profiles shown in figure 5.3.3 demonstrates that the peak RMS values of streamwise and cross-stream fluctuations are reduced but spanwise fluctuation are non-zero unlike the smooth wing’s shear layer. When the shear layer pass through the serrations at its early stage of development, serration impacts the flow in such a way that the extraction of turbulent energy from the mean flow is biased towards developing spanwise disturbances. The small bump seen in smooth wing’s spanwise velocity fluctuations profile in figure

5.3.3 (a1) is actually the foremost edge of the separation bubble. As the flow heads downstream (figure 5.3.3 (a3-a5)), all fluctuating components develop in both shear layers; however, serrated wing shows higher magnitudes of RMS fluctuations of streamwise and vertical velocities consistently. Regarding the spanwise fluctuations, the differences even out at the downstream zones of the contour (figure 5.3.3 (a3-a5)).

Also, serrated wing's shear layer is lifted up from the upper surface of the wing compared to the smooth case. This can be observed from TKE profiles as well as the RMS fluctuation profiles at a1 location. This type of upward deflection of shear layer results in wake enlargement which can be observed from figure 5.3.2 (b1-b4) profiles. Similar phenomenon has been observed in the study conducted by Al-Battal *et al.* (2016) where they conducted PIV experiments using NACA 0012 airfoil to investigate the effects of blowing on airfoil performance. They also observed a larger wake resulting from the upward deflection of the shear layer. From the wake profiles shown in figure 5.3.2 (b1-b4), we can also observe that serrations do not have a strong effect on the intensification of wake turbulence except larger wake is mainly developed at the near wake less than 7 chord length away from the wing.



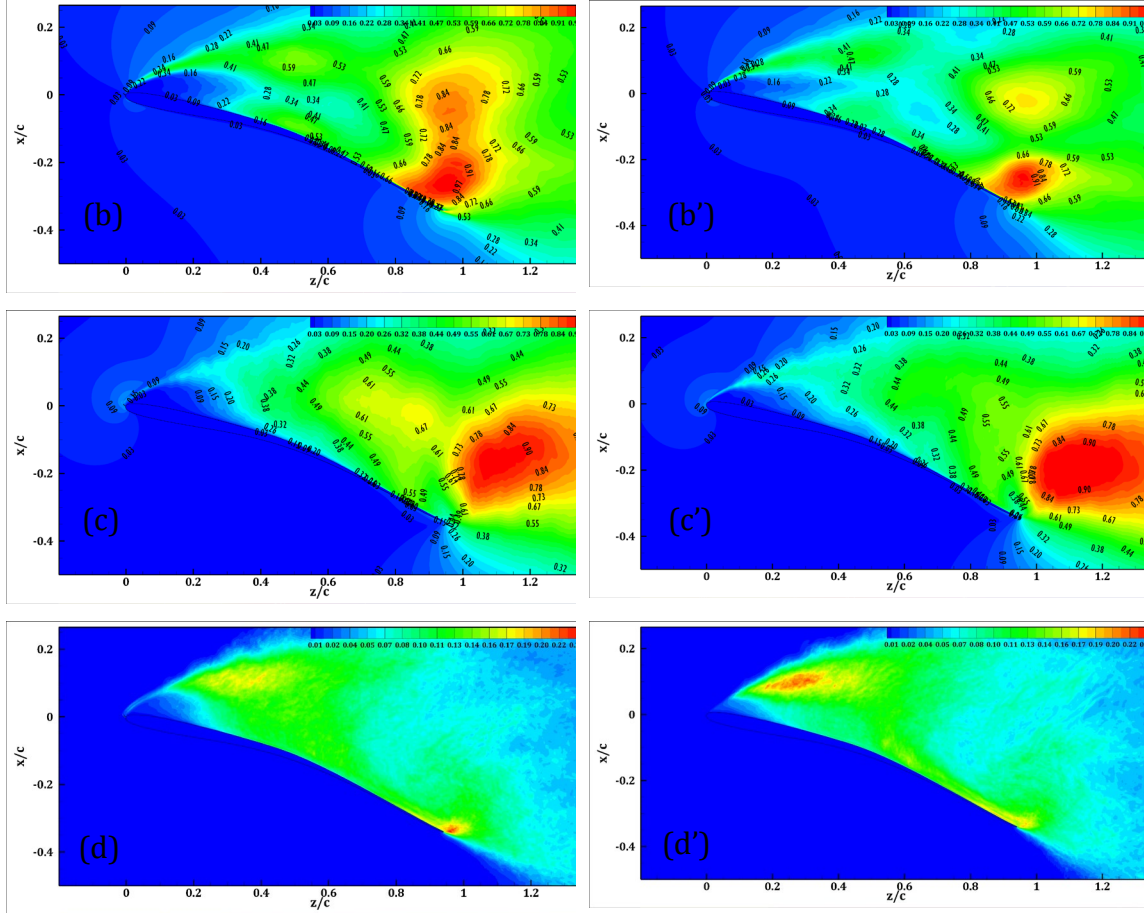


Figure 5.3.1: (a) Time and spanwise averaged turbulent kinetic energy (TKE) of serrated case, (a') smooth case; RMS of streamwise velocity fluctuations for (b) serrated wing, (b') smooth wing; RMS of vertical velocity fluctuations for (c) serrated wing (c') smooth wing; RMS of spanwise velocity fluctuations for (d) serrated wing (d') smooth wing. Note that, TKE and RMS values are normalized by U_∞^2 and U_∞ respectively.

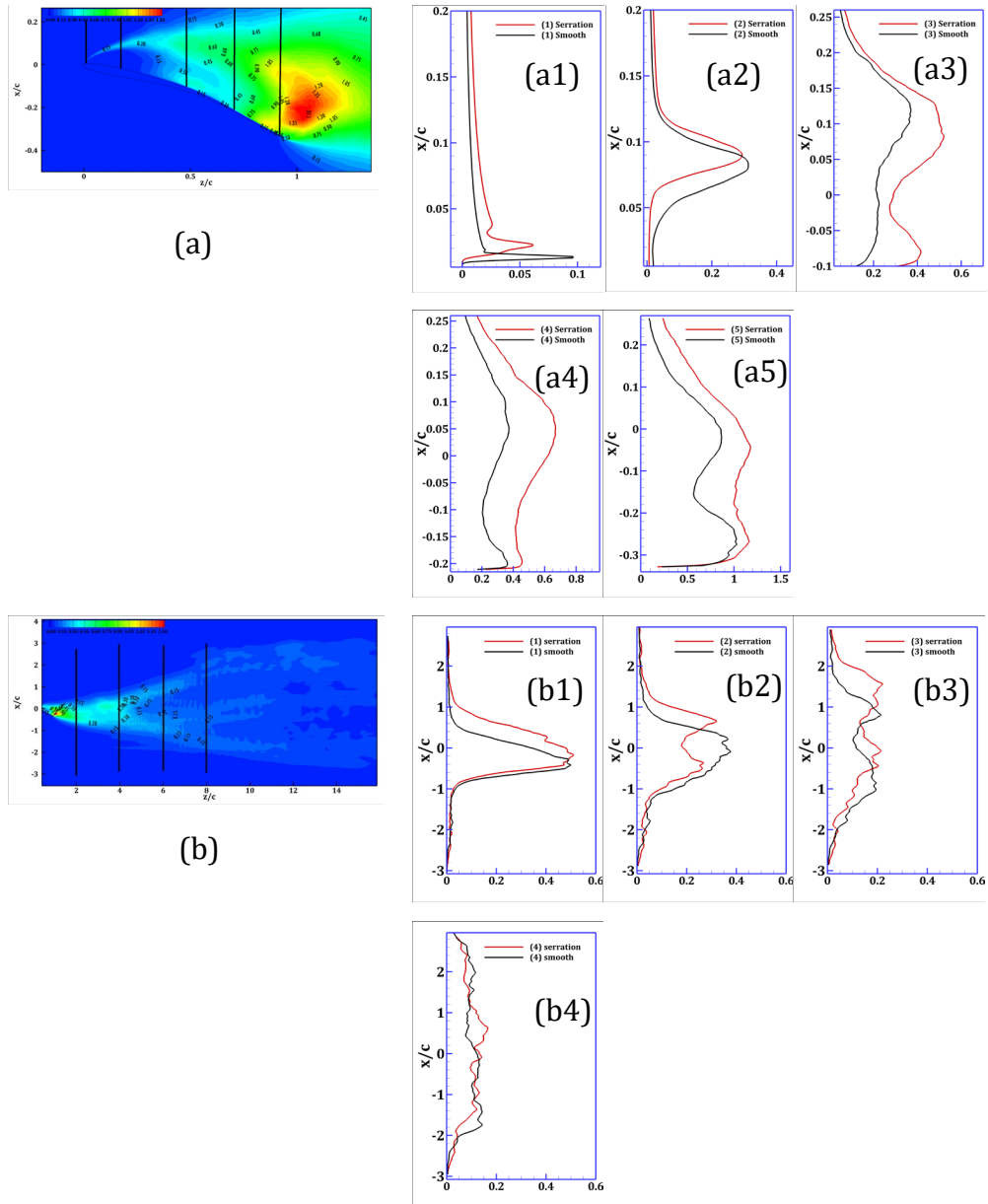
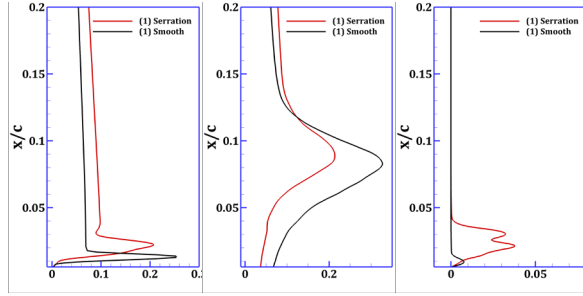
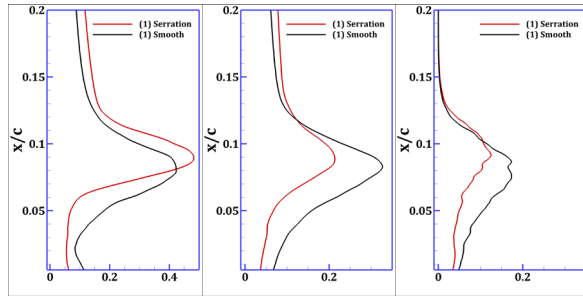


Figure 5.3.2: Comparisons of TKE profiles. Data taken at the locations shown with black lines over the contour plot; (a) profiles over the wing (b) at the wake. Location numbering (i.e., a1, a2..., a5) starts from the leftmost line in the contour maps in (a) and (b).

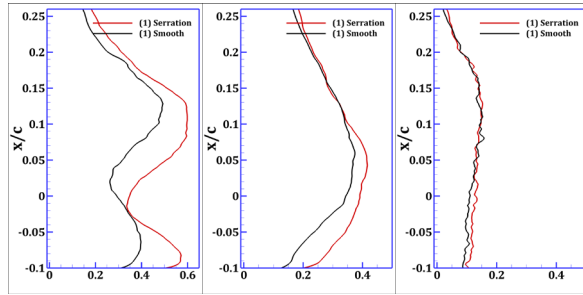
(a1)



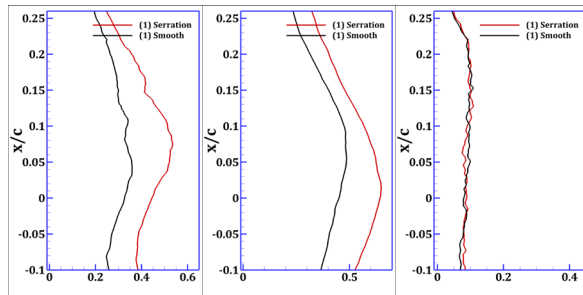
(a2)



(a3)



(a4)



(a5)

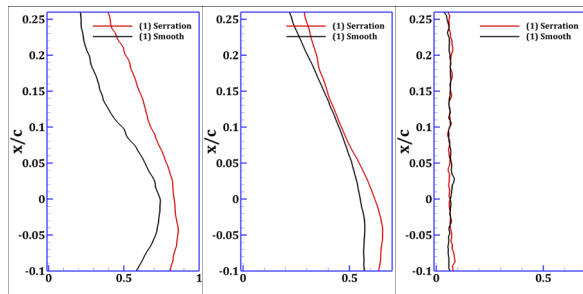


Figure 5.3.3: From left: RMS of streamwise velocity fluctuations, RMS of cross-stream velocity fluctuations, RMS of spanwise velocity fluctuations at location (a1, a2, a3, a4, a5) as shown in figure 15(a).

Turbulent motions in the flow can generate additional momentum fluxes and they can be interpreted as additional effective stresses known as Reynolds stresses which comprises of normal stresses (diagonal terms of the Reynolds stress tensor) and shear stresses (off diagonal). In this section, Reynolds shear stress in the streamwise-vertical plane ($\langle \overline{u'w'} \rangle / U_\infty^2$) is described, the contour plot is shown in figure 5.3.4 (top). The Reynolds shear stress is also used to indicate mean transition location in fluid flows where Reynolds stress reaches to $0.001U_\infty^2$ after the separation of the boundary layer (Ol *et al.*, 2005; Hain *et al.*, 2009). From the profile shown in figure 5.3.5 (a1), Reynolds stress is already much higher at the shear layer close to the leading-edge for both cases. As the shear layer heads downstream the flow, the sign of the Reynolds stress changes at $0.15 z/c$ for the smooth wing and $0.2 z/c$ for the serrated case (figure 5.3.4: (a), (a')). This can also be observed from figure 5.3.5 (a2) that shear layer changes sign at a later location for the serration. To analyze the turbulent momentum transport in the flow, a similar approach to the quadrant analysis introduced by Wallace *et al.* (1972) can be employed. The time and span-averaged Reynolds stress $\langle \overline{u'w'} \rangle / U_\infty^2$ is produced by four types of instantaneous events: Q2 (+w, -u) and Q4 (-w, +u) are associated with vertical turbulent momentum transport; Q2 is downward transport of high-speed fluid, Q4 is upward transport of low speed fluid. On the other hand, Q1 is upward transport of high-speed fluid and Q3

is downward transport of low speed fluid (Wallace, 2016; Soldati and Banerjee, 1998). Hence, negative $\langle \overline{u'w'} \rangle$ creates gradient momentum flux while positive $\langle \overline{u'w'} \rangle$ creates counter gradient flux (Wallace, 2016; Metcalfe *et al.*, 1987).

Near the leading-edge, the serrated wing shows the smaller region of $\langle \overline{u'w'} \rangle \sim 0$, this can also be observed in the TKE contour plots. At the TE, serrated wing shows a large region of negative $\langle \overline{u'w'} \rangle$ (Q2 and Q4 type event dominant) compared to the smooth wing. This implies vertical turbulent momentum transport in that region is quite significant. This zone is where TE and LEV interacts mostly during the shedding cycle, bringing high speed fluid from the surroundings. In time-averaged sense, serrated wing induces high vertical turbulent momentum transport near the TE. At the middle portion of the wing, a large region of positive $\langle \overline{u'w'} \rangle$ (Q1 and Q3 type event dominant) can be observed for the smooth wing. This location corresponds to the mean LEV core location in time-averaged streamlines; positive Reynolds stress (Q1 and Q3 type event dominant) corresponds to contribution to negative turbulence production (i.e., TKE sink, energy from fluctuating component is transferred to the mean flow (Metcalfe *et al.*, 1987; Soldati and Banerjee, 1998)). As a result, turbulent momentum transport in smooth wing is limited compared to the serrated wing. We also show the Reynolds stress in the crossflow plane ($\langle \overline{u'v'} \rangle / U_\infty^2$) in figure 5.3.4: b, b'. Significant differences in the pattern of the contours are not observed except near the leading edge which implies that the spanwise fluctuations at the leading edge does not significantly alter turbulent stress pattern in the crossflow plane. It is important to note that all the turbulent characteristics as well as the profiles shown in this subsection 5.3 are time and span averaged over ~ 5 vortex shedding cycles which may

also have a smearing effect as a result of averaging. This may have an impact on the values across LE shear layer which might be a reason behind low TKE and low Reynolds stress near the LE for the serrated wing (compared to the smooth one) as the subsequent profiles showed higher values for the serrated case.

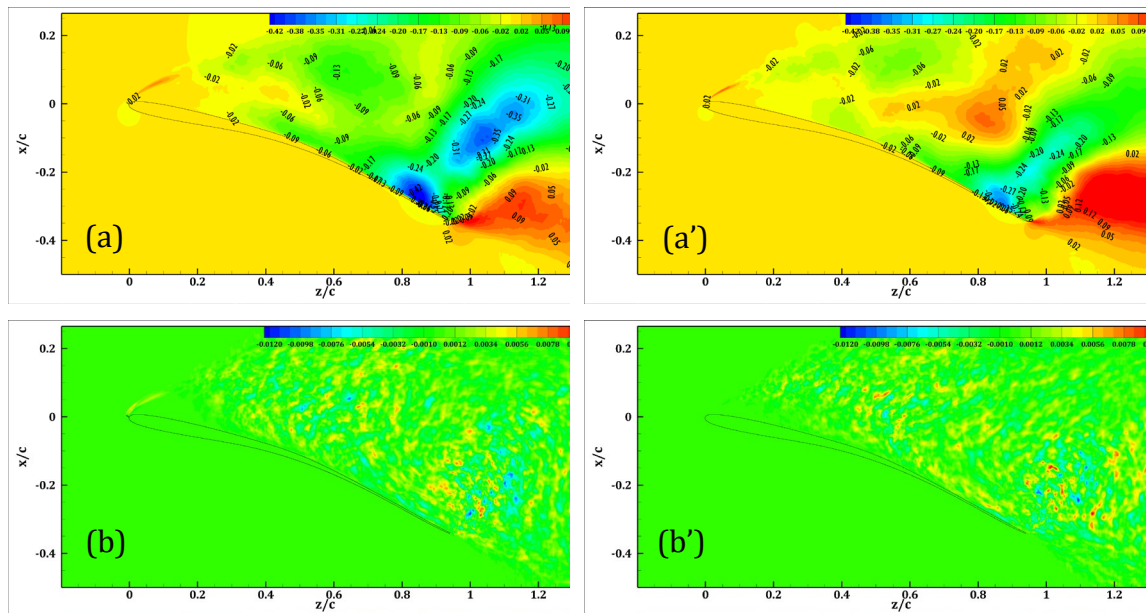


Figure 5.3.4: Time and spanwise averaged Reynolds stress $\langle \overline{u'w'} \rangle / U_\infty^2$ of (a) serrated wing (a') smooth wing; $\langle \overline{u'v'} \rangle / U_\infty^2$ of (b) serrated wing (b') smooth wing

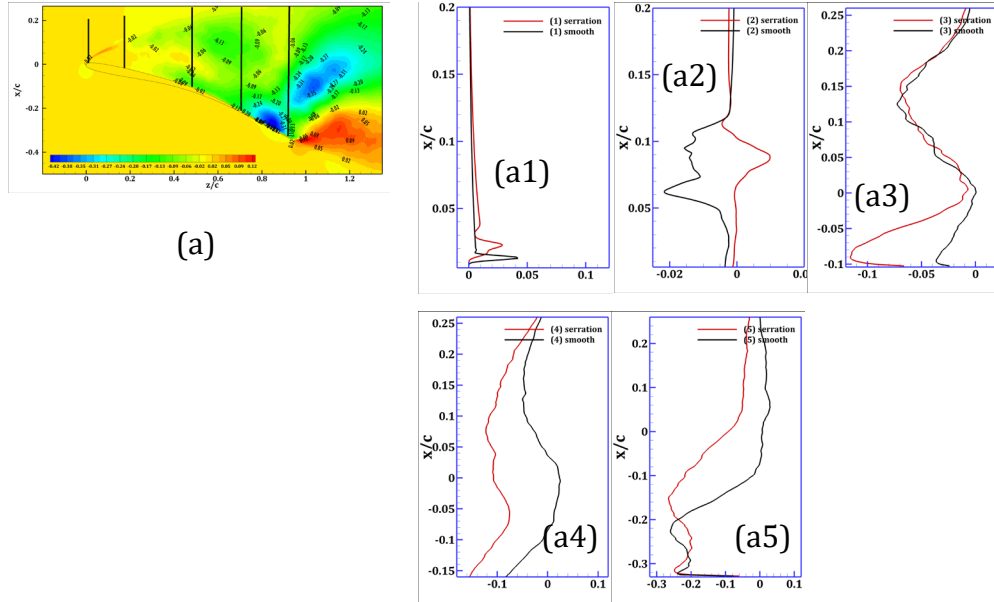


Figure 5.3.5: Reynolds stress ($\langle \overline{u'w'} \rangle / U_\infty^2$) profile comparison. Data taken at the locations shown with black lines over the contour plot. Location numbering (i.e., a1, a2..., a5) starts from the leftmost line in the contour map (a).

5.4 Influence of serrations on instantaneous turbulence

Instantaneous effects on turbulence due to the presence of serrations are assessed in this section. To analyze the instantaneous turbulent flow field, we calculate local fluctuating helicity density ($\vec{u}' \cdot \vec{\omega}'$) during the shedding cycle previously shown in figure 5.2.1. The term “helicity” refers to the mathematical quantity, $\mathcal{H} = \int \vec{u} \cdot \vec{\omega} dV$ which is a quadratic invariant of the Euler equations (Moffatt, 1969). Also, the term “helicity density” in many literatures refers to the local values of $\vec{u} \cdot \vec{\omega}$, which is associated with linkages of vortex tubes (a tubular fluid volume which can move with the flow while the vorticity vector remains tangent to its surface) in the flow (Moffatt and Tsinoabar, 1992). This parameter ($\vec{u} \cdot \vec{\omega}$) had been utilized in many literatures to

identify and characterize vortex cores, separation/reattachment lines, secondary vortices, etc. (see Moffat and Tsinobar (1992) for a brief review). The study by Andre and Lesieur (1977) demonstrated that the presence of large helicity in the flow results in reduction of energy transfer from the large scales to small scales which was also in agreement with the theoretical analysis by Kraichnan (1973). In several studies, it was reported that local helicity density fluctuations $(\vec{u}' \cdot \vec{\omega}')$ is related to small scale intermittency and the dynamics of the coherent structures in the flow (Levich and Tsinobar, 1983; Levich and Tsinobar, 1984; Pelz *et al.*, 1985). Local helicity density $(\vec{u} \cdot \vec{\omega})$ being not Galilean invariant, local helicity density fluctuation is a better choice to understand the instantaneous turbulent field (Orlandi, 1997). The mathematical relation $|\vec{u}' \cdot \vec{\omega}'|^2 + |\vec{u}' \times \vec{\omega}'|^2 = |\vec{u}'|^2 |\vec{\omega}'|^2$ indicates local helicity density fluctuations inhibit energy cascade as the Lamb vector term $|\vec{u}' \times \vec{\omega}'|$ denotes to energy transfer rate in the cascade process (Orlandi, 1997). Also, local helicity density fluctuations (local alignment/counter alignment between vorticity and velocity fluctuations) can distinguish the regions of the flow field where turbulent kinetic energy budget terms may depict significant differences when two cases are compared (i.e., high/low dissipation/production rate).

Figure 5.4.1 shows instantaneous snapshots of the local helicity density fluctuations $(\vec{u}' \cdot \vec{\omega}')$ during the shedding period shown in figure 5.2.1. A closer look to the LE region of both the wings reveals that serrated case has a finite value of $\vec{u}' \cdot \vec{\omega}'$ near the serrations during the entire shedding cycle while the smooth wing doesn't, which implies that either \vec{u}' and $\vec{\omega}'$ are zero or they are orthogonal to each other. Histograms

of the velocity component fluctuations in this zone are shown in figure 5.4.2. From the distribution, it can be observed that both wings have finite streamwise and cross-stream fluctuating velocity components although their spread differ significantly. As vorticity fluctuations inside a turbulent shear layer will also have non-zero values, this implies that serrations generate helicity density via aligning the vorticity and velocity fluctuations (i.e., $\frac{\overline{u'} \cdot \overline{\omega'}}{\sqrt{|\overline{u'}|^2 |\overline{\omega'}|^2}}$). This may result in increased turbulence production and/or decreased dissipation (Orlandi, 1997) compared to the smooth case which we will be investigating in the next section. Also, in figure 5.4.3, histograms of velocity fluctuations are shown in a different x-z plane (i.e., located in between two neighboring serrations). Comparing the histograms of velocity fluctuations in two different planes (figure 5.4.2 and 5.4.3), we can observe that serrations strongly influence spanwise variation of turbulent fluctuations in the LE region while the smooth wing does not impact it significantly. In figure 5.2.4c (spanwise velocity fluctuations spectra), it was observed that probe 1 of the smooth wing did not have any distinguished frequency peak while the serrated wing demonstrated fundamental frequency along with its harmonics in this location. These findings support the previous observations (RMS of velocity fluctuations; see figure 5.3.3) that the serrations prompt three-dimensional turbulence in the shear layer earlier than the smooth wing which impact the subsequent development of rib vortices as well as the separation vortex.

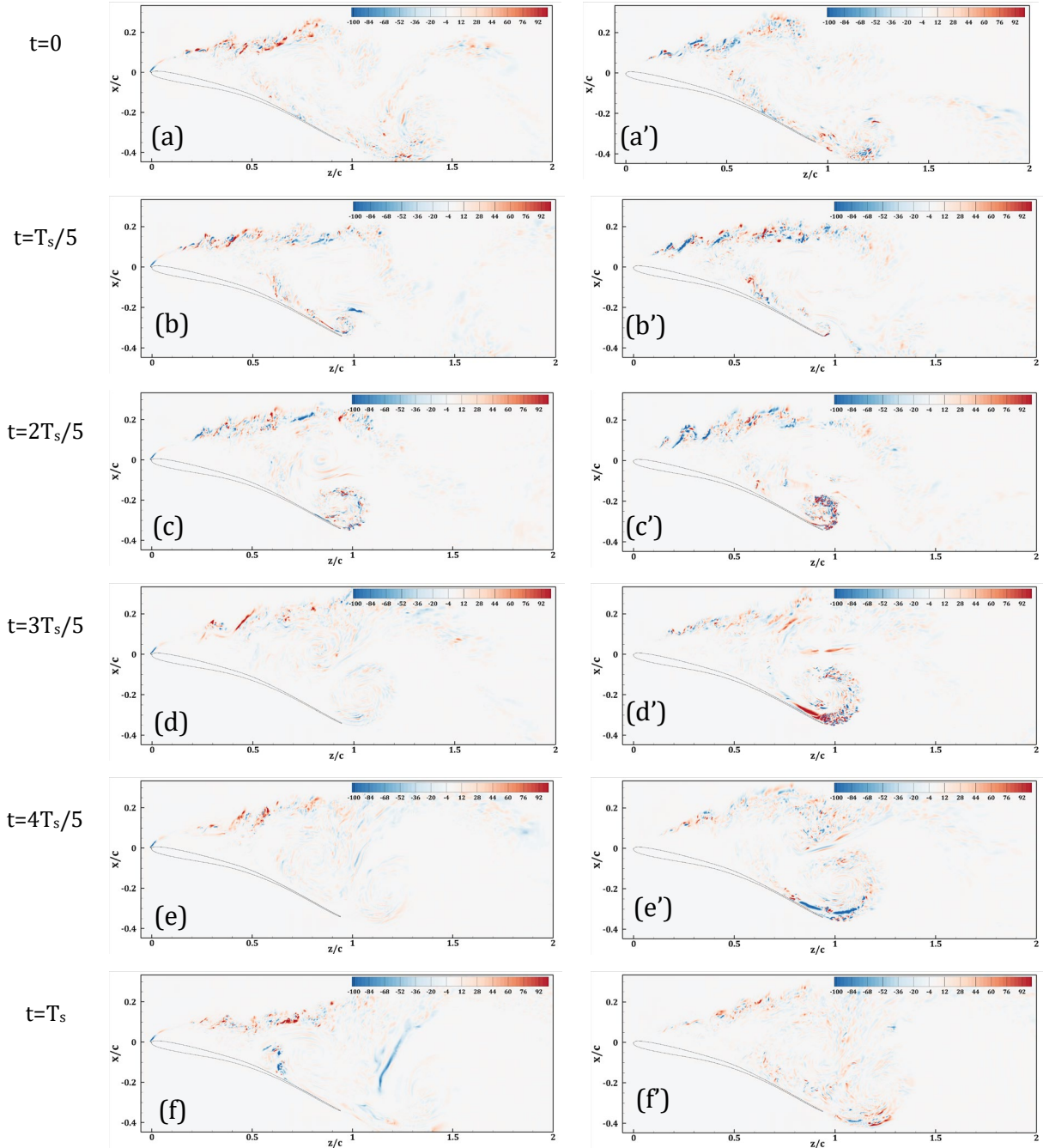


Figure 5.4.1: Evolution of local helicity density fluctuations $(\vec{u}^t \cdot \vec{\omega}^t) / cU_\infty^2$ during one shedding period, T_s . The subfigures on the left (a-f) depict the helicity density field of the serrated wing while the ones on the right exhibit smooth wing's helicity density field. Note that, the figures correspond to the instantaneous snapshots shown in figure

5.2.1.

In figure 5.4.1, both the wings show high magnitude of helicity density at the shear layer downstream the leading-edge where roller as well as rib vortices form and interact (see section 5.2 for descriptions). As three-dimensional turbulent structures are predominant in this zone for both cases during the entire shedding cycle (see also figure 5.2.3), the magnitudes of helicity density fluctuations are naturally inclined towards having larger values (Levich and Tsinober, 1983). During the TEV expansion phases (figure 5.4.1; $t=2T_s/5$, $t=3T_s/5$) and its subsequent departure from the trailing-edge ($t=4T_s/5$), a noticeable difference can be observed between the two cases. The smooth wing exhibits much higher helicity density fluctuations at the trailing edge region compared to the serrated wing. A closer look to the aforementioned sub-figures reveal that the high magnitudes of helicity density appear in the region close to where the flow separates during the development of the TEV. Orlandi (1977) showed that when a pipe rotates, helicity density fluctuations significantly increased in the near the wall region compared to a stationary case. He demonstrated that this increase was associated with drag reduction (at the near wall region) while helicity increase in the central region of the pipe (far from the wall) denotes to increased turbulent energy due to the reduction in turbulent energy transfer. Note that, boundary layer thickening reduces turbulent skin friction drag (Bannier *et al.*, 2016). In this study, boundary layer thickening can also be observed for the smooth LE case (see section 5.2) during the TEV expansion phases. This occurrence may also contribute to overall less drag generation of the smooth LE wing (section 5.1).

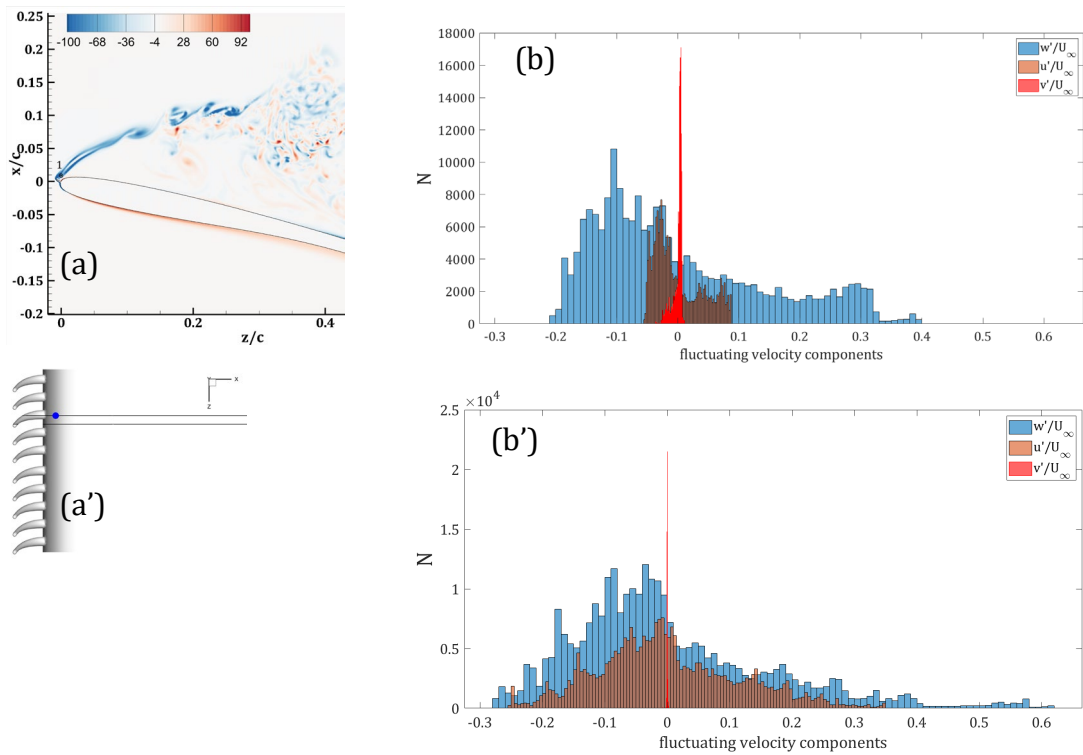


Figure 5.4.2: Histograms of velocity fluctuations inside the shear layer near the leading-edge (point 1 in sub-figure (a)) of both the wing. Note that, point 1 in sub-figure (a) shows the probe location in the x - z plane while sub-figure (a') shows the x - z plane location (blue circle) on the wing in 3D (i.e., plane intersecting the middle of a serration). Sub-figure (b) depicts the histogram of the serrated wing while (b') shows the histogram of the smooth wing. Here, N represents the number of occurrences during ~ 20 shedding cycles.

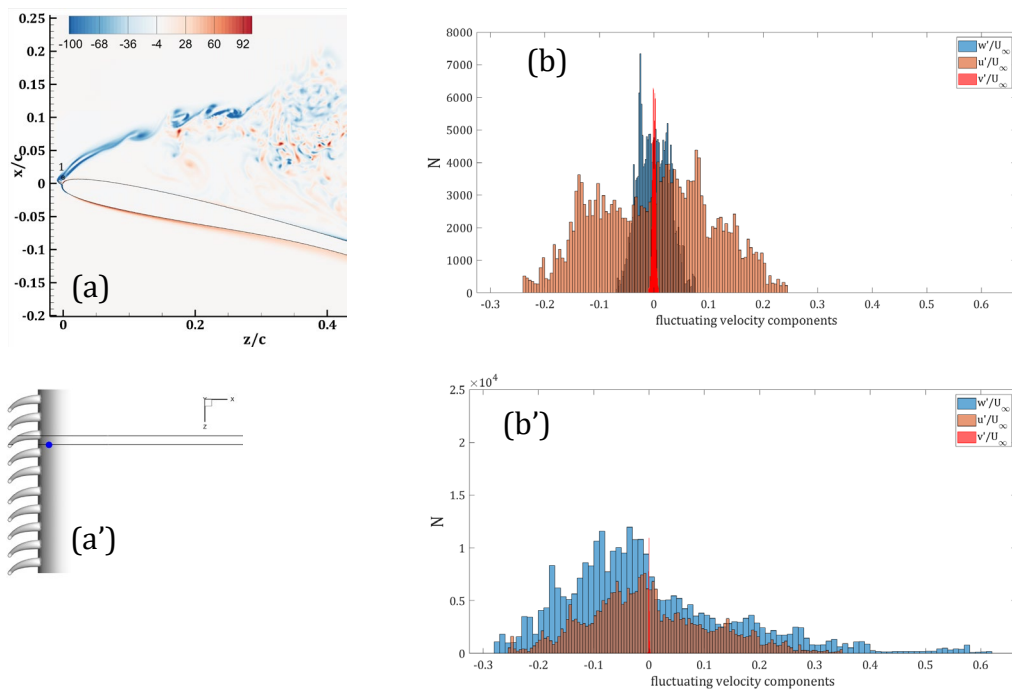


Figure 5.4.3: Histograms of velocity fluctuations inside the shear layer near the leading-edge (point 1 in sub-figure (a)) of both the wing. Note that, point 1 in sub-figure (a) shows the probe location in the x - z plane while sub-figure (a') shows the x - z plane location (blue circle) on the wing in 3D (i.e., between two neighboring serrations). Sub-figure (b) depicts the histogram of the serrated wing while (b') shows the histogram of the smooth wing. Here, N represents the number of occurrences during ~ 20 shedding cycles.

5.5 Turbulent kinetic energy (TKE) budget

For an incompressible flow, the transport equation of the turbulent kinetic energy (TKE) per unit mass (q) can be written as:

$$\frac{D}{Dt} \frac{\overline{q^2}}{2} = \underbrace{-\frac{\partial}{\partial x_i} \overline{u' \left(\frac{p'}{\rho} + \frac{q^2}{2} \right)}}_{(I)} - \underbrace{\overline{u'_i u'_j} \frac{\partial \overline{U}_j}{\partial x_i}}_{(II)} + \underbrace{v \frac{\partial}{\partial x_i} \overline{u'_j \left(\frac{\partial u'_i}{\partial x_j} + \frac{\partial u'_j}{\partial x_i} \right)}}_{(III)} - \underbrace{v \overline{\left(\frac{\partial u'_i}{\partial x_j} + \frac{\partial u'_j}{\partial x_i} \right) \frac{\partial u'_j}{\partial x_i}}}_{(IV)} - \underbrace{v \overline{\left(\frac{\partial u'_i}{\partial x_j} + \frac{\partial u'_j}{\partial x_i} \right) \frac{\partial u'_j}{\partial x_i}}}_{(V)}$$

(5.5.1)

Equation 5.5.1 states that “the total change in q (I) equates to the work done by the total dynamic pressure of turbulence (II), plus the deformation work of the mean motion by the turbulent stresses (III), plus the work by the viscous shear stresses of the turbulent motion (IV) and the viscous dissipation of the turbulent motion (V)” (Hinze, 1987). The term (III) is known as TKE production term. This term (III) implies that exchange of kinetic energy with the mean flow occurs via deformation work done by the turbulence shear stresses which contributes to the turbulence energy of the flow. On the other hand, the term (V) is known as viscous dissipation term which implies that energy drain from turbulence occurs via deformation work by viscous stresses against the fluctuating strain rate (Lumley, 1972).

In this section, term (III) and (V) are estimated in different regions of the flow field to understand how serrations modify the generation and dissipation of turbulence. Also, the constituent parts of the term (III) and term (V) are presented to compare both cases and understand how serrations intensify/alleviate energy transfer from/to the mean flow. Note that, for turbulent production, $P_{ij} = \overline{u'_i u'_j} \frac{\partial \overline{U}_j}{\partial x_i}$ and

dissipation, $D_{ij} = v \overline{\left(\frac{\partial u'_i}{\partial x_j} + \frac{\partial u'_j}{\partial x_i} \right) \frac{\partial u'_j}{\partial x_i}}$ term, where $i, j=1, 2, 3$ meaning there are nine

production terms and nine dissipation terms (i.e., P11, D11, P12, D12, ..., P33, D33). Here, 1 refers to streamwise component, 2 refers to cross-stream component, and 3 is spanwise component.

Figure 5.5.1 shows the local production and dissipation of turbulence inside the shear layer in plane 1 and 2 (figure 5.5.1(a)). Note that, plane 1 intersects a serration geometry while plane 2 is located in-between two neighboring serrations. Near the serrations, the peak of turbulence production can be observed in plane 2 (figure 5.5.1(c)); however, in plane 1, this peak is slightly further downstream. Such difference arises from the three dimensionalities of the serrations as plane 2 intersect the tip of one serration (although the plane 2 is located in-between two neighboring serrations, the spanwise angle of the serration in plane 1 causes the tip of the serration to impact the shear layer at the middle of two serrations). This interference can be better visualized in figure 5.2.3 where iso-surfaces of Q-criterion are shown colored with streamwise vorticity. The shear layer also exhibits spanwise variation of streamwise vorticity near the serrations (i.e., positive streamwise vorticity in plane 1, negative in plane 2) in figure 5.2.3. Unlike the smooth wing, serrated wing exhibits a sharp drop off from the peak local production ($0.025-0.05 z/c$ in figure 5.5.1c) near the leading edge. This is in line with local helicity density fluctuations (figure 5.4.1) near the LE of both the wings. Hence, in contrast to the shear layer of the smooth wing, serrated wing having high magnitudes of helicity density close to the LE is indicative of increased local production of turbulence. Further downstream ($0.05 - 0.2 z/c$), serrated wing shows much lower production of turbulence compared to the smooth case. Also, total production of turbulence appears almost identical in both planes

(0.05 – 0.2 z/c location in plane 1 and 2) for both the smooth and the serrated wing. Even for the total dissipation of turbulence (figure 5.5.1c), the difference in magnitudes (between plane 1 and 2) only appears near the LE of the serrated wing's shear layer while the smooth wing does not exhibit any significant variation. The overall dissipation of turbulence exhibits a consistent trend in both cases within the shear layer, however, the smooth wing dissipates slightly higher turbulent energy. In addition, both cases exhibit much higher local production of turbulence compared to the local dissipation inside the shear layer.

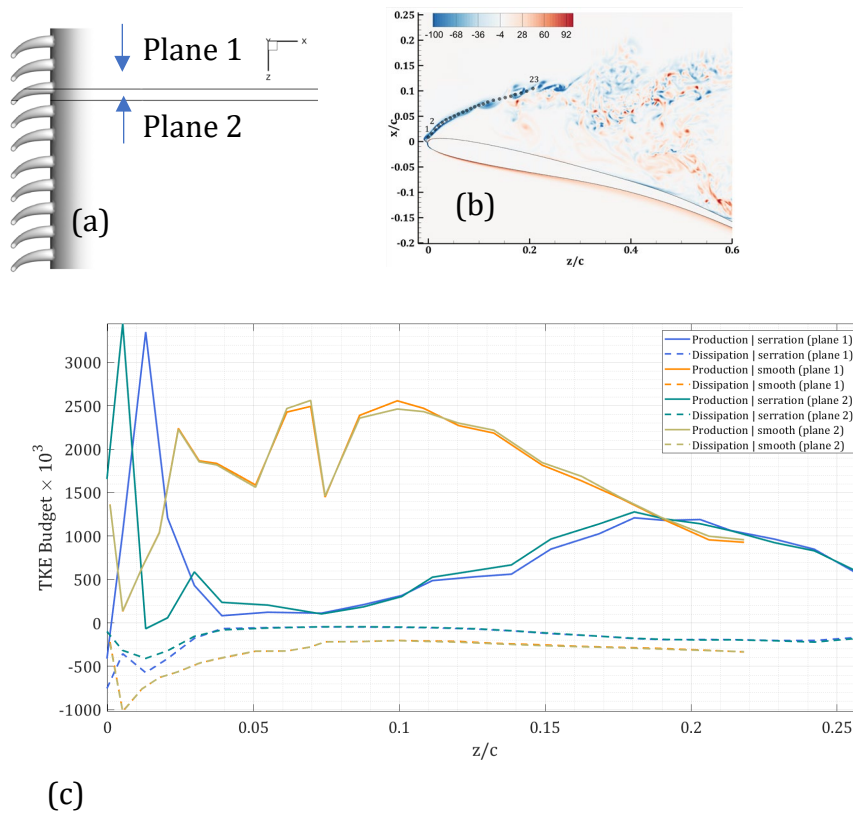


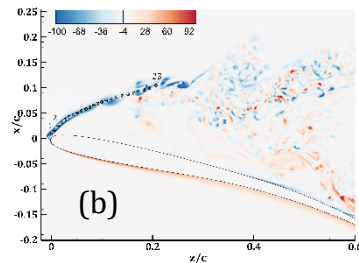
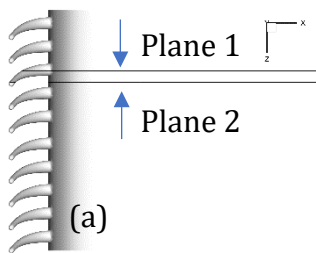
Figure 5.5.1: Local production and dissipation of turbulence inside the shear layer (c) for both the serrated and the smooth wing. The terms were calculated from the data

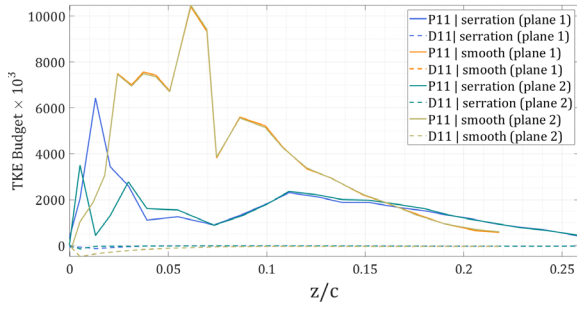
points shown in (b) located in two planes (plane 1 and plane 2) shown in (a). Plane 1 intersects a serration geometry at the leading-edge while plane 2 is located between two serrations. Same setup has also been maintained for the smooth leading-edge case.

For both the wings, the main sources of turbulence production are P11 (figure 5.5.2c) and P12 (figure 5.5.2d) while P21 (figure 5.5.2f) and P22 (figure 5.5.2g) are the main sinks. The other terms such as P13 (figure 5.5.2e), P23 (figure 5.5.2h) also contribute to the total local production term but their magnitudes are trivial as compared to the main source/sink terms of turbulence production. In the DNS study by Cimarelli *et al.* (2019), it was demonstrated that positive production mechanism at the LE shear layer is driven by streamwise compression of the mean flow ($\frac{\partial \bar{W}}{\partial z} < 0$, mean flow deceleration). In this study, both the streamwise gradient of streamwise ($\frac{\partial \bar{W}}{\partial z}$) and cross-stream ($\frac{\partial \bar{U}}{\partial z}$) mean flow contribute significantly to the positive production of turbulence (P11 and P12). In figure 5.5.3, both gradients ($\frac{\partial \bar{W}}{\partial z}, \frac{\partial \bar{U}}{\partial z}$) are compared near the LE shear layer corresponding to the data points where production and dissipation are calculated. Comparing figure 5.5.2(c, d) with figure 5.5.3, it can be observed that for the serrated wing, streamwise gradients of the mean flow are smaller ($0-0.15z/c$) in terms of magnitude compared to the smooth wing; therefore, serration has an initial effect on diminishing the streamwise mean flow gradients (mean flow deceleration) inside the LE shear layer which leads to a lower production of turbulence. This effect can also be observed in figure 5.3.2 where TKE profiles for

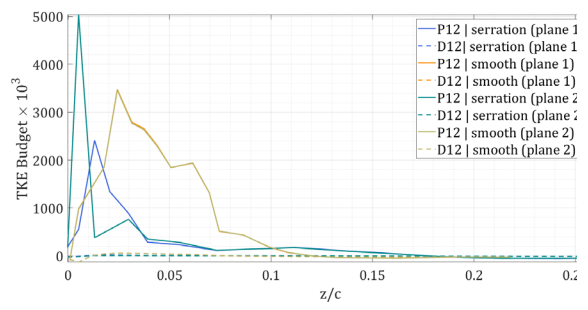
both the wings are shown at different region of the flow. However, this effect does not persist downstream the flow as TKE increases rapidly with the spatial and temporal development of the shear layer.

In a LE shear layer, negative local production is not uncommon and mainly occur due to positive correlation between Reynolds shear stress and mean flow shear (Cimarelli *et al.*, 2019) (i.e., P21). As the Reynolds stress is predominantly positive near the LE for both cases (figure 5.3.4a, a'), the term P21 act as a sink of TKE unlike classical production of turbulence where Reynolds stress and mean flow shear are negatively related. Similarly, P22 is also a sink of TKE; $\langle u'u' \rangle$ and $\frac{\partial \bar{U}}{\partial x}$ are positively related in this case ($\frac{\partial \bar{U}}{\partial x} > 0$). On the other hand, the constituent terms of the total local dissipation (i.e., D11, D12, ..., D33) do not exhibit any significant difference between the two cases (figure 5.5.2 c-k); both cases exhibit comparable magnitudes and trends (note that, the budget terms are multiplied with 10^3 , hence, the actual difference is less than what visually appears in the plots).

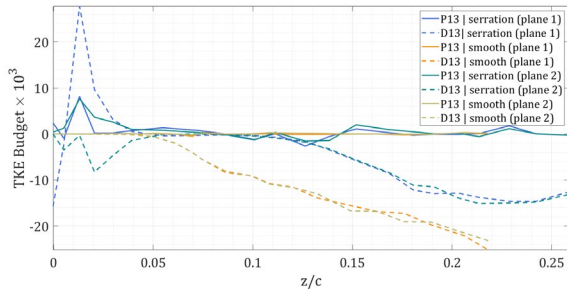




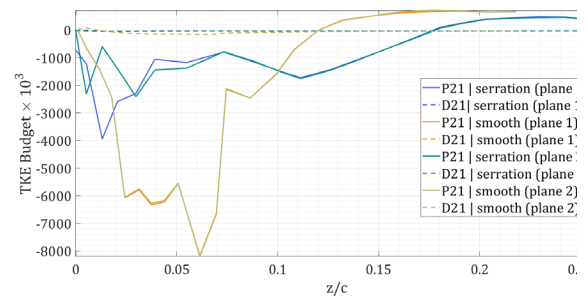
(c)



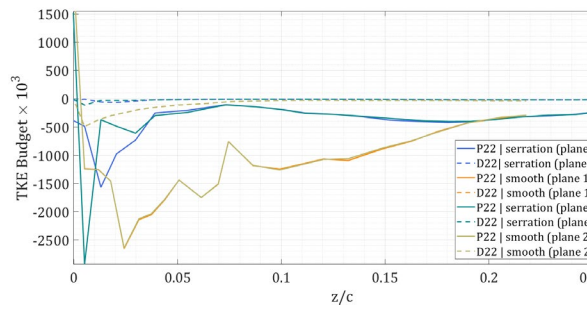
(d)



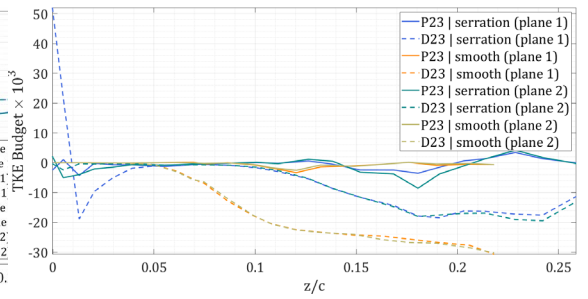
(e)



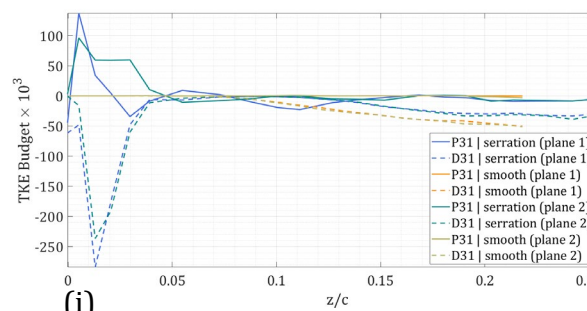
(f)



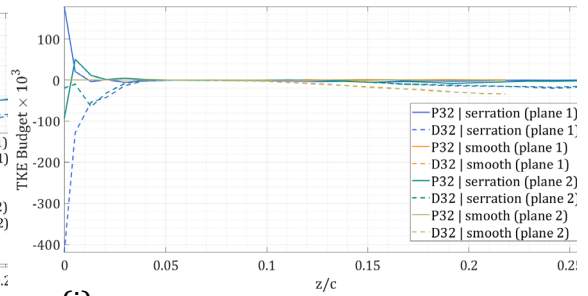
(g)



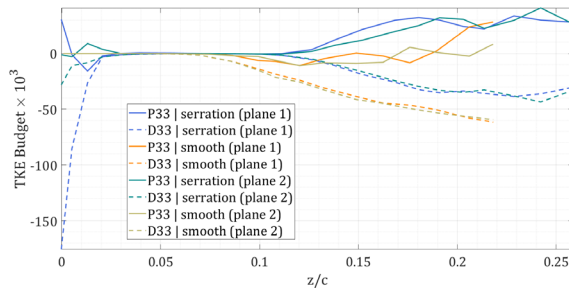
(h)



(i)



(j)



(k)

Figure 5.5.2: Comparison of constituent terms of turbulence production and dissipation inside the shear layer (b) for both the serrated and the smooth wing. The terms were calculated from the data points shown in (b) located in two planes (plane 1 and plane 2) shown in (a). Plane 1 intersects a serration geometry at the leading-edge while plane 2 is located between two serrations. The subfigures (c)-(k) depict the following constituent terms in plane 1 and 2: (c) P11, D11 (d) P12, D12 (e) P13, D13 (f) P21, D21 (g) P22, D22 (h) P23, D23 (i) P31, D31 (j) P32, D32 (k) P33, D33.

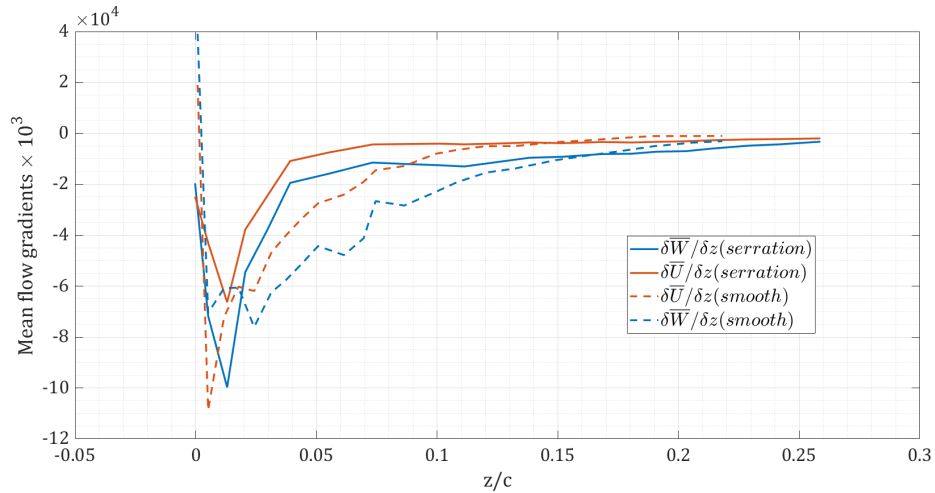
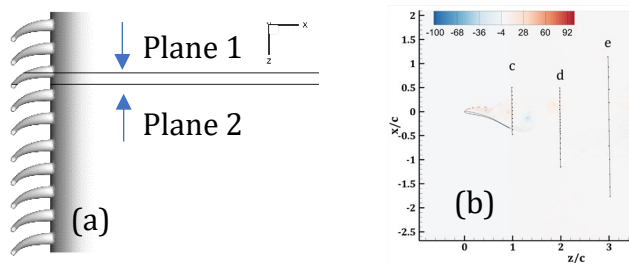


Figure 5.5.3: Comparison of streamwise gradients of the mean flow inside the shear layer of both the serrated and the smooth wing. The terms were calculated from the data points shown in figure 5.5.2b in plane 1 (figure 5.5.2a).

Local production and dissipation of TKE are also estimated at the wake. In figure 5.5.4b, the locations of the wake profiles are shown which were estimated from the probe data along the profiles. It is important to note that the vertical extent of the wing (20° AOA) is from 0 x/c to -0.5 x/c . At profile 1 (for both cases), the wake can be divided into two segments; positive production zone (0.4 x/c to -0.05 x/c) and negative production zone (-0.05 x/c to -0.5 x/c). As mentioned earlier, negative production originates from the positive relation between Reynolds shear stress and mean flow shear; positive Reynolds stress occurs due to large temporal scale phenomena (that induces positive $\langle u'w' \rangle$) prevailing over small ones that induces positive production (Cimarelli *et al.*, 2019). In figure 5.3.4, it can be observed that the Reynolds stress is positive in the negative production region at the near wake. The negative production region in wake profile (c) borders the TEV while the positive production zone is mostly affected by the interaction between SV and TEV. Therefore, the TEV is inducing positive Reynolds stress in our case in conjunction with mean flow deceleration that leads to negative local production of turbulence. In the study by Krishnan (2022), he analyzed the wake profiles of owls during their flapping flights. He found that the wake profiles had positive production value all over. However, the experiments were conducted using live birds having all the wing features intact (i.e., TE fringes, velvety surface, LE serrations, etc.) while the simulation only accounts for LE serrations which may explain the difference as the flow which develops over the wing will also interact with the surface and the TE features.

In figure 5.5.4c, the profiles of turbulence production at the wake do not vary significantly between the two spanwise planes of the same case (i.e., serration/smooth). The serrated wing exhibits higher turbulence production (positive segment) compared to the smooth case. On the other hand, total dissipation profiles are very similar for both cases. Further downstream (1 chord length away), the TKE production profiles (d) depict positive values in general, while the peak values remain at the upper section of the profile for both the cases (i.e., passage of the shedded vortices). In addition, the difference in magnitudes between the two planes of the same case (i.e., serration/smooth) starts to become noticeable which eventually becomes more pronounced as the flow travels further away from the wing (figure 5.5.4 (e)). In the wake profile (e), the serrated wing exhibits a reduction in the total production of turbulence compared to the smooth case. Additionally, there is a slight increase in total dissipation for the serrated wing. In summary, the comparison of the two cases reveals that the production and dissipation profiles at the wake are not significantly different. This observation is consistent with the comparison of Turbulent Kinetic Energy (TKE) profiles illustrated in figure 5.3.2.



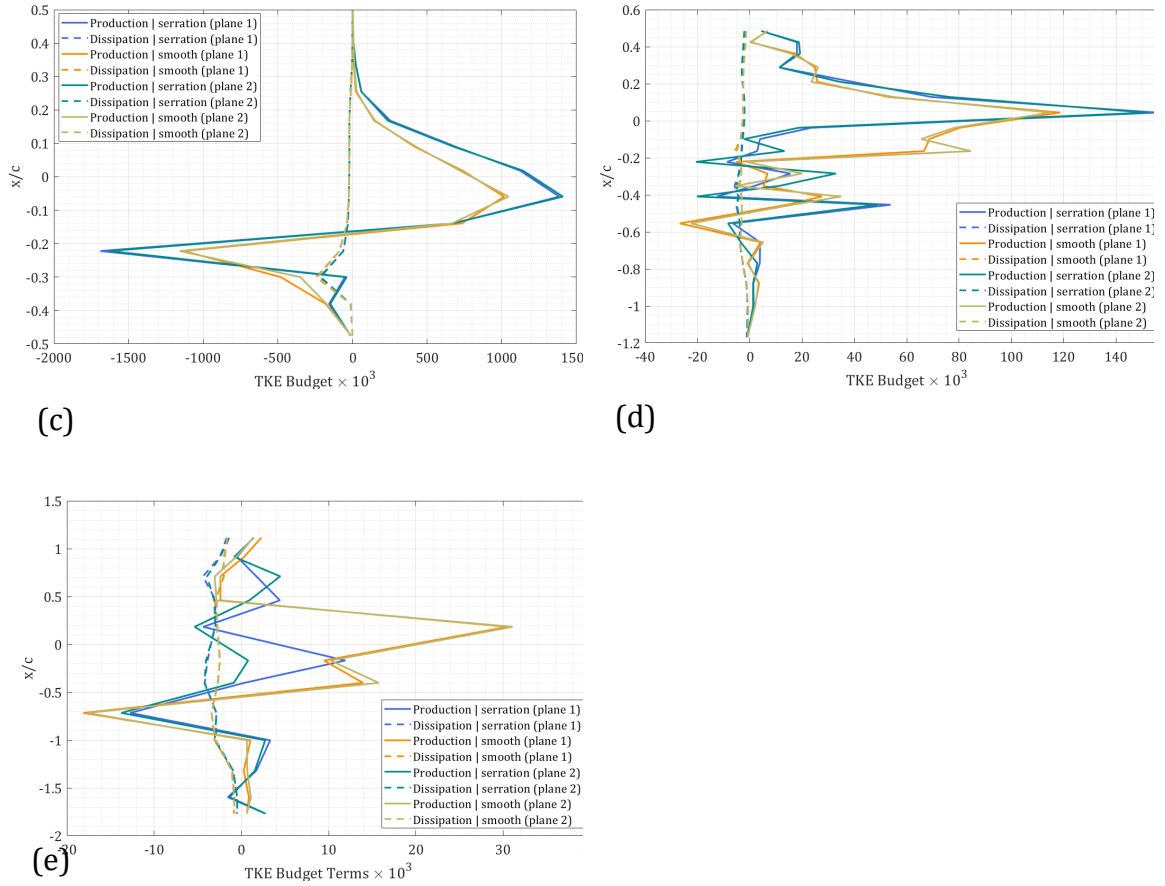


Figure 5.5.4: Local production and dissipation of turbulence at the wake of both the serrated and the smooth wing. The terms were calculated at the profiles shown in (b).

Two spanwise planes (plane 1 and 2 as shown in (a)) were considered for the comparison of the profiles for both the serrated and the smooth wing.

5.6 Estimation of integral scales at the wake

Velocity measurements at several points over time can be converted into spatially distributed data using Taylor's hypothesis. Taylor's hypothesis posits that turbulent eddies are embedded in a stationary turbulence field carried downstream at a mean local velocity \bar{U} (note that, in Taylor's hypothesis, average convection velocity is used;

however, local mean velocity can also be utilized for this approximation at the wake)(Swamy *et al.*, 1979; Lewalle and Ashpis, 2004)) in the streamwise direction, $\Delta z = \bar{U} T_w$, (T_w , is the integral time scale determined from auto-correlation of $w'(t)$) (Swamy *et al.*, 1979; Lewalle and Ashpis, 2004). Consequently, these eddies are assumed to remain unchanged over time, t . For any velocity component,

$$T_i = \int_0^{\infty} R_i(\tau) d\tau \approx \int_0^{\tau_0} R_i(\tau) d\tau, \quad (5.6.1)$$

$$R_i(\tau) = \frac{i(t)i(t+\tau)}{\sigma_i^2}.$$

Here, $i = w', u', v'$ denotes to streamwise, cross-stream and spanwise velocity fluctuations, respectively. In equation 5.6.1, R_i refers to auto-correlation of a fluctuating velocity component's time series whereas σ_i denotes to its standard deviation. The corresponding length scales then can be calculated from, $L_i = T_i \bar{U}$.

In figure 5.6.1, longitudinal (L_w/c) and transverse (L_u/c) integral length scales are shown. Spanwise length scale (L_v) is not estimated in this study as the flow domain is limited in the spanwise direction; since the method of approximation (eq. 5.6.1) utilizes temporal auto-correlation (to calculate integral scales) instead of spatial auto-correlation, fully developed spanwise flow is required to obtain realistic approximation of the corresponding scale. We can observe from the figure 5.6.1 that the peak correlations are found at the upper portion ($0-1x/c$) of the wake profile (e) similar to what observed at the TKE budget profile in figure 5.5.4 (due to the passage of shedded vortices). Unlike the findings by Krishnan (2022) (experimental study using real owl), serrated wing depicts much larger longitudinal and transverse scales.

Krishnan (2022) found that longitudinal and transverse scale measuring approximately $0.18c$ and $0.22c$, respectively. In this study, peak value of L_w is found to be $0.78c$ while the peak value of L_u is $0.38c$ for the serrated wing. Therefore, microscale serrations do not reduce the large scales of the flow at stall AOA rather it enlarges the average size of eddies in the wake. It is important to note that the study by Krishnan (2022) does not account for stall AOA; hence, the difference in AOA might also be source of such high differences in integral scale magnitudes (between both studies). In fact, Sedaghatizadeh (2018) showed that for a NACA0012 airfoil, integral length scale increases from $0.35c$ (5° AOA) to $0.68c$ (18° AOA) along the wake.

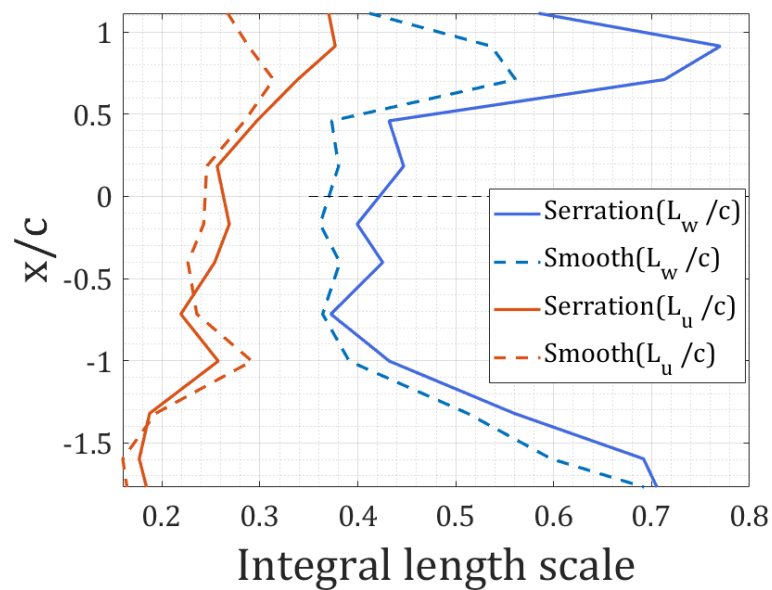


Figure 5.6.1: Longitudinal and transverse length scales

(L_w, L_u) estimated at the wake profile (e) in plane 1 as shown

in figure 5.5.4(a) and figure 5.5.4(b).

Chapter 6

Experimental study using 3D printed owl wing

In the preceding chapter, the results of the numerical simulation of an owl wing, both with and without leading edge (LE) serrations, were presented. This chapter delves into the investigation of the impact of serrations on the boundary layer of an owl wing using Particle Image Velocimetry (PIV). A comparative study between owl wing models with and without serrations was carried out to ascertain the changes in the boundary layer across a range of angles of attack (Saussaman *et al.*, 2023). It is important to clarify that the purpose of this experimental investigations is not to draw comparisons with the data from the numerical study outlined in the previous chapter. Instead, the objective is to comprehend how serrations influence the boundary layer over the entire three-dimensional (3D) owl wing. Due to limited computational resources, the flow simulation setup detailed in Chapter 4 encompassed only a limited portion of the owl wing across the span. In contrast, the present experiment involves a comprehensive 3D model of an owl wing employing the same airfoil as the numerical study (Saussaman *et al.*, 2023).

It is important to note that the LE serrations on the owl wing model used in the experiments (3D printed) do not precisely replicate the size and shape of the serrations due to the minimum size limitations imposed by the 3D printer model

owned by Coastal Carolina University. Nevertheless, the experiments conducted on a full 3D owl wing demonstrate how the boundary layer is altered in the spanwise direction. The experimental study involves two wing models (with and without serrations) tested in a recirculating water flume. A dead barred owl wing was electronically scanned, as shown in figure 6.1A, and was used to generate a 3D model in SolidWorks (see Figure 6.1B). Optical flow measurement techniques were employed to analyze the flow within the boundary layer formed over the wing at $Re_c = U_\infty c / \nu = 49,000$. For a comprehensive overview of the experimental setup and the model configurations tested, please refer to the detailed description provided in the publication by Saussaman *et al.*, 2023. However, it is crucial to emphasize that the conducted experiments focused exclusively on examining the characteristics of the suction surface boundary layer in relation to the variation of angle of attack (AOA). Three AOA was investigated: 6° , 12° , and 20° , for two wing configurations (with and without serrations). For each angle of attack, the flow over the wings was measured at five different planes: 0%, 25%, 50%, 75%, and 95% of the wingspan from the root (herein as the root (P1), root-to-mid (P2), mid (P3), mid-to-tip (P4) and tip (P5), respectively) as shown in figure 6.2: right. Sampling across the wingspan offered a three-dimensional perspective on the flow evolution in the spanwise direction.

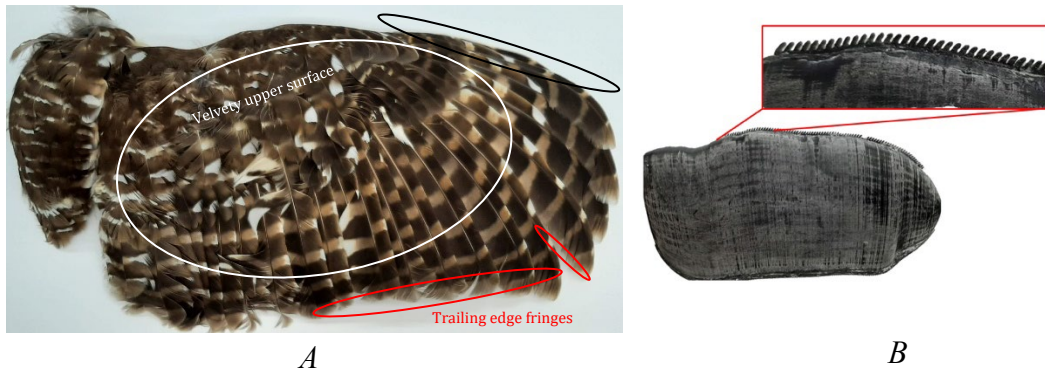


Figure 6.1: A: Barred owl wing (left) with the specific features commonly found in nocturnal owls' species: leading-edge serrations, velvety upper surface (elongated pennula), and trailing-edge fringes. B: 3D printed wing with a closeup of the serrations (Saussaman et al., 2023).

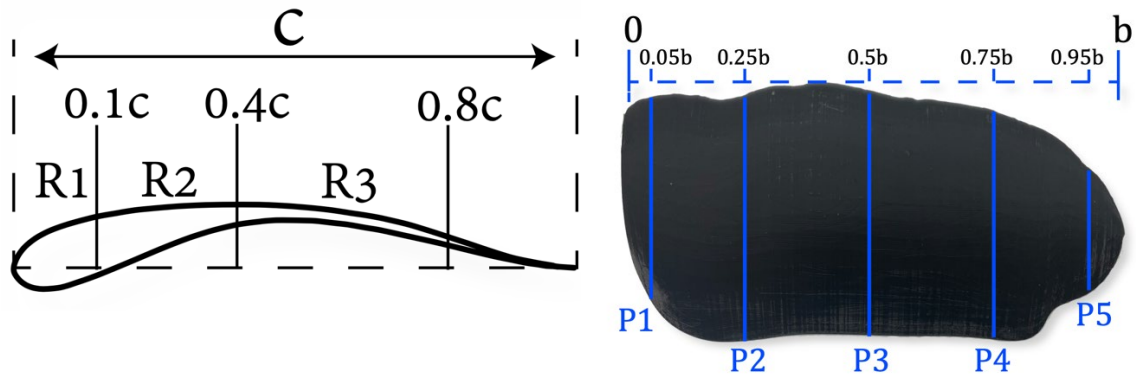


Figure 6.2: Schematic description of the field of view locations where measurements were performed. Left: wing cross section divided into three arbitrary regions: leading-edge (R1), separation (R2), and reattachment (R3), where c is the chord. Right: wing planform; blue lines represent the five different measured PIV planes where b is the wing spanwise length (Saussaman et al., 2023).

6.1 Boundary layer characteristics

To better characterize the flow over the suction surface of the wing, the boundary layer developed over each plane (i.e., P1, P2, ..., P5) was divided into three distinct regimes (refer to figure 6.2, left): R1) leading-edge: spanning from 0 to $0.1c$, where the boundary layer forms; R2) separation region, covering 0.1 to $0.4c$; where, at relatively high angles of attack, the flow might separate, leading to the collapse of the boundary layer; and R3) reattachment region, spanning from 0.4 to $0.9c$, where, at certain angles of attack, the flow can reattach, and the boundary layer may reform. The analysis excluded the region near the trailing edge due to laser reflections hindering reliable measurements in this small area.

Figures 6.1.1-6.1.3 function as comparative illustrations where the ratio between the serrated and smooth wing is calculated for each flow property. A ratio below one indicates that the property value is lower for the serrated wing, while a ratio above one suggests the opposite, with the smooth wing having a higher property value. In figure 6.1.1, mean streamwise velocity profile deficit (proportional to displacement deficit (δ)) ratio within the boundary layer is shown for both the wings. The procedures to estimate velocity profile deficit ratio is briefly discussed in Saussaman *et al.*, 2023. At 6° AOA, the inclusion of leading-edge serrations results in an increased δ compared to the smooth wing case across the span, particularly at the leading edge and middle regions. Across all AOAs along the span, the serrated case at R3, toward the trailing edge, exhibited a significantly thinner boundary layer compared to the smooth case. This trend is consistent for 12 degrees and 20 degrees as well, with a thinner boundary layer at the leading edge and a flipped pattern in the middle section,

akin to the 6-degree case. This underscores the influence of angle of attack on flow dynamics, as discussed by Ben-Gida *et al.* in 2020.

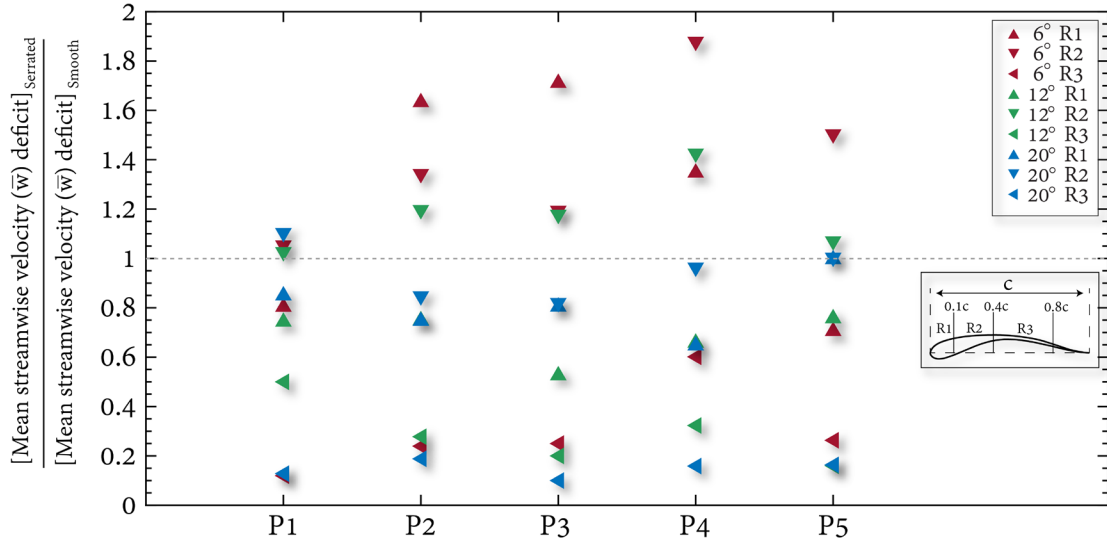


Figure 6.1.1: The mean streamwise velocity profile deficit ratio within the boundary layer between the serrated and smooth case in the streamwise-normal planes at different spanwise locations (P1, P2, P3, P4, P5). In the sub-panel, c denotes to chord length of the wing (Saussaman *et al.*, 2023).

To evaluate the influence of turbulence in the presence of serrations, the ratio of turbulent quantities (such as Reynolds stress, turbulent kinetic energy, etc.) between the serrated and smooth cases was calculated. Turbulence modulations were characterized through the ratio of maximal value, emphasizing conditional differences between planes and angles of attack, coupled with the presence or absence of serrations at the leading edge.

Figure 6.1.2 illustrates the ratios of the maximal Reynolds stress component in spanwise-normal planes in relation to the AOA and spanwise plane location over the wing planform. The horizontal axis represents the plane location denoted as P1, P2, P3, P4, and P5 in accordance with the experimental setup, while the vertical axis denotes the maximal Reynolds stress ratio. The absolute values of the maximal Reynolds stress within the boundary layer exhibit a consistent trend, increasing across planes with a rise in the angle of attack. However, values at the root location were somewhat inconsistent, possibly due to edge effects from the connecting rod (that holds the 3D printed wing during the experiments) (Saussaman *et al.*, 2023). Generally, ratios at 6° and 12° are predominantly higher than 1, with exceptions at the leading-edge region in the tip (12° , R1) and P2 (6° , R1). At 20° AOA, the ratio over the wing was generally lower than one, with sporadic values above and below one. This distribution suggests that the impact of serrations on turbulence levels is not linear, as their effect is coupled with the angle of attack and the elliptical planform of the wing resembling that of a natural owl wing. Similar trends are also observed in the distribution of turbulent kinetic energy at the boundary layer (refer to figure 6.1.3 for the turbulent kinetic energy ratio), indicating that turbulence modulation varies distinctly at different angles of attack due to the presence of serrations.

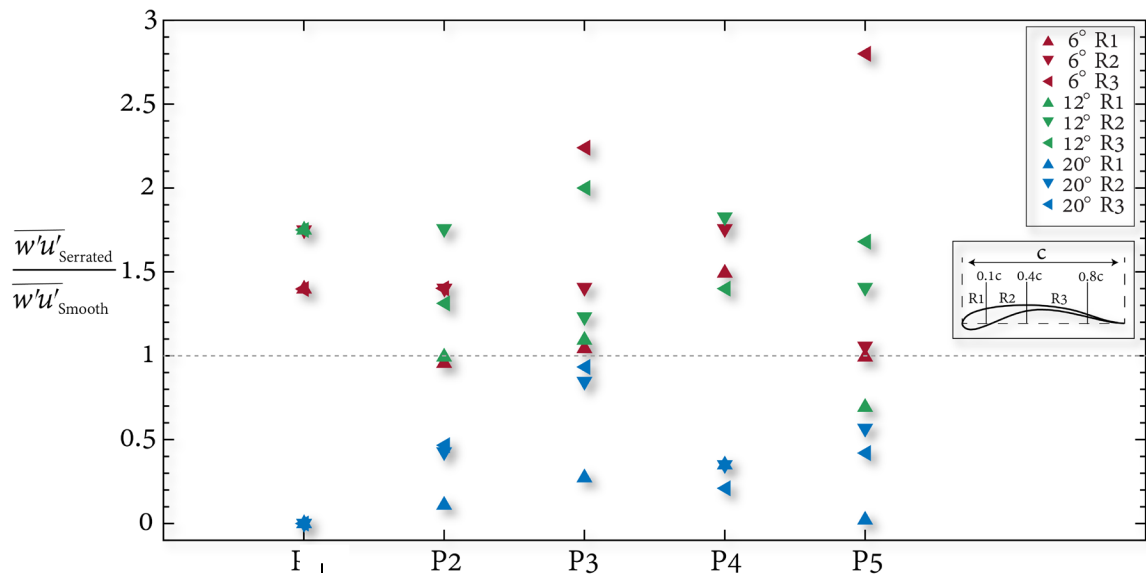


Figure 6.1.2: The ratio of the maximal Reynolds stress component ($\overline{w'u'}$) between the serrated and smooth case in the streamwise-normal planes at different spanwise locations (P1, P2, P3, P4, P5). Here, w' refers to streamwise velocity fluctuation, and u' refers to vertical velocity fluctuation (Saussaman et al., 2023).

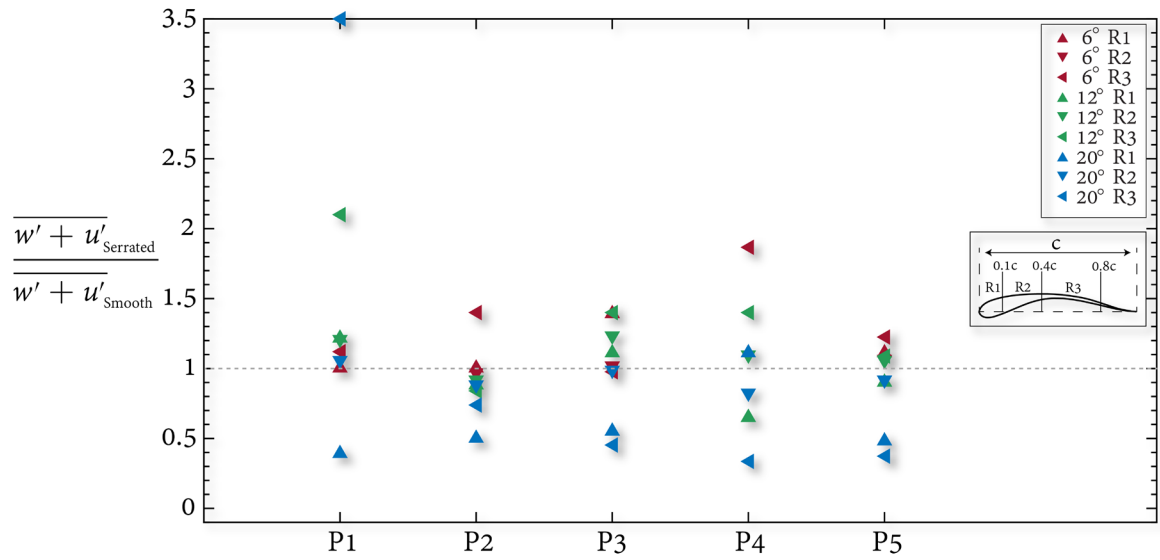


Figure 6.1.3: The ratio of the maximal turbulent kinetic energy $\overline{(w' + u')}$ between the serrated and smooth case in the streamwise-normal planes at different spanwise locations (P1, P2, P3, P4, P5). Here, w' refers to streamwise velocity fluctuation, and u' refers to vertical velocity fluctuation (Saussaman et al., 2023).

Chapter 7

Summary and conclusion

The present study demonstrates the impact of owls' microscale leading-edge serrations on the flow dynamics of an owl wing. Owl's serrations are significantly smaller than their wing chord length ($\sim 1-2\%$ of the chord length) and their size and shape are highly three-dimensional, oriented at an angle with the freestream. Most of the numerical studies simplifies the size and shape of the serrations via modeling them into sinusoidal, sawtooth, and similar shapes to reduce the complexities associated with numerical simulations (Jaworsky and Peake, 2020; Wang *et al.*, 2019). In this research, serrations are designed based on the data obtained from the research conducted by Bachmann and Wagner (2011). The study provides exact size, shape and orientation of serrations as those found on actual owl wings. Via utilizing direct numerical simulation method, the flow around the model owl wing (with and without serrations) is resolved to the smallest scales at 20° AOA with the Reynolds number 40,000. In order to elucidate the flow physics associated with serrations on owl wings, the results of the numerical simulations for two cases are compared, shedding light on how serrations modify the flow field. It is important to note that to reduce the computational costs associated with numerical simulations and data post-processing, this study utilizes a computational domain that extends to $0.062c$ in the spanwise

domain which limits the solver's capability to capture large spanwise phenomena such as tip vortex system. Although this choice is rather restricting in terms of full spanwise flow development, both cases studied in this research contain similar restrictions; hence, the findings from this comparative study won't be affected by the inaccuracies by a large margin.

Typically, during landing, take-off and prey capture, owls fly at high AOA. However, during take-off, high AOA is observed accompanied with wing flapping. This simulation setup can be associated with landing or prey capture phase while the owl is not flapping. During these stages, owls need to slow down and increased lift is required. The results from this study show that serrations prompt reduced aerodynamic performance compared to the smooth LE wing (3.2% decrease); however, lift production is enhanced by 2% which suggests that serration may contribute positively to owls' flight at high AOA during the landing and prey capture phase.

Separation bubble is detrimental to aerodynamic performance and stability of flight vehicles, birds, marine animals, etc. (Shy *et al.*, 2008; Serdar *et al.*, 2020). From the time-averaged results, it is found that serrations promote reverse flow weakening and its area reduction. Note that, the effectiveness of control surfaces in air vehicles (such as ailerons, flaps, spoilers, etc.) are dependent on the attached flow over them (Rao, 1984; Lochert, 2019). Similarly, birds also have multi-layered covert feathers which are generally deployed during high AOA maneuvers, landing, take-off, etc. Some of these covert feathers (i.e. secondary lesser coverts located near the leading-

edge) are known for enhancing maneuverability in birds' flights (Othman *et al.*, 2023). Serrations having weaker backflow and sustained reattached flow over the wing is favorable to other control feathers on owls' upper wing surface. Enhanced spanwise momentum transfer is also observed for the serrated case which is associated with facilitation of LEV stabilization during flapping flights (Jardin and David, 2014).

From the instantaneous flow visualizations, it was observed that both wings have asymmetric wake consisting of unequal strength vortices. The vortex shedding frequency is impacted due to the presence of serrations in the shear layer passage. Streamwise vorticity is developed early in the shear layer while passing through the array of serrations due to the spanwise deflection of the flow. As a result, three dimensionalities emerge earlier in the shear layer of the serrated wing. This impacts the downstream separation vortex formation mechanism so that during the trailing edge vortex formation and enlargement phase, a stronger separation vortex persists on the upper surface of the wing which drives more vorticity ejection from the wall. Therefore, serrated wing depicts larger secondary vortices ($\sim 0.5 z/c$) in the time-averaged profiles. Turbulence characteristics of the serrated wing is found to be different compared to what found in the real owl wings with serrations removed (Geyer *et al.*, 2017). We can observe an increase in TKE as well as Reynolds stress with the inclusion of serrations whereas the real owl wings show the opposite trend. This is due to other morphological features of the real owl wing which were not included in the model owl wing of this study.

Reynolds stress analysis suggest that serration enhances downward turbulent momentum transport over the wing, especially, near the trailing-edge where separation vortex and trailing edge vortex interacts mostly over the shedding cycle. It is commonly known that separation bubble formation and its intensity can be controlled via passive and active control methods (i.e., blowing, vortex generators, etc.) which essentially introduce turbulence generation upstream the separation point (Jahanmiri, 2011). Although AOA other than 20° has not been investigated in this study, it can be surmised that larger AOAs will have shear layers that will pass through the array of serrations. As turbulent momentum transport is ultimately increased due to this early onset of three dimensionality in the shear layer, it will improve “stall resistance” at larger AOA.

Turbulent characteristics profiles at the wake demonstrated that serrated wing had larger wake in comparison to the smooth leading-edge wing due to the upward deflection of the shear layer; however, the change in wake size does not persist more than seven chord length away downstream the trailing edge. In close proximity of the serrations ($0-0.02z/c$), the shear layer depicted high alignment of fluctuating velocity and vorticity field as opposed to the smooth LE which resulted in increased local production of turbulence. Although the production of turbulence was significantly enhanced near the serration ($0-0.02z/c$), it rapidly dropped off to a much lower value compared to the smooth case in the downstream region ($0.02-0.2z/c$). However, further downstream ($z/c > 0.2$), this effect was not observed in the TKE profiles as the serration started to generate more TKE in comparison to the smooth LE case. Similar phenomenon was also observed in the experimental study by Hasheminejad

et al. (2020) where they modeled “sawtooth” type serrations at the trailing edge of a NACA 65(12)-10 airfoil at 0° angle of attack. The “sawtooth” type serrations which had a length of ~30% of the wing chord were shown to significantly reduce TKE level at the near wake via suppressing the coherent structures at the wake. The reduction occurred after the turbulent boundary layer at TE interacted with the sawtooths. In the current study, the flow was set to be uniform at the inlet with zero inflow turbulence. Although the current research and the study by Hasheminejad *et al.* (2020) are vastly different in terms of set-ups and models, they both demonstrate that serrations and “serration-like” structures can reduce TKE in the immediate vicinity. However, in the current research, the wake flow behind the model owl wing with serrations did not demonstrate any notable differences compared to the smooth LE wing. Also, the integral scales at the wake of the serrated wing was found to be larger than the smooth case which implies that the addition of serration array at the leading-edge does not improve the wake turbulence.

The impact of leading-edge serrations on the boundary layer development over a full 3D owl wing (with and without serrations) was also studied using experimental method: particle image velocimetry (Saussaman *et al.*, 2023). While the experimental setup deviates from the simulation setup, it effectively compares two scenarios (with and without serrations) within a similar Reynolds number range. This approach allows an understanding of how serrations influence the boundary layer when considering a full three-dimensional wing. A 3D printed owl wing was employed for the experimental analyses while the serrations were designed based on approximated size and shape from the digital images. The wing models were tested

in a recirculating water flume and 2D-PIV were performed at 6° , 12° and 20° angles of attack to obtain the velocity field in the spanwise-normal planes. Data were collected in five spanwise-normal planes across the 3D printed wing. The findings suggest that leading-edge serrations alter the boundary layer over the wing at all angles of attack, but not in a similar manner. Specifically, there is no clear trend in the difference between the serrated and smooth wing when considering the mean streamwise velocity deficit ratio (Saussaman *et al.*, 2023).

In the analysis of various turbulent characteristics, it is observed that the serrations amplify turbulence at low to moderate angles of attack. Conversely, at a high AOA, turbulence suppression occurs. The observation holds true for turbulent ratios, including Reynolds stress and turbulent kinetic energy (TKE), which exhibit variations across the wing's span at all angles of attack, irrespective of enhancement or suppression. Notably, the spanwise variation in turbulent ratios is more pronounced for the 6° and 12° cases compared to the 20° case (Saussaman *et al.*, 2023). The findings suggest that the presence of serrations, coupled with an elliptical planform shape and a high angle of attack, results in the deintensification of three-dimensional effects on the flow

Bibliography

- Abbot, I. H., Doenhoff, E. A. and Stivers, L. S. (1945). Summary of airfoil data. NASA Report No. 824.
- Al-Battal, N., Cleaver, D. and Gursul, I. (2016). Aerodynamic load control through blowing. *54th AIAA Aerospace Sciences Meeting*.
- Anderson, G.W. (1973). An experimental investigation of a high lift device on the owl wing. Master's Thesis, Air Force Institute of Technology, Wright-Patterson AFB.
- Anderson, J. D. (2017). *Fundamentals of aerodynamics*. McGraw-Hill Education.
- André, J. C., and Lesieur, M. (1977). Influence of helicity on the evolution of isotropic turbulence at high Reynolds number. *Journal of Fluid Mechanics*, 81(01), 187.
- Anyoji, M., Wakui, S., Hamada, D. and Aono, H. (2018). Experimental study of owl-like airfoil aerodynamics at low Reynolds numbers. *Journal of Flow Control, Measurement & Visualization*, 6, 185-197.
- Bachmann, T. (2010). Anatomical, morphometrical and biomechanical studies of barn owls' and pigeons' wings. Master's thesis, RWTH Aachen University.
- Bachmann, T. and Wagner, H. (2011). The three-dimensional shape of serrations at barn owl wings: towards a typical natural serration as a role model for biomimetic applications. *Journal of anatomy*, 219(2), 192-202.
- Bachmann, T., and Winzen, A. (2014). Owl inspired silent flight. *World Scientific Series in Nanoscience and Nanotechnology*, 695–717.

- Bachmann, T., Klän S., Baumgartner, W., Klaas, M., Schröder, W. and Wagner, H. (2007). Morphometric characterization of wing feathers of the barn owl (*Tyto alba*) and the pigeon (*Columba livia*). *Frontiers in Zoology*, 4, 23.
- Bachmann, T., Wagner, H., and Tropea, C. (2012). Inner vane fringes of barn owl feathers reconsidered: morphometric data and functional aspects. *Journal of Anatomy*, 221(1), 1–8.
- Balaras, E. (1995). Large eddy simulation of high Reynolds number wall bounded shear layers. *Ph.D. Dissertation*, Swiss Federal Institute of Technology.
- Balaras, E. (2004). “Modeling Complex Boundaries Using an External Force Field on Fixed Cartesian Grids in Large-Eddy Simulations. *Computers & Fluids*, Vol. 33, No. 3, pp. 375–404.
- Balci, A., Andersen, M., Thompson, M. C. and Brøns, M. (2015). Codimension three bifurcation of streamline patterns close to a no-slip wall: A topological description of boundary layer eruption. *Physics of Fluids*, 27(5), 053603.
- Bannier, A., Garnier, E. and Sagaut, P. (2016). Friction drag reduction achievable by near-wall turbulence manipulation in spatially developing boundary-layer. *Physics of Fluids*, 28 (035108), 16.
- Bearman, P. W. (1984). Vortex Shedding from Oscillating Bluff Bodies. *Annual Review of Fluid Mechanics*, 16(1), 195–222.
- Ben-Gida, H., Gurka, R., and Weihs, D. (2020). Leading-edge vortex as a high-lift mechanism for large-aspect-ratio wings. *AIAA Journal*, 58(7), 2806–2819.

- Beratlis, N. (2008). Direct numerical simulations of transitional pulsatile flow in stenotic vessels. PhD thesis, University of Maryland.
- Beratlis, N., Capuano, F., Krishnan, K., Gurka, R., Squires, K., and Balaras, E. (2020). Direct numerical simulations of a great horn owl in flapping flight. *Integrative and Comparative Biology*, 60 (5), 1091–1108.
- Bostrom, E. (2015). Investigation of outflow boundary conditions for convection-dominated incompressible fluid flows in a spectral element framework. Master's Thesis in Scientific Computing, KTH Royal Institute of Technology.
- Boutilier, M. H., Yarusevych, S. (2012). Effects of end plates and blockage on low-Reynoldsnumber flows over airfoils. *AIAA Journal*, 50, 1547–59.
- Bradshaw, P. (1987). Turbulent secondary flows. *Annual Review of Fluid Mechanics*, 19(1), 53–74.
- Breuer, M., and Jovičić, N. (2001). Separated flow around a flat plate at high incidence: an LES investigation. *Journal of Turbulence*, 2, N18.
- Broeren, A. P. and Bragg, M. B. (2001). Unsteady Stalling Characteristics of Thin Airfoils at Low Reynolds Number. *Fixed and Flapping Wing Aerodynamics for Micro Air Vehicle Applications*, 191–213.
- Buresti, G. (2000). Bluff-body aerodynamics. International Advanced School on Wind-excited and Aeroelastic Vibrations of Structures, Genoa, Italy.
- Busse, A., Lützner, M., and Sandham, N. D. (2015). Direct numerical simulation of turbulent flow over a rough surface based on a surface scan. *Computers & Fluids*, 116, 129–147.

- Cantwell, B. and Coles, D. (1983). An experimental study of entrainment and transport in the turbulent near wake of a circular cylinder. *Journal of Fluid Mechanics*, 136(-1), 321.
- Chakraborty, P., Balachandar, S. and Adrian, R. J. (2005). On the relationships between local vortex identification schemes. *Journal of Fluid Mechanics*, 535, 189–214.
- Chang, J., Zhang, Q., He, L., and Zhou, Y. (2022). Shedding vortex characteristics analysis of NACA 0012 airfoil at low Reynolds numbers. *Energy Reports*, 8, 156–174.
- Cimarelli, A., Leonforte, A., De Angelis, E., Crivellini, A., and Angeli, D. (2019). On negative turbulence production phenomena in the shear layer of separating and reattaching flows. *Physics Letters A*, 383(10), 1019–1026.
- Doligalski, T. L., Smith, C. R. and Walker, J. D. A. (1994). Vortex interactions with walls. *Annual Review of Fluid Mechanics*, 26(1), 573–616.
- Duraisamy, K. (2005). Studies in tip vortex formation, evolution and control. Ph.D. thesis, University of Maryland, College Park.
- Eisenbach, S., and Friedrich, R. (2007). Large-eddy simulation of flow separation on an airfoil at a high angle of attack and $Re = 105$ using Cartesian grids. *Theoretical and Computational Fluid Dynamics*, 22(3-4), 213–225.
- Freymuth, P., Bank, W. and Palmer, M. (1984). Vortices around Airfoils: The flow around an airfoil in unsteady wind provides insight into a difficult realm of aerodynamics. *American Scientist*, 72(3), 242–248.

- Frohlich, J., Mellen, C. P., Rodi, W., Temmerman, L., and Leschziner, M. A. (2005). Highly resolved large-eddy simulation of separated flow in a channel with streamwise periodic constrictions. *Journal of Fluid Mechanics*, 526, 19–66.
- Genç, M. S., Koca, K., Demir, H. and Açikel, H. H. (2020). Traditional and new Types of passive flow control techniques to pave the way for high maneuverability and low structural weight for UAVs and MAVs. autonomous vehicles.
- Geyer, T.F., Claus V.T., Hall P.M. and Sarradj, E. (2017). Silent owl flight: the effect of the leading-edge comb. *International Journal of Aeroacoustics*, 16(3), 115-134.
- Giuni, M., and Green, R. B. (2013). Vortex formation on squared and rounded tip. *Aerospace Science and Technology*, 29(1), 191–199.
- Graham, R.R. (1934). The silent flight of owls. *The Aeronautical Journal*, 38, 837-843.
- Gruschka, H.D., Borchers, I.U. and Coble, J. G. (1971). Aerodynamic noise produced by a gliding owl. *Nature*, 233(5319), 409-11.
- Guha, A. and Rahmani, M. (2019). Predicting vortex merging and ensuing turbulence characteristics in shear layers from initial conditions. *Journal of Fluid Mechanics*, 878.
- Gurka, R., Liberzon, A. and Hetsroni, G. (2006). POD of vorticity fields: A method for spatial characterization of coherent structures. *International Journal of Heat and Fluid Flow*, 27(3), 416-423.

- Hain, R., Kähler, C. and Radespiel, R. (2009). Dynamics of laminar separation bubbles at low-Reynolds-number aerofoils. *Journal of Fluid Mechanics*, 630, 129–153.
- Hasheminejad, S. M., Chong, T. P., Lacagnina, G., Joseph, P., Kim, J.-H., Choi, K.-S., ... Stalnov, O. (2020). On the manipulation of flow and acoustic fields of a blunt trailing edge aerofoil by serrated leading edges. *The Journal of the Acoustical Society of America*, 147(6), 3932–3947.
- Hinze, J. O. (1987). *Turbulence*. McGraw-Hill.
- Hoarau, Y., Braza, M., Ventikos, Y., Faghani, D., and Tzabiras, G. (2003). Organized modes and the three-dimensional transition to turbulence in the incompressible flow around a NACA0012 wing. *Journal of Fluid Mechanics*, 496, 63–72.
- Huai, W., Xue, W., & Qian, Z. (2015). Large-eddy simulation of turbulent rectangular open-channel flow with an emergent rigid vegetation patch. *Advances in Water Resources*, 80, 30–42.
- Huang, R. F., Wu, J. Y., Jeng, J. H. and Chen, R. C. (2001). Surface flow and vortex shedding of an impulsively started wing. *Journal of Fluid Mechanics*, 441.
- Hunt, J., Wray, A. and Moin, P. (1988). Eddies, Stream, and Convergence Zones in Turbulent Flows. *Proceeding of the Summer Program in Center for Turbulence Research*, 193-208.
- Jahanmiri, M. (2011). Laminar Separation Bubble: Its Structure, Dynamics and Control. Research report 2011:06, Chalmers University of Technology.

- Jardin, T., and David, L. (2014). Spanwise gradients in flow speed help stabilize leading-edge vortices on revolving wings. *Physical Review E*, 90(1).
- Jaworski, J. W., and Peake, N. (2020). Aeroacoustics of silent owl flight. *Annual Review of Fluid Mechanics*, 52(1).
- Jeong, J. and Hussain, F. (1995). On the identification of a vortex. *Journal of fluid mechanics*, 285, 69-94.
- Johnson, W. (2013). *Rotorcraft Aeromechanics*. Cambridge University Press.
- Jones, L. E., Sandberg, R. D., and Sandham, N. D. (2008). Direct numerical simulations of forced and unforced separation bubbles on an airfoil at incidence. *Journal of Fluid Mechanics*, 602.
- Kitsios, V., Cordier, L., Bonnet, J.-P., Ooi, A., and Soria, J. (2011). On the coherent structures and stability properties of a leading-edge separated aerofoil with turbulent recirculation. *Journal of Fluid Mechanics*, 683, 395–416.
- Kitsios, V., Cordier, L., Bonnet, J.-P., Ooi, A., and Soria, J. (2011). On the coherent structures and stability properties of a leading-edge separated aerofoil with turbulent recirculation. *Journal of Fluid Mechanics*, 683, 395–416.
- Klän, S, Klaas, M, and Schröder, W. (2010). The influence of leading-edge serrations on the flow field of an artificial owl wing. *28th AIAA Applied Aerodynamics Conference*, Chicago, Illinois, USA.
- Klän, S., Bachmann, T., Klaas, M., Wagner, H. and Schröder, W. (2009). Experimental analysis of the flow field over a novel owl-based airfoil. *Experiments in Fluids*, 46, 975–989.

- Klose, B. F., Spedding, G. R., and Jacobs, G. B. (2021). Direct numerical simulation of cambered airfoil aerodynamics at $Re= 20,000$. arXiv eprint arXiv:2108.04910.
- Kraichnan, R. H. (1973). Helical turbulence and absolute equilibrium. *Journal of Fluid Mechanics*, 59(04), 745..
- Krishnan, K. (2022). Aerodynamics and turbulent wake-flow characteristics of owls during flapping flight. PhD Thesis, Coastal Carolina University.
- Kroeger, R.A, Gruschka, H.D. and Helvey, T.C. (1972). Low speed aerodynamics for ultra-quiet flight. Technical Report AFFDL TR-71-75.
- Kudela, H. and Malecha, Z. M. (2009). Eruption of a boundary layer induced by a 2D vortex patch. *Fluid Dynamics Research*, 41(5), 055502.
- Lam, K. M. (1996). Phase-locked eduction of vortex shedding in flow past an inclined flat plate. *Physics of Fluids*, 8(5), 1159–1168.
- Lawley, J., Ben-Gida, H., Krishnamoorthy, K., Hackett, E.E., Kopp, G.A., Morgan, G. and Gurka, R. (2019). Flow features of the near wake of the Australian boobook owl (Ninox boobook) during flapping flight suggest an aerodynamic mechanism of sound suppression for stealthy flight. *Integrative Organismal Biology*, 1(1), obz001.
- Lee, S. J. (2017). Numerical simulation of vortex-dominated flows using the penalized VIC method. *Vortex Dynamics and Optical Vortices*, *IntechOpen*, 52536.
- Levich, E. and Tsinober, A. (1983). On the role of helical structures in three-dimensional turbulent flow, *Physics Letter*, 93A, 293(1983).

- Levich, E. and Tsinober, A. (1984). On dynamical fractal models of homogeneous turbulence, *Physics Letter*, 101A, 265.
- Lewalle, J. and Ashpis, D. E. (2004). Estimation of time scales in unsteady flows in a turbomachinery rig. NASA/TM—2004-209452.
- Lilley, G.M. (1998). A study of the silent flight of the owl. *4th AIAA/CEAS Aeroacoustics Conference*, Toulouse, France.
- Linehan, T., and Mohseni, K. (2020). On the maintenance of an attached leading-edge vortex via model bird alula. *Journal of Fluid Mechanics*, 897.
- Liu, T., Kuykendoll, K., Rhew, R. and Jones, S. (2006). Avian wing geometry and kinematics. *AIAA Journal*, 44(5),954-963.
- Löchert, P., Huber, K. C., Ghoreyshi, M., and Allen, J. (2019). Control device effectiveness studies of a 53° swept flying wing configuration. Experimental, computational, and modeling considerations. *Aerospace Science and Technology*, 105319.
- Luton, A., Ragab, S. and Telionis, D. (1995). Interaction of spanwise vortices with a boundary layer. *Physics of Fluids*, 7(11), 2757–2765.
- Mascha, E. (1904). The structure of wing-feathers. *Zeitschrift für Wissenschaftliche Zoologie*, 77, 606–651.
- McAuliffe, B.R. and Yaras, M.I. (2009). Passive manipulation of separation-bubble transition using surface modifications. *Journal of Fluids Engineering*, 131, 021201:1-16.
- McCullough, G. B. and Gault, D. E. (1951). Examples of Three Representative Types of Airfoil-Section Stall at Low-Speed. NACA TN 2502.

- McDonough, J.M. (2007). *Introductory lectures on turbulence: physics, mathematics, and modeling*. Mechanical Engineering Textbook Gallery, University of Kentucky.
- Mcmasters, J. H., and Henderson, M. L. (1979) Low-speed single-element airfoil synthesis. *Technical Soaring* 4, 2 (1979), 1–21.
- Metcalfe, R.W., Orszag, S.A., Brachet, M.E. and Riley, J.J. (1987). Secondary instability of a temporally growing mixing layer. *Journal of Fluid Mechanics*, 184, 207–243.
- Moffatt, H. K. (1969). The degree of knottedness of tangled vortex lines. *Journal of Fluid Mechanics*, 35(01), 117.
- Moffatt, H. K., and Tsinober, A. (1992). Helicity in Laminar and Turbulent Flow. *Annual Review of Fluid Mechanics*, 24(1), 281–312.
- Moin, P. (2010). *Fundamentals of engineering numerical analysis*. Cambridge University Press.
- Nafi, A., Ben-Gida, H., Guglielmo, C. G., and Gurka, R. (2020). Aerodynamic forces acting on birds during flight: a comparative study of a shorebird, songbird and a strigiform. *Experimental Thermal and Fluid Science*, 110018.
- Nedić, J. and Vassilicos, J. C. (2015). Vortex Shedding and Aerodynamic Performance of Airfoil with Multiscale Trailing-Edge Modifications. *AIAA Journal*, 53(11), 3240–3250.
- Neuhaus, W., Bretting, H. and Schweizer, B. (1973). Morphologische und funktionelle untersuchungen über den “lautlosen” flug der Eulen (*Strix aluco*)

imVergleich zum Flug der Enten (*Anas platyrhynchos*). *Biologisches Zentralblatt*, 92, 495-512.

- Norberg, U. M. (2012). *Vertebrate flight: Mechanics, physiology, morphology, ecology and evolution*. Springer Berlin, Heidelberg.
- Ol, M., McCauliffe, B., Hanff, E., Scholz, U., and Kaehler, C. (2005). Comparison of Laminar Separation Bubble Measurements on a Low Reynolds Number Airfoil in Three Facilities. *35th AIAA Fluid Dynamics Conference and Exhibit*.
- O'Meara, M. M. and Mueller, T. J., (1987) "Laminar Separation Bubble Characteristics on an Airfoil at Low Reynolds Numbers", *AIAA Journal*, Vol. 25, No. 8, Aug. issue, pp 1033-1041.
- Orlandi, P. (1997). Helicity fluctuations and turbulent energy production in rotating and non-rotating pipes. *Physics of Fluids*, 9(7), 2045–2056.
- Orlandi, P. (2001). *Fluid flow phenomena: a numerical toolkit*. Kluwer Academic Publishers.
- Orlandi, I. (1976). Simple boundary-condition for unbounded hyperbolic flows. *Journal of Computational Physics*, 21, 251–269.
- Orlandi, I. (1976). Simple boundary-condition for unbounded hyperbolic flows. *Journal of Computational Physics*, 21, 251–269.
- Othman, A.K., Zekry, D.A., Saro-Cortes, Lee, K. J. and Wissa, A. A. (2023). Aerial and aquatic biological and bioinspired flow control strategies. *Communications Engineering*, 2, 30.

- Pal, A., Sarkar, S., Posa, A. and Balaras, E. (2017). Direct numerical simulation of stratified flow past a sphere at a subcritical Reynolds number of 3700 and moderate Froude number. *Journal of Fluid Mechanics*, 826, 5–31.
- Pauley, L. L., Moin, P., & Reynolds, W. C. (1990). The structure of two-dimensional separation. *Journal of Fluid Mechanics*, 220(-1), 397.
- Pauley, W. R. and Eaton, J. K. (1988). Experimental study of the development of longitudinal vortex pairs embedded in a turbulent boundary layer. *AIAA Journal*, 26(7), 816–823.
- Pelz, R. B., Yakhot, V., Orszag, S. A., Shtilman, L., and Levich, E. (1985). Velocity-Vorticity Patterns in Turbulent Flow. *Physical Review Letters*, 54(23), 2505–2508.
- Pérez-Torró, R., and Kim, J. W. (2017). A large-eddy simulation on a deep-stalled aerofoil with a wavy leading edge. *Journal of Fluid Mechanics*, 813, 23–52.
- Perry, A. E., and Steiner, T. R. (1987). Large-scale vortex structures in turbulent wakes behind bluff bodies. Part 1. Vortex formation processes. *Journal of Fluid Mechanics*, 174(-1), 233.
- Pope, S.B. (2000). *Turbulent flows*. Cambridge University Press.
- Posa, A. and Balaras, E. (2018). Large Eddy Simulation of an isolated vertical axis wind turbine. *Journal of Wind Engineering and Industrial Aerodynamics*, 172, 139–51.

- Posa, A., Parker, C. M., Leftwich, M.C. and Balaras E. (2016). Wake structure of a single vertical axis wind turbine. *International Journal of Heat and Fluid Flow*, 61, 75–84.
- Posa, A., Vanella, M., and Balaras, E. (2017). An adaptive reconstruction for Lagrangian, direct-forcing, immersed-boundary methods. *Journal of Computational Physics*, 351, 422–436.
- Posdziech, O., and Grundmann, R. (2007). A systematic approach to the numerical calculation of fundamental quantities of the two-dimensional flow over a circular cylinder. *Journal of Fluids and Structures*, 23(3), 479–499.
- Rahromostaqim, M., Posa, A. and Balaras E. (2016). Numerical investigation of the performance of pitching airfoils at high amplitudes. *AIAA Journal*, 54, 2221–32.
- Rao C., Ikeda T., Nakata T., and Liu H. (2017). Owl-inspired leading-edge serrations play a crucial role in aerodynamic force production and sound suppression. *Bioinspiration and Biomimetics*, 12(4), 046008.
- Rao, D. M. (1984). Leading edge flap system for aircraft control augmentation. U.S. Patent 4,485,992.
- Richardson, L.F. (1922). *Weather prediction by numerical process*. Cambridge: Cambridge University Press.
- Rinoie, K. and Takemura, N. (2004). Oscillating behaviour of laminar separation bubble formed on an aerofoil near stall. *The Aeronautical Journal*, 108(1081), 153–163

- Robinson, S. K. (1991). Coherent motions in the turbulent boundary layer. *Annual Review of Fluid Mechanics*, 23(1), 601–639
- Saffman, P. G. and Baker, G. R. (1979). Vortex Interactions. *Annual Review of Fluid Mechanics*, 11(1), 95–121.
- Sandham, N. D. (2008). Transitional separation bubbles and unsteady aspects of aerofoil stall. *The Aeronautical Journal*, 112(1133), 395–404.
- Saussaman, T., Nafi, A., Charland, D., Ben-Gida, H., and Gurka, R. (2023). The role of leading-edge serrations in controlling the flow over owls' wing. *Bioinspiration & biomimetics*, 18(6).
- Schmitz, F. W. (1942). *Aerodynamik des Flugmodells*. C. J. E. Volckmann Nachf. E. Wette, Berlin-Charlottenburg, 1942.
- Sedaghatizadeh, N. (2018). The effect of unsteady flow on wind turbine wake development and noise generation. PhD thesis, The University of Adelaide, Australia.
- Shyy, W., Lian, Y., Tang, J., Viieru, D. and Liu, H. (2008). *Aerodynamics of low Reynolds number flyers*. Cambridge University Press.
- Smith, C. E., Beratlis, N., Balaras, E., Squires, K., and Tsunoda, M. (2010). Numerical investigation of the flow over a golf ball in the subcritical and supercritical regimes. *International Journal of Heat and Fluid Flow*, 31(3), 262–273.
- So, J., Ryan, K. and Sheard, G. J. (2007). Interaction of an unequal-strength vortex pair, *In Proceedings of the 16th Australasian Fluid Mechanics Conference*, Crown Plaza, Gold Coast, Queensland, Australia.

- Soldati, A., and Banerjee, S. (1998). Turbulence modification by large-scale organized electrohydrodynamic flows. *Physics of Fluids*, 10(7), 1742–1756.
- Spedding, G. R., and McArthur, J. (2010). Span Efficiencies of Wings at Low Reynolds Numbers. *Journal of Aircraft*, 47(1), 120–128.
- Strawn, R. C., Kenwright, D. N. and Ahmad, J. (1999). Computer visualization of vortex wake systems. *AIAA Journal*, 37(4), 511–512.
- Swalwell, K., Sheridan, J., and Melbourne, W. (2003). Frequency analysis of surface pressures on an airfoil after stall. *21st AIAA Applied Aerodynamics Conference*.
- Swamy, N. V. C., Gowda, B. H. L., and Lakshminath, V. R. (1979). Auto-correlation measurements and integral time scales in three-dimensional turbulent boundary layers. *Applied Scientific Research*, 35(4), 237–249.
- Swarztrauber, P.N. (1974). Direct method for the discrete solution of separable elliptic equations. *SIAM Journal of Numerical Analysis*, 11, 1136.
- Swarztrauber, P.N. (1984). Fast Fourier transforms algorithms for vector computers. *Parallel Computing*. 45–63.
- Taira, K., and Colonius, T. (2009). Three-dimensional flows around low-aspect-ratio flat-plate wings at low Reynolds numbers. *Journal of Fluid Mechanics*, 623, 187.
- Tank, J., Smith, L., and Spedding, G. R. (2016). On the possibility (or lack thereof) of agreement between experiment and computation of flows over wings at moderate Reynolds number. *Interface Focus*, 7(1), 20160076.
- Tennekes, H. and Lumley, J.L. (1972). *A first course in turbulence*. MIT press.

- Thorpe, W.H. and Griffin D.R. (1962). The lack of ultrasonic components in the flight noise of owls compared with other birds. *Ibis*, 104, 256–57.
- Torenbeek, E., Wittenberg, H. and Calvert, S. (2009). *Flight physics: Essentials of aeronautical disciplines and technology, with historical notes*. Springer.
- Townsend, A., Jiya, I. N., Martinson, C., Bessarabov, D., and Gouws, R. (2020). A comprehensive review of energy sources for unmanned aerial vehicles, their shortfalls, and opportunities for improvements. *Heliyon*, 6(11), e05285.
- Tsinobar, A. (2001). An informal introduction to turbulence. Springer Netherlands.
- Udaykumar, H.S., Mittal, R. and Shyy, W. (1999). Computation of solid-liquid phase fronts in the sharp interface limit on fixed grids. *Journal of Computational Physics.*, 153, 535–574.
- Visbal, M. R. (2011). Numerical Investigation of Deep Dynamic Stall of a Plunging Airfoil. *AIAA Journal*, 49(10), 2152–2170.
- Wagner, H., Weger, M., Klaas, M. and Schröder, W. (2017). Features of owl wings that promote silent flight. *The Royal Society: Interface Focus*, 7(1), 20160078.
- Wallace, J. M. (2016). Quadrant analysis in turbulence research: history and evolution. *Annual Review of Fluid Mechanics*, 48(1), 131–158.
- Wallace, J. M., Brodkey, R. S. and Eckelmann, H. (1972). The wall region in turbulent shear flow. *Journal of Fluid Mechanics*, 54, 39–48.

- Wang, Y., Zhao, K., Lu, X.-Y., Song, Y.-B., and Bennett, G. J. (2019). Bio-Inspired Aerodynamic Noise Control: A Bibliographic Review. *Applied Sciences*, 9(11), 2224.
- Weger, M. and Wagner, H. (2016). Morphological Variations of Leading-Edge serrations in Owls (Strigiformes). *PLoS One*, 11(3): e0149236.
- Winzen, A., Roidl, B., Klän, S., Klaas, M., and Schröder, W. (2014). Particle-Image Velocimetry and Force Measurements of Leading-Edge Serrations on Owl-Based Wing Models. *Journal of Bionic Engineering*, 11(3), 423–438.
- Yang, J. (2005). An embedded-boundary formulation for large-eddy simulation of turbulent flows interacting with moving boundaries. PhD thesis, University of Maryland.
- Yang, J., and Balaras, E. (2006). An embedded-boundary formulation for Large-Eddy Simulation of turbulent flows interacting with moving boundaries. *Journal of Computational Physics*, Vol. 215, No. 1, 2006, pp. 12–40.
- Yang, Z. (2013). Numerical study of instabilities in separated–reattached flows. *International Journal of Computational Methods and Experimental Measurements* 1(2):116-131.
- Yang, Z. and Voke, P. R. (2001). Large-eddy simulation of boundary-layer separation and transition at a change of surface curvature. *Journal of Fluid Mechanics*, 439.
- Yarusevych, S., and H. Boutilier, M. S. (2011). Vortex shedding of an airfoil at low Reynolds numbers. *AIAA Journal*, 49(10), 2221–2227.

- Yarusevych, S., Kawall, J. G. and Sullivan, P. E. (2008). Separated-Shear-Layer Development on an Airfoil at Low Reynolds Numbers. *AIAA Journal*, 46(12), 3060–3069.
- Yarusevych, S., Sullivan, P. E., and Kawall, J. G. (2009). On vortex shedding from an airfoil in low-Reynolds-number flows. *Journal of Fluid Mechanics*, 632, 245.
- Zaman, K. B. M. Q., Mckinzie, D. J. and Rumsey, C. L. (1989). A natural low-frequency oscillation of the flow over an airfoil near stalling conditions. *Journal of Fluid Mechanics*, 202(-1), 403.
- Zauner, M., De Tullio, N. and Sandham, N. D. (2019). Direct numerical simulations of transonic flow around an airfoil at moderate Reynolds numbers. *AIAA Journal*, 1–11.
- Zhang, W., and Samtaney, R. (2016). Assessment of spanwise domain size effect on the transitional flow past an airfoil. *Computers and Fluids*, 124, 39–53.

